This is to certify that the

dissertation entitled

Elastic and Structural Properties

of Composite Materials

presented by

Jidong Chen

has been accepted towards fulfillment
of the requirements for

Ph.D. degree in **Physics**

M. F. Thorpe

Major professor

Date **April 13, 1994**

DATE DUE	DATE DUE	DATE DUE
MAY 07 2001 ~~12200~~		

ELASTIC AND STRUCTURAL PROPERTIES OF COMPOSITE MATERIALS

By

Jidong Chen

A DISSERTATION

Submitted to

Michigan State University

in partial fulfillment of the requirements

for the degree of

DOCTOR OF PHILOSOPHY

Department of Physics and Astronomy

1994

ABSTRACT

ELASTIC AND STRUCTURAL PROPERTIES OF COMPOSITE MATERIALS

By

Jidong Chen

In this thesis we have studied the structural and elastic properties of composite materials. Our research provided a good understanding for the whole range of composites. The inclusions could be of any shape with any elastic properties, from perfectly rigid body to completely empty holes. We also investigated the effect of adhesion on the inclusion-matrix interface and gave the theoretical formulae for all of the elastic moduli under different interfacial boundary conditions. In particular, we studied the local strain in random composites under hydrostatic pressure, and found what appeared to be the first example of local geometry dominating the local strain near close packing. We performed computer simulation to support our analytical results whenever necessary.

The field of composite material is of great importance because composites form a new generation of materials which may replace most of the metal and wood in the next century. In order to achieve this goal, we must have a deep understanding of the elastic properties of composites. The interface of the geometry is another important issue in the study of the structural properties of composites. By adjusting the arrangement of inclusions, we can enhance the performance of composites greatly.

Up to now composites have been studied mainly by Mechanical Engineers, Polymer Engineers and Materials Scientists who are more interested in the mechanical

properties and chemical properties. Physicists are seldom involved in this area. By modifying the concept of *percolation*, which is widely known to physicists from the studies of phase transitions, we introduced the concept of *rigidity percolation* for continuous medium. We have calculated the critical components for all of the elastic moduli, and given the asymptotic formulae to the elastic compliances and Poisson's ratio around rigidity threshold. Moreover, we found that a fixed point in the Poisson's ratio flow diagram did not exist in general, which was different from the results obtained in the study of lattice networks where a fixed point always occurred.

Another field studied in this thesis is the $2d$ porous materials. Porous materials can be used in packaging, for which their mechanical performance under external loading is crucial. We studied the elastic properties of two-dimensional composites containing polygonal holes, and compared this problem with the corresponding conductivity problem.

We are now studying the elastic properties of two-dimensional composites containing elliptical holes or cracks. This is a problem involving an anisotropic continuous medium. We want to explain crack formation and propagation in composites, which are very important in the practical applications of composites.

To my wife, Ann

ACKNOWLEDGEMENTS

I would like to thank my thesis advisor, Professor M. F. Thorpe, for his understanding, support and encouragement in the last five years. It is he who introduced me to the field of disordered systems and suggested this work in the gap between physics and engineering. His broad knowledge of both physics and materials science, his deep insight into complicated phenomena, his ability to *glue* different fields together and his approach to scientific research is a real inspiration to me.

I would like to express my thanks to Professor I. Jasiuk, M. Dubson, S. Simkin and J. Linnemann for their service on my Ph. D. guidance committee. I would also like to thank Professor J. S. Kovacs for his assistance during my study at MSU. The help I got from Mrs. Janet King and Mrs. Stephanie Holland in the last five years is greatly appreciated.

I would like to thank Dr. L. C. Davis in Ford Motor Company for teaching me ABAQUS and for his help in arranging for me to work at Ford in the summer of 1992, which gave me valuable exposure to the automotive industry.

Professor A. R. Day from Marquette University is acknowledged for providing a subroutine of the Conjugate Gradient Method.

Especially, I would like to thank Professor M. F. Thorpe, I. Jasiuk, P. M. Duxbury, S. D. Mahanti, M. Gandhi and Dr. L. C. Davis for giving me references during my last year at MSU.

My thanks also go to my friends Q. Zhu, B. Chen, N. Ju, Y. Cai, W. Zhong, Q. Yang, H. Wang, N. Mousseau, B. Djordjevic, S. Hyun and S. Kim. Their friendship made my days at MSU most enjoyable and special.

Finally, my thanks are due to my parents for their support and encouragement. Special thanks must go to my grandfather, for his love which comes long distance and half-way around the world. I also owe a large debt to my wife, Ann. I am very grateful for her love, understanding and patience throughout my arduous educational journey. It is her love that keeps me going and finishing this thesis.

Contents

1 INTRODUCTION 1

2 SIMULATION TECHNIQUES 10

2.1 DIGITAL-IMAGE-BASED METHOD 10

2.2 FINITE ELEMENT ANALYSIS 16

3 DILUTE RESULTS AND EFFECTIVE MEDIUM THEORY 21

3.1 INTRODUCTION 21

3.2 GEOMETRY AND BOUNDARY CONDITIONS 22

3.3 ELASTIC STRAIN ENERGY 25

3.4 TWO-DIMENSIONAL UNIDIRECTIONAL COMPOSITE 27

3.4.1 Single-inclusion Solution 27

3.4.2 Dilute Result 29

3.4.3 Self-Consistent Solution 31

3.4.4 Differential Scheme 33

3.5 THREE-DIMENSIONAL PARTICULATE COMPOSITE 37

3.5.1 Dilute Result 37

3.5.2 Self-Consistent Solution 39

3.5.3 Differential Scheme 40

3.6 DISCUSSION 42

3.7 CONCLUSIONS 47

4 RIGID FIBER-REINFORCED COMPOSITES **53**

4.1 INTRODUCTION 53

4.2 THEORY 54

4.2.1 Elasticity Theory for a Two-dimensional Isotropic System . . 54

4.2.2 Dilute Limit 54

4.2.3 Results Near the Rigidity Threshold 55

4.2.4 Compression Mode 56

4.2.5 Shear Mode 58

4.3 CRITICAL BEHAVIORS 58

4.3.1 Triangular Arrangement 59

4.3.2 Hexagonal Arrangement 62

4.3.3 Kagomé Arrangement 63

4.4 IMPROVEMENTS IN THE BULK MODULUS AT RIGIDITY THRESHOLD 67

4.5 EFFECTIVE MEDIUM THEORY 73

4.6 SIMULATON RESULTS 74

4.7 CONCLUSIONS 80

5 FINITE ELEMENT ANALYSIS **83**

5.1 INTRODUCTION 83

5.2 DILUTE RESULTS 84

5.3 SIMULATION RESULTS 85

5.4 CONCLUSIONS 88

6 LOCAL STRAIN IN RANDOM COMPOSITES **99**

6.1 INTRODUCTION 99

6.2 THEORY 100

6.3 SIMULATIONS 103

6.4 CONCLUSIONS 108

7 BOUNDS FOR FIBER ALIGNED COMPOSITES **111**

7.1 INTRODUCTION 111

7.2 BOUNDS FOR THE TRANSVERSE ELASTIC MODULI 112

7.3 EFFECTIVE MEDIUM THEORY 115

7.4 STRAIN AND STRESS TENSOR FOR A TRIANGULAR NETWORK 117

7.5 RESULTS FOR GLASS - EPOXY FIBER COMPOSITE 121

7.6 CONCLUSIONS 128

8 MATERIALS WITH POLYGONAL HOLES **131**

8.1 INTRODUCTION 131

8.2 TWO-DIMENSIONAL ELASTICITY 132

8.3 CLM TRANSFORMATION AND THEOREM 133

8.4 DUNDURS CONSTANTS 134

8.5 A MATERIAL CONTAINING HOLES 135

8.6 A MATERIAL WITH POLYGONAL HOLES 136

8.7 SIMULATION RESULTS 139

8.8 EFFECTIVE MEDIUM THEORIES 143

8.9 DISCUSSION 149

9 CONCLUSION **152**

A CONFORMAL MAPPING **157**

B THE SHEET CONTAINING ELLIPTICAL HOLES OR CRACKS 164

C HILL'S THEOREM FOR AN N-SLAB IN D-DIMENSIONS **174**

C.1 CASE 1: External Loading in x_1 Direction 176

C.2 CASE 2: External Loading in x_2 Direction 178

C.3 CONCLUSIONS 179

List of Tables

6.1 Occurrence of nearest neighbors for a configuration with 240 disks . . 102

7.1 The microstructural parameter ζ and η for IOC model 116
7.2 The Young's modulus and Poisson's ratio for glass and epoxy 123
7.3 α, β, γ for glass and epoxy. 123

8.1 Relation between $2d$ and $3d$ elastic moduli 133
8.2 Relation between α, ν_0 and n 140

A.1 Analytical and numerical values for parameters α and ν_0 for triangular holes 160
A.2 Analytical and numerical values for parameters α and ν_0 for square holes 161
A.3 Analytical and numerical values for parameters α and ν_0 for pentagonal holes 162
A.4 Analytical and numerical values for parameters α and ν_0 for hexagonal holes 162

List of Figures

1.1 A typical cross section of fiber-reinforced composite 5

2.1 Triangular grid with interlocking honeycomb lattices 12
2.2 Three possible configurations 15

3.1 Nonoverlapping circular fiber composite 23
3.2 2D Self-consistent method, Poisson's ratio flow diagram 34
3.3 2D Differential scheme, Poisson's ratio flow diagram 35
3.4 2D Shear modulus for different $\tilde{k}$ 38
3.5 3D Self-consistent method, Poisson ratio flow diagram 41
3.6 Comparison of bulk modulus 44
3.7 Overlapping circular fiber composite 48

4.1 The compression mode and shear mode 57
4.2 Triangular Superlattice 60
4.3 Hexagonal Superlattice 64
4.4 Kagomé Superlattice 66
4.5 Cartoon for calculating modified bulk modulus 69
4.6 Poisson's ratio flow diagram 78
4.7 Bulk modulus for different structures 79

5.1 The type of basic elements for $2d$ and $3d$ used in simulation 89
5.2 Mesh for triangular superlattice, version 1 90

5.3 Mesh for triangular superlattice, version 2 91
5.4 Mesh for hexagonal superlattice 92
5.5 Mesh for Kagomé superlattice 93
5.6 Poisson's ratio flow diagram, pure sliding boundary condition 94
5.7 Effective bulk modulus, pure sliding boundary condition 95
5.8 Stress map, yy component, pure sliding, hexagonal superlattice 96
5.9 σ_{rr} and $\sigma_{r\phi}$ on the fiber-matrix interface 97

6.1 Neck region between two rigid disks 101
6.2 Local strain ϵ_i vs gap width w_i 105
6.3 Voronoi construction for a random array of disks 106
6.4 Bulk modulus k_0/k vs area fraction of matrix 107

7.1 The local grid configuration 119
7.2 Effective area bulk and shear modulus 122
7.3 Strain and stress map for $f_2 = 0.01$ 125
7.4 Strain and stress map for $f_2 = 0.20$ 126
7.5 Strain and stress map for $f_2 = 0.55$ 127

8.1 Randomly cut triangular holes 138
8.2 Results of α and ν_0 142
8.3 Young's modulus obtained from differential scheme 144
8.4 Poisson' ratio obtained from self-consistent scheme 146

9.1 A typical mesh generated by my ABAQUS preprocessor for random fiber-reinforced composites 154

A.1 Shapes corresponding to the conformal mapping 158

B.1 A sheet containing elliptical holes 167
B.2 A sheet containing cracks 168
B.3 The elastic compliances for the sheet shown in Fig. B.1 169

B.4 The effective Young's modulus and Poisson's ratio for a matrix containing randomly distributed, oriented, overlapping elliptical holes . . 170
B.5 A sheet containing a single crack 171
B.6 The effective Young's modulus for a matrix containing randomly distributed, oriented, overlapping cracks 172

C.1 N-slab in d-dimensions 175

Chapter 1

INTRODUCTION

The technology of composite materials has a very long history. Two-thousand years ago, people learned to make mud bricks with chopped straw in order to give a better tensile strength than brittle dried mud. In 800 B.C., straw was certainly used by the Israelites in the manufacture of sun-baked bricks which had a compressive strength about one quarter of the strength of modern fired bricks [1]. Composites have also been used in the construction of weapons since early times. The Mongol bow was made of composite of animal tendons, wood and silk bonded together with an adhesive, and the Japanese ceremonial swords were of laminated structure [1].

But the science of composite material made little progress until the 19th century when Clausius studied the problem of electrical conductivity of composites consisting of matrix and embedded spherical particles [2]. Thirty years ago, the goal of providing lighter-weight, higher stiffness and strength aircraft provided an incentive for the development of advanced fiber composites. Since the early 1960s a very considerable world-wide investment has been made to develop artificial composites, especially fiber-reinforced composites [3]. Because most of the conventional engineering materials, such as steel, aluminum, titanium, beryllium, boron, glass, carbon, and others, are very brittle, they are not suitable candidates for aircraft. To minimize their brittleness, these materials have been obtained in fibrous form for incorporation

into metallic and polymer matrices. Therefore, rigorously speaking, a composite material is not a material in the classical sense but an infinite family of materials which the designer can choose or create according to his needs. Nowadays, "stronger than steel, stiffer than titanium, and lighter than aluminum" are no longer the exaggerated advertisement words shown on newspaper and TV.

By definition, a composite is a material consisting of two or more discrete physical phases, in which a fibrous phase is dispersed within a continuous matrix phase. The fibrous phase may be macro-, micro- or sub-microscopic, but it must retain its physical identity, such that it conceivably could be removed from the matrix intact [4]. For example, particles of steel mixed with a plaster form a composite, since there are distinct regions of plaster and distinct regions of steel. Typical composites in nature are wood and bone. Usually composites have properties in strength, rigidity or thermal expansion, which are superior to the corresponding properties of individual phases. The properties of a composite depend not only on the properties of its constituents, but also depend on their distribution and their physical and chemical interactions between each other.

The name of *fiber-reinforced composite* comes from the fact that fibers are harder and stronger than the matrix in a composite, although this is not true in some cases. In the last three decades, there has been a tremendous advance in the science and technology of this new class of materials. The primary reason is that usually a composite has low density, high strength, high stiffness to weight ratio, excellent durability, and design flexibility. As a result, it can be used as a substitute for metals in industrial applications.

Because of the advantages of fiber-reinforced materials, they have been widely used in aircraft, missile, space shuttle, automobile, marine and sporting goods. For example, graphite epoxy is used for more than 50% of the surface area of the McDonnell-Douglas F-18 Hornet (aircraft), and accounts for 10% of the overall structural weight [5]. Using carbon fiber composites can save up to 40% in structural weight, which

allows aircraft to carry more fuel and a greater payload for the same takeoff weight. Although expensive, the advantages of better fuel economy and greater payload liftoff make carbon fibers very competitive with other materials. Using composites not only can reduce the weight significantly, but can also reduce the number of subcomponents. A typical example is that a ten-leaf steel rear spring in the Corvette automobile was replaced by a uni-leaf E-glass reinforced epoxy in 1981, which saved about 80% in weight [6] and gave a higher internal damping than steel springs. Daily use is another impetus to the development of this field. Increased research and development have made fiber-reinforced materials enter our daily life. Many sporting goods, such as golf club shafts, tennis rackets, fishing rods, ski poles, and so on, are made of graphite composites. If you go to a sporting store to buy a tennis racket, you will notice that the cheap ones (for beginners) are made of aluminum, and the expensive ones (for professionals) are made of graphite fibers.

Yet many manufactures have been slow to embrace composites. The chief problem is that composites can be much more expensive and difficult to work with than metal. Also, minor variations in mixing and processing can result in fatally flawed composites that will not perform as designed. But with the development of science and technology, these disadvantages will be overcome soon. In the next century, from automobile bodies and bridge support beams to our kitchen clock, things now made with metal will be fashioned from lighter, stronger composite materials. Composites may change our society even more than plastics did in the last forty years.

The *fiber* plays a dominant role in fiber-reinforced materials. A fiber is exactly what the name implies. It is a long continuous strand of a material, much like the fiber used in the textile industry. Fiber carries the major portion of the load and imparts stiffness to the structure. For nonbrittle materials such as most metals and polymers, we can just simply group fibers together into a bundle in order to obtain a high tensile modulus. But unfortunately the strongest materials are all very brittle. Therefore, we can not use them in ropes because the coiling and surface abrasion between fibers can

easily introduce extensive cracking. However, fibers can be embedded in deformable matrices to form a fiber-reinforced composite. By choosing fiber and matrix properly, this composite can have the desired properties. For example, glass is very brittle and it is well known that a small surface scratch on it can lead to the breaking of a piece of glass. But if glass fibers are embedded in a plastic matrix, then the small cracks, which occasionally occur in individual fibers, will not easily grow through the mixture. Therefore, this composite is no longer brittle, but it retains some of the good properties of glass, such as large strength and stiffness. This is the beauty of composite materials — they can provide high fracture toughness at high strength levels, which is impossible for each single material.

Figure 1.1 shows a cross section of composites with silica fibers randomly dispersed in a continuous matrix of aluminum [7]. It indicates that the fibers are of fairly constant diameters, while there is a considerable variation in spatial arrangement, *i.e.*, an occasional fiber pair is almost touching, while others are well apart. This is the reason why we assume that fibers are of the same diameters throughout the thesis.

The *matrix* is another important component in fiber-reinforced composites. The major functions of the matrix are that (1) it protects the surface of the fibers against adverse environment by providing a barrier (2) it binds the fibers together to form a bundle and (3) it transfers loads between fibers, which can deflect cracks that may occur in fibers in the longitudinal direction. The matrix holds the composite together and permits the material to be formed into different shapes as required for manufacturing. For example, a network of fibers forming a shell would collapse under its own weight. But the presence of a matrix can keep the fibers in the desired locations and directions. The matrix also makes it possible to tailor the material to achieve the desired strength and stiffness in a particular direction.

The degree of contact and the cohesive forces at the interface are of considerable importance, because stress is transmitted from one phase to another across an

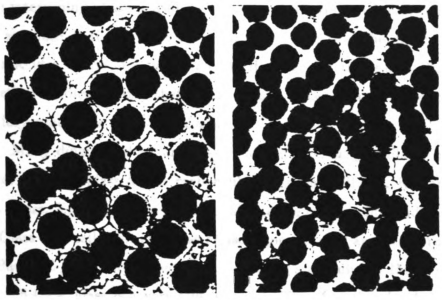

Figure 1.1: Section of 47% silica fibers dispersed in a continuous matrix of aluminum ($\times 150$)

interface [1]. Two phases (phase A and phase B) may be in direct contact with each other, or may be separated by an intervening phase between them. The intervening phase may be deliberately added to improve the adhesion, or it may be the result of a chemical reaction between the two phases. The elastic properties of the intervening phase are very difficult to specify. Usually we just assume that the elastic constants of the intervening phase is a linear function of its width, with the elastic properties same as phase A at one surface and same as phase B at the other surface. This is the basic idea of the *three-phase model.* However, for the reason of simplicity most theoretical studies assume that phase A and phase B actually touch with certain boundary conditions on the interface.

Many different fibers and matrix are commercially available now. The most popular ones are glass fibers, carbon fibers (graphite fibers), Kevlar 49 fibers and boron fibers. Epoxy, polyester and metals are the most useful candidates for the matrix. Glass is usually considered as an isotropic material and has a Young's modulus 76 GPa for E-glass. Compared with the Young's modulus of IMHS epoxy, which is about 3.5 GPa, glass is a very stiff material. Therefore, for simplicity in theory we can regard the glass fibers as a perfect-rigid inclusion. Since this assumption can simplify the mathematical calculations a lot, but also gives the correct characteristic behavior of the composite, we use this assumption in **Chapters 3 – 6**. In order to check if the perfect-rigid-inclusion assumption is reasonable, we use a real material (E-glass, IMHS epoxy) in **Chapter 7** and compare it with the analytic expressions of bounds for elastic moduli, given by Torquato, Hashin, etc., to verify the correctness of our work.

This thesis is a combination of the research in which I have been involved during my Ph.D. program at Michigan State University. Prof. M. F. Thorpe, Prof. I. Jasiuk from Michigan State University, and Dr. L. C. Davis, Dr. K. C. Hass from Ford Motor Company, have contributed greatly to this work. Details are as follows.

In **Chapter 1** I give an introduction to composite materials. Composite

materials are very important in both science and engineering. This field combines Physics, Mechanics, Materials Science, Mechanical Engineering, Chemical Engineering and Polymer Science. It is the diversity of composites that interests me in this field, and let me choose composite materials as the topic of my thesis. This field also reminds me from time to time that my knowledge in Physics is not purely academic but is closely related to industry.

In **Chapter 2** I illustrate two computer simulation techniques which are widely used in the thesis. One of them is the Digital-Image-Based Method which is basically one of the versions of the Finite Difference Method. This method is the most common one used in the Computational Physics, such as in the Molecule Dynamics. But the finite difference method has its limitations when dealing with mechanical problems involving complex geometry or complicated boundaries. Therefore, I also apply another computer simulation technique called the Finite Element Method in the thesis. The finite element method is the most popular method used in Mechanics and Mechanical Engineering. It also has some applications in Physics, such as solving the Schrödinger equation in Quantum Mechanics. The detailed discussion of these two simulation techniques can be found in **Chapter 2**.

In **Chapter 3** I study the adhesion on the matrix-inclusion interface in composite materials. In the dilute concentration limit, I study this problem by solving $4th$ order non-linear elastic equations; and in other concentration regions, I approach this problem by using effective medium theory. I would like to point out that I derived most of the formulae for $2d$ case, and Prof. I. Jasiuk and Prof. M. F. Thorpe did most of the work in $3d$.

In **Chapter 4** I study the elastic and structural properties of fiber-reinforced composites. The interface condition is assumed to be perfectly bonded which is the most common approximation to practical cases. This work comes from the ideas of Prof. M. F. Thorpe. All of the computer simulation is done by the author.

In **Chapter 5** I move one more step further toward investigating the interfa-

cial effect in composites by using the Finite Element Method. The interface condition is assumed to be purely sliding, which is the opposite extreme limit with respect to the perfectly bonding case. This part of the work was finished entirely by the author at Ford Motor Company in the summer of 1992. The help from Dr. L. C. Davis and the invitation from Ford Motor Company are greatly appreciated.

In **Chapter 6** I study the relation between the local geometry and local strain. This work appears to be important in practice because it provides an easy and non-destructive testing method for composite materials. The idea for this work came from Dr. L. C. Davis at Ford in the summer of 1992 when I worked there. Dr. L. C. Davis and Dr. K. C. Hass derived most of the formulae, and the author is responsible for all of the simulations.

In **Chapter 7** I use computer simulation to study the different elastic bounds in fiber-reinforced composites. This work was finished by the author under the guidance of Prof. M. F. Thorpe.

In **Chapter 8** and **Appendix A** I study porous materials with polygonal holes, elliptical holes, or cracks in a uniform matrix. The effective medium theory and conformal mapping method are used. Most of the theoretical work in this chapter was done by Prof. M. F. Thorpe and Prof. I. Jasiuk, and I contributed all of the simulation work.

Finally in **Chapter 9** I give a brief summary of my Ph.D. research during the last couple of years at Michigan State University. I also briefly discuss some of our current work and illustrate some perspectives on our future work.

Bibliography

[1] L. Holliday, Composite Materials, Elsevier Publishing Company, New York (1966).

[2] Z. Hashin, Opening Remarks on the IUTAM Symposium on Mechanics of Composite Materials, Blacksburg, Virginia (1982).

[3] J. B. Donnet and R. C. Bansal, Carbon Fiber, Marcel Dekkeer, Inc., New York and Basel (1990).

[4] H. W. Rauch, W. H. Sutton and L.R. McCreight, Ceramic Fibers and Fibrous Composite Materials, Academic Press, New York and London (1968).

[5] J. R. Vinson, Composite Materials, edited by K. Kawata & T. Akasaka, Proc. Japan-U.S. Conference, Tokyo (1981).

[6] P. K. Mallick, Fiber-Reinforced Composites - Material, Manufacturing and Design, Marcel Dekkeer, Inc., New York and Basel (1988).

[7] D. E. Lloyd, Ceramic Systems, edited by L. Holliday, Elsevier Publishing Company, New York (1966).

Chapter 2

SIMULATION TECHNIQUES

In this thesis I use two kinds of computer simulation techniques. One of them is *Digital-Image-Based Method*, and the other one is *Finite Element Analysis*.

2.1 DIGITAL-IMAGE-BASED METHOD

The digital-image-based method is one of the most fundamental methods for the study of continuous systems by using computer simulations. Computers can only deal with discrete variables. Therefore, when we study a continuum system, we digitalize the system first, that is, use a set of discrete variables to represent the corresponding continuous physical quantities. Recently this method has been used successfully in solving many practical problems, such as the diffusivity of cement-based materials [1], the roughness of blasted steel panels [2], and the elastic moduli of a sheet containing circular holes [3].

In this thesis, I use a special type of digital-image-based method, which we call the *spring-grid model*, to calculate the transverse effective elastic moduli of fiber-reinforced composites. The idea of this method is very similar to the finite difference method, in which the partial differential equations of elasticity are solved by approximating derivatives by quotients of differences. We represent the continuum material

by a underlying discrete lattice which has the same elastic properties as the original continuum material. The lattice we choose is a triangular network in which the six nearest neighbor points are connected by springs obeying Hooke's law. The reason we use a triangular net instead of a square net is that the square net is not stable unless we introduce angular forces between springs or introduce further neighbor interactions.

The triangular network is formed from three interlocking honeycomb lattices, each lattice having different spring constants α, β and γ, as shown in Fig. 2.1. From our previous work [3], we know that such an arrangement makes the system isotropic with the area bulk modulus k and transverse shear modulus G given by

$$k = \frac{1}{\sqrt{12}}(\alpha + \beta + \gamma),$$

$$G = \sqrt{\frac{27}{16}}\left(\frac{1}{\alpha} + \frac{1}{\beta} + \frac{1}{\gamma}\right)^{-1}. \tag{2.1}$$

In an isotropic two-dimensional system, there exist only two *independent* elastic constants. Therefore, once k and G are determined, we can get the Young's modulus E and Poisson's ratio ν through the relations

$$E = \frac{4kG}{k+G},$$

$$\nu = \frac{k-G}{k+G}. \tag{2.2}$$

Substituting (2.1) into (2.2), we find the Young's modulus and the Poisson's ratio for this triangular net

$$E = \frac{2\sqrt{3}(\alpha+\beta+\gamma)}{3\left[1 + \frac{2}{9}(\alpha+\beta+\gamma)(\frac{1}{\alpha}+\frac{1}{\beta}+\frac{1}{\gamma})\right]},$$

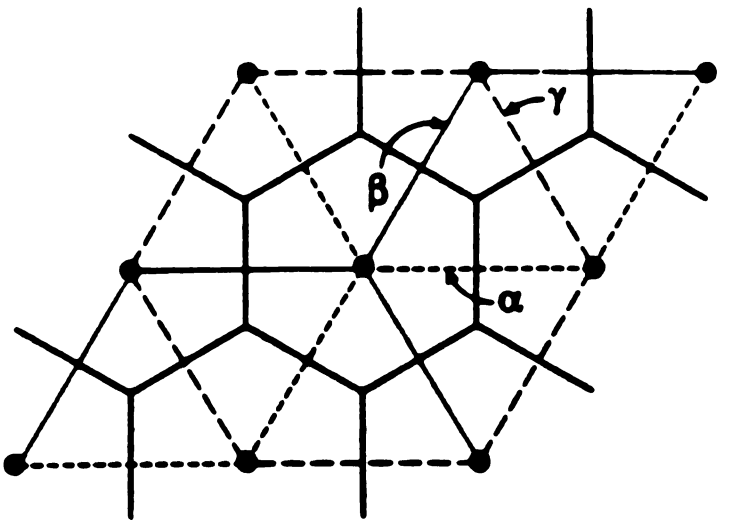

Figure 2.1: A piece of the triangular grid with three interlocking honeycomb lattices with spring constants α, β and γ, respectively. α: dots; β: dash; γ: solid.

$$\nu = 1 - \frac{2}{1 + \frac{2}{9}(\alpha + \beta + \gamma)(\frac{1}{\alpha} + \frac{1}{\beta} + \frac{1}{\gamma})}. \tag{2.3}$$

Eq. (2.3) allows ν to vary from 1/3 to 1 by adjusting the three spring constants α, β and γ. Note that α, β and γ are always kept positive for stability, and the Poisson's ratio is alway greater than or equal to 1/3. If one wants to study the problem in which $\nu < 1/3$, the angular forces have be to included in the triangular network. This part of work is not included in the thesis.

In the simulation, we use a 210×210 triangular lattice as a unit supercell and impose periodic boundary conditions. We use two sets of spring constants α, β and γ, one set chosen to give the elastic constants of the continuum matrix and the other chosen to give the elastic constants of the continuum fibers. The fibers are randomly placed on this triangular net, either overlapping or nonoverlapping and the spring constants are assigned values according to whether the springs lie in the matrix or fiber region.

For the overlapping case, a configuration is generated by randomly placing fibers on the matrix. For the nonoverlapping case, we use the Metropolis version of the Monte Carlo method to generate configurations [4]. We first set a 19×19 array of fibers with diameter 11 on this 210×210 matrix, which forms a perfect crystal. Then, we randomly remove some fibers to give the required concentration. After that, we randomly choose the fibers remaining on the matrix, one at time, and change the x and y coordinates by a random length between 0 and δr_{max}. Here δr_{max} is an adjustable parameter that governs the size of the square box in which the selected fiber can move. After such a change, we check whether the fiber selected, in its new position, overlaps with other fibers or not. If it overlaps, the selected fiber is not moved, otherwise the fiber is moved to the new position. We repeat this procedure about 10^5 times until we generate a random nonoverlapping configuration. The δr_{max} is adjusted every 50 steps to make the probability of movement of a selected fiber about 30%. The randomness of the final configuration is checked by calculating the

correlation function of the fiber centers.

In practice, fibers are often tightly bonded to the matrix. Therefore we use perfect bonding boundary conditions at the fiber-matrix interface. For nonoverlapping fibers embedded in a matrix (Identical Nonoverlapping Cylinders - - INC), there exist three possible configurations on the boundaries, as shown is Fig. 2.2(a), 2.2(b) and 2.2(c).

In Fig. 2.2(a), pixel A is in a fiber and pixel B is in the matrix, that is the spring AB crosses the surface of a fiber at a point defined as C. Under perfect bonding conditions, the spring AB can be viewed as two separate springs AC and CB joined together at point C. Therefore, assuming the natural length of the spring AB is unity, we find the spring constant K_{AB} through

$$\frac{1}{K_{AB}} = \frac{x}{K_{AC}} + \frac{1-x}{K_{CB}}. \tag{2.4}$$

where x and $1-x$ are the natural lengths of spring AC and CB, and K_{AC} and K_{CB} are the corresponding spring constants determined by the elastic properties of fiber and matrix, respectively.

In Fig. 2.2(b), pixel A and pixel B are in different fibers and the spring AB crosses the surfaces of two fibers at points C and D. By a similar argument, we find the effective spring constant of K_{AB} through

$$\frac{1}{K_{AB}} = \frac{x_1}{K_{AC}} + \frac{1-x_1-x_2}{K_{CD}} + \frac{x_2}{K_{DB}}. \tag{2.5}$$

where x_1 and x_2 are the natural lengths of the spring AC and DB, and $1-x_1-x_2$ is the natural length of the spring CD. K_{AC} and K_{DB} are corresponding spring constants determined by the elastic properties of the fiber and K_{CD} is determined by the matrix.

In our simulation we neglect the third case [Fig. 2.2(c)]. This is due to the fact that in our model the sample size is 210×210 and the diameter of fiber is 11. Because the distance between each pixel and its nearest neighbor is equal to 1, this

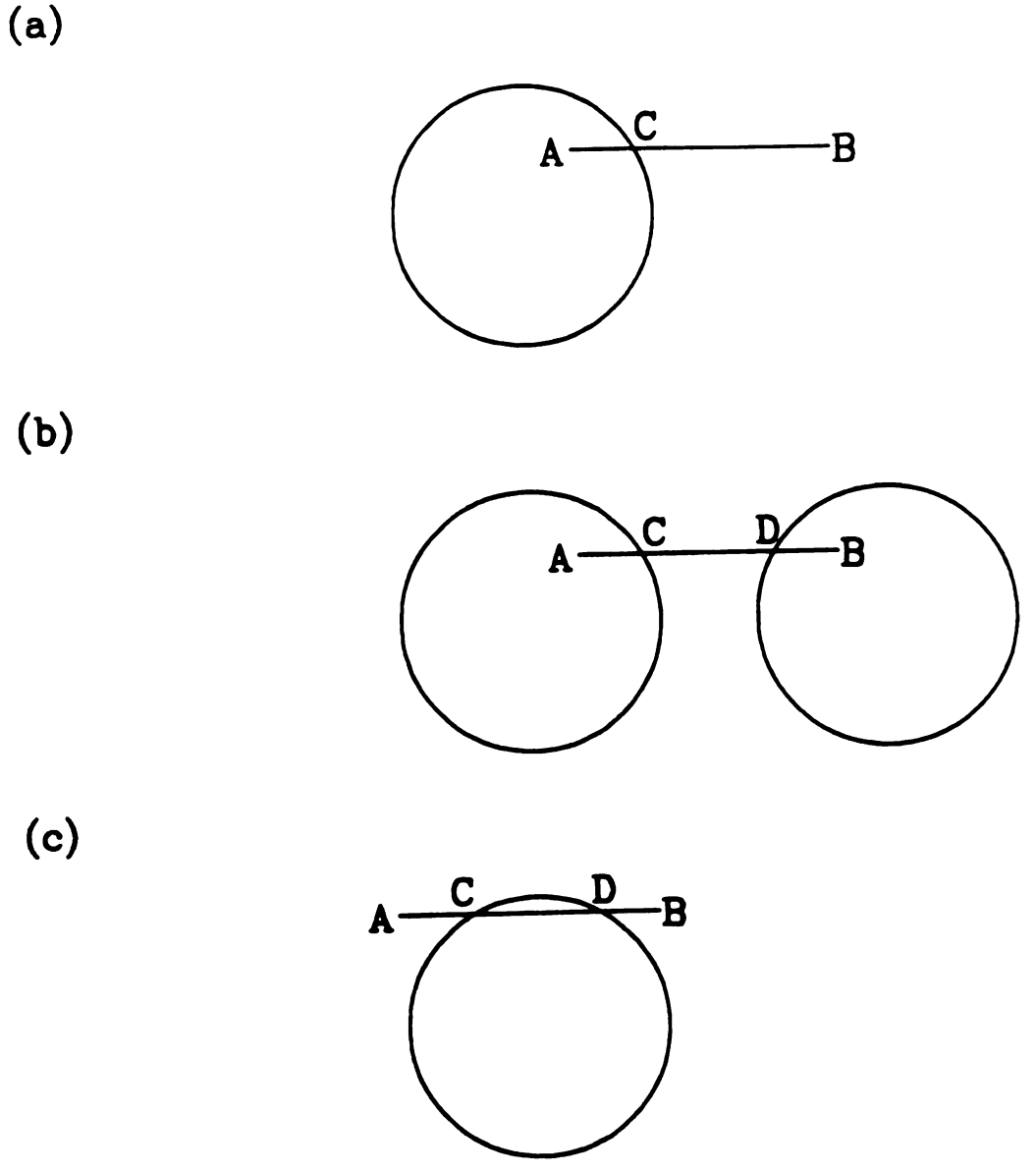

Figure 2.2: Showing the three possible configurations for spring AB at the fiber-matrix interface. The ratio of the natural length of AB to the diameter of fibers is exaggerated to show the details. (a) A is in fiber and B is in matrix. (b) Both A and B are in fibers. (c) Both A and B are in the matrix.

third case is very unlikely to happen. We checked all of the configurations we used and never found such a case. Therefore, we neglect this case in our simulations. In the Identical Overlapping Cylinders (IOC) model, we regard the overlapping area of fibers as having the same elastic properties as pure fiber.

After fixing the configuration of the springs we apply a uniaxial plane strain, typically of the order of 10^{-3}, to the composite. The nodes of the network and the length of the unit supercell perpendicular to the applied strain are simultaneously relaxed using the conjugate gradient method [3] [5]. When the system is fully relaxed the effective Young's modulus is determined from the total elastic energy per unit area. The area Poisson's ratio can also be obtained by measuring the length change in the direction perpendicular to the applied strain. After determining these two independent elastic moduli, all other elastic constants, such as the area bulk modulus and the transverse shear modulus, can be obtained through

$$k = \frac{E}{2(1-\nu)}, \tag{2.6}$$

$$G = \frac{E}{2(1+\nu)}. \tag{2.7}$$

2.2 FINITE ELEMENT ANALYSIS

The digital-image-based method is powerful for solving the porous problems and the composite problems in which the boundary conditions on fiber-matrix interface is perfectly bonded. If the boundary is purely sliding on the fiber-matrix interface, this method is very difficult to implement. So I switched to *finite element analysis*, a very popular simulation technique in engineering.

Although the label of *finite element method* first appeared on a paper written by Clough [6] on plane elasticity in 1960, the idea of finite element method was introduced a long time ago. A good example is the accurate calculations of π at a

very early date. In A.D. 480 the Chinese engineer Tsu Chung Chih determined π to lie between 3.1415926 and 3.1415927 [7]. This work was based on replacing the area of a circle with slender inscribed and circumscribed rectangles.

The finite element method is a numerical analysis technique for obtaining approximate solutions to a wide variety of engineering problem. This method has a wide range of applications. It can be used to solve *equilibrium problems*, such as to find the stress distribution or the displacement distribution or perhaps the temperature distribution for a given mechanical or thermal loading. It can also be used to solve *eigenvalue problems* of solid and fluid mechanics. One example is to find the natural frequencies and modes of vibration of dams and lakes when their interaction is considered. Another application of the finite element method is solving *propagation problems* in which the loadings are time-dependent. An example of this application is the crash simulation of a motor vehicle.

In more and more engineering situations today, people find that it is necessary to obtain approximate numerical solutions to problems rather than exact closed-form solutions, because in many cases the exact solution does not exist or is impossible to figure out. For example, when we design an air-inflated building, an axisymmetric thin shell, a ship's hull or the leg of an oil-drilling platform, we can write down the governing equations and boundary conditions for these problems without too much effort, but we can see immediately that no simple analytic solution can be found. Mathematician may think that such problems have been '*solved*' because they can prove that an non-singular solution exists for each of these problems. But engineers are never satisfied with such '*solutions*'. They are called upon to obtain numerical answers.

Although originally developed to study the stresses in complex airframe structures, the finite element method has been extended and applied to the board field of continuum mechanics. The finite-element model typically requires hundreds or thousands of simultaneous equations, necessitating the use of a large computer and spe-

cialized data-handling programs. Furthermore, computer-assisted modelling (CAM) and display aids usually are needed to build the model and interpret the results with reasonable time and cost. Fortunately, computer science has been developing very greatly in recent years, and large, powerful digital computers are now available at a relatively low price. Many commercial finite element packages, such ABAQUS and PATRAN, are on the market now and provide an improvement in dealing with more complicated situations. This provides the user an easy way to design complex structures, such as is done in engineering schools and in industry. Nowadays, CAD/CAM experts agree that one of the most powerful methods for analyzing a structure on a computer is the finite element method [8]. In the automotive industry, such as at Ford Motor Company, the FEM has been become a major tool in designing their new model cars and trucks.

Unlike the *finite difference method*, which envisions the solution region as an array of grid points, the finite element method envisions the solution region as built up of many small, interconnected subregions or elements. In finite element analysis, the first step is finite-element discretization which generates a *mesh* of simple *elements* (such as rods, shells or cubes) depending on the geometry of the structure. Each element is determined by a set of *nodes*, which is usually on the boundaries. Then, a continuum material is represented by these finite elements. After this step, the solution for each tiny chunk is determined either exactly by classical continuum mechanics, or approximately by an interpolation function using the basic idea that any continuous function can be represented by a linear combination of algebraic polynomials. Thus, the finite-element method can be interpreted as a piecewise application of variational methods, such as the Ritz and weighted-residual methods, in which the approximation functions are algebraic polynomials and the undetermined parameters represent the values of the solution at a finite number of nodes on the boundary and in the interior of the element [9]. Finally, all of the element properties must be *assembled* in order to find the properties of the overall system modeled by the network

of elements. At this step both the boundary conditions between elements and the boundary conditions on the overall system are considered simultaneously.

Bibliography

[1] E. J. Garboczi and D. P. Bentz, Journal of Materials Science, **27**, 2083 (1992).

[2] J. W. Martin and D. P. Bentz, presentation at the 64th Annual Meeting of the Federation of Societies for Coatings Technology, Atlanta, GA (1986).

[3] A. R. Day, K. A. Snyder, E. J. Garboczi and M. F. Thorpe, J. Mech. Phys. Solids, **40**, No. 5, 1031 (1992).

[4] M. P. Allen and D. J. Tildesley, Computer Simulation of Liquids, p.118, Oxford University Press, Oxford, England (1987).

[5] W. H. Press, B. P. Flannery, S. A. Teukolsky and W. T. Vetterling, Numerical Recipes, p.301, Cambridge University Press, Cambridge, England (1986).

[6] R. W. Clough, Proceedings of 2nd. ASCE Conference on Electronic Computation, Pittsburgh, PA (1960).

[7] H. C. Martin and G. F. Carey, Introduction to Finite Element Analysis, McGraw-Hill Book Company, New York (1973).

[8] J. K. Krouse, What Every Engineer Should Know About Computer-Aided Design and Computer-Aided Manufacturing, Marcel Dekker, Inc., New York and Basel (1983).

[9] K. H. Huebner and E. A. Thornton, The Finite Element Method for Engineers, John Wiley & Sons, Inc., New York (1982).

Chapter 3

DILUTE RESULTS AND EFFECTIVE MEDIUM THEORY

3.1 INTRODUCTION

Composite materials are very important in engineering applications, because their properties can be tailored to design specifications. There are many factors that influence the elastic properties of composites: the elastic constants and volume fractions of the constituents; the shape, size and geometric arrangement of the reinforcement; the boundary conditions at the inclusion-matrix interface on the elastic properties of composite materials; and others. In this chapter, we concentrate on the effect of the interfaces on the elastic properties of composite materials. To facilitate the discussion, we use the example of rigid inclusions in two and three dimensional geometries.

There exist various models to determine the macroscopic properties of composites. An extensive list of references on works in this area is given by MURA, HASHIN, and CHRISTENSEN, among others [1] [2] [3]. Most of the existing theories, however, assume perfect bonding at the matrix-inclusion interface. Several theoretical studies, which do include the effect of imperfect bonding in the composites, are due to BROUTMAN and AGARWAL, LENE and LEGUILLON, BENVENISTE, ABOUDI,

STEIF and HOYSAN, THEOCHARIS, MAURER *et al.*, SIDERIDIS, PAGANO and TANDON, BENVENISTE *et al.*, ACHENBACH and ZHU, JASIUK and TONG, JASIUK *et al.*, and HASHIN, among others [4] - [18]. However, the work in this area is far from complete.

In this chapter, we first obtain solutions for a single isolated inclusion. We employ an interface parameter k that describes sliding at the interface. Two important limiting cases are perfect bonding ($k \to \infty$) and perfect sliding ($k \to 0$). We explicitly forbid debonding (separation) and for simplicity consider only the case of rigid inclusions. The single-inclusion results are used to obtain exact expressions for the effective elastic moduli of composites with a dilute concentration of inclusions. Finally, the results for the dilute case are used in effective medium theories to predict the overall elastic properties of composites with a high volume fraction of rigid sliding inclusions. The methods employed include the self-consistent approach [19] [20] and the differential scheme [21] [22]. We show that the Poisson's ratio has very interesting behavior at high volume fractions of reinforcement, in that it tends to certain universal values that are independent of Poisson's ratio of the matrix, but do depend on the interface parameter k. We also show that both effective medium theories give remarkably similar results in the pure sliding limit.

3.2 GEOMETRY AND BOUNDARY CONDITIONS

In the analysis, two composite systems are used: a unidirectional composite and a particulate composite. In both cases the fibers or particles are randomly distributed in the elastic matrix. In the unidirectional composite material, as shown for example in Fig. 3.1, the fibers are cylindrical, have a circular cross-section and are aligned. The composite is assumed to be clamped in the longitudinal direction so the deformation can occur only in the transverse direction. In the particulate composite, the particles are assumed to be spherical in shape. In this chapter we would like to predict the

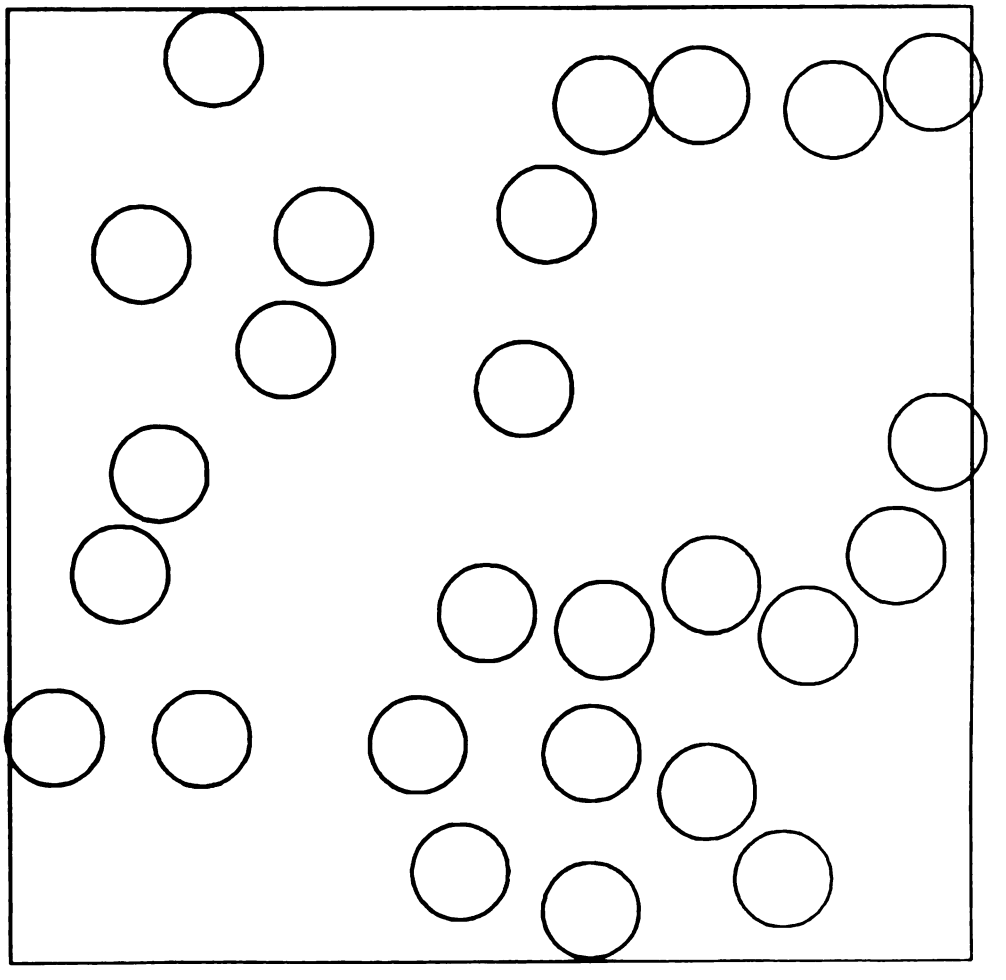

Figure 3.1: Sketch of a cross-section through a unidirectional composite containing random arrangement of aligned fibers with a circular cross-section and volume fraction $f = 0.2$. The centers of the fibers were generated using pairs of random numbers, with overlaps not allowed.

effective elastic properties of these two types of composites.

Initially, the micromechanics approach is used by solving the elasticity problem of a single inclusion embedded in the infinite matrix and subjected to mechanical loading. The boundary conditions at the interface involve continuity of traction and of the normal displacement, but shear traction is taken to proportional to the jump in the tangential displacement. This representation of imperfectly bonded interface has been used by LENE and LEGUILLON [5] and BENVENISTE [6], among others. For an inclusion having a circular cross-section, these boundary conditions can be written as:

$$\sigma_{rr}^{i} = \sigma_{rr}^{m}$$

$$u_{r}^{i} = u_{r}^{m}$$

$$\sigma_{r\theta}^{i} = \sigma_{r\theta}^{m} = k[u_{\theta}] \tag{3.1}$$

For the spherical inclusion to be discussed later, two additional equations are needed:

$$\sigma_{r\phi}^{i} = \sigma_{r\phi}^{m} = k[u_{\phi}] \tag{3.2}$$

The superscripts m and i refer to the matrix and inclusion, respectively. The displacements are u_{α} and the stresses are $\sigma_{\alpha\beta}$. Tangential slip is allowed by the scalar interface parameter k, and $[u_{\theta}] = (u_{\theta}^{m} - u_{\theta}^{i})$ and $[u_{\phi}] = (u_{\phi}^{m} - u_{\phi}^{i})$ are the discontinuities in the tangential displacements. If the inclusion is considered to be rigid (i.e. its elastic moduli are very much stiffer than those of the matrix), then the boundary conditions (3.1) and (3.2) reduce to:

$$u_{r} = 0$$

$$\sigma_{r\theta} = k u_{\theta} \tag{3.3}$$

$$\sigma_{r\phi} = k u_{\phi} \tag{3.4}$$

and the inclusion is nondeformable. We have dropped the superscript m from the quantities in (3.3) and (3.4) to simplify the notation. There is no confusion with notation in the rigid inclusion limit as all quantities refer to the matrix. In the expression (3.3) and (3.4), k is the factor of proportionality which denotes the degree of bonding at the surface. In the limit, when $k \to \infty$, the perfect bonding condition is obtained, and when $k \to 0$, the pure sliding limit is reached. Observe that, in this model, the interface is represented as a very thin fictitious layer having a spring-like behavior for tangential displacements. Radial separation is not allowed. These, somewhat artificial, but mathematically well defined springs *do not permit delamination to occur*, but do control the degree of sliding. We imagine the continuum limit in which there is a large surface density of these small interface springs.

3.3 ELASTIC STRAIN ENERGY

When an isolated elastic inhomogeneity (inclusion) Ω in a domain D is subjected to an applied stress σ^0_{ij} at infinity, the elastic strain energy is expressed as

$$W = \frac{1}{2}\int_D (\sigma^0_{ij} + \tilde{\sigma}_{ij})(\varepsilon^0_{ij} + \tilde{\varepsilon}_{ij}) dV \tag{3.5}$$

where the strain fields are $\varepsilon_{ij} = \frac{1}{2}(u_{i,j} + u_{j,i})$. The superscript 0 denotes a quantity in the absence of the inclusion, and the superscript $\tilde{}$ designates the change in a quantity (disturbance) caused by the presence of the inclusion. Hence $\sigma_{ij} = \sigma^0_{ij} + \tilde{\sigma}_{ij}$ and $u_i = u^0_i + \tilde{u}_i$ are the total stresses and total displacements in the presence of the inhomogeneity. The stresses σ_{ij} satisfy the equations of equilibrium $\sigma_{ij,j} = 0$ and n_i is the outward unit vector normal to surface of inclusion $|\Omega|$. Then Eqn.(3.5) is expressed in terms of integrals on $|\Omega|$ as

$$W = W^0 + \frac{1}{2}\int_{|\Omega|} \sigma^0_{ij} n_j u_i dS - \frac{1}{2}\int_{|\Omega|} \sigma_{ij} n_j u^0_i dS + \frac{1}{2}\int_{|\Omega|} \sigma^0_{ij} n_j [u_i] dS - \frac{1}{2}\int_{|\Omega|} \sigma_{ij} n_j [u_i] dS \tag{3.6}$$

where $W^0 = \frac{1}{2}\int_D \sigma^0_{ij}\varepsilon^0_{ij} dV$. The elastic strain energy of the interface springs in given by

$$W^s = \frac{1}{2}\int_{|\Omega|} \sigma_{ij} n_j [u_i] dS = \frac{1}{2}\int_{|\Omega|} k[u_\theta]^2 dS \tag{3.7}$$

The total elastic strain energy W^c of the composite with boundary conditions given by (3.1) and (3.2) is the sum of the energy of elastic medium (matrix and inclusions) given by (3.6) and the energy of the interface springs given by (3.7):

$$W^c = W^0 + \frac{1}{2}\int_{|\Omega|} \sigma^0_{ij} n_j u_i dS - \frac{1}{2}\int_{|\Omega|} \sigma_{ij} n_j u^0_i dS + \frac{1}{2}\int_{|\Omega|} \sigma^0_{ij} n_j [u_i] dS \tag{3.8}$$

By simplifying this equation for the case of rigid inclusions, and expression similar to the Eshelby's formula for the energy [3] is obtained

$$W^c = W^0 + \frac{1}{2}\int_{|\Omega|} (\sigma^0_{ij} n_j u_j - \sigma_{ij} n_j u^0_i) dS \tag{3.9}$$

The elastic strain energy per unit volume stored in the equivalent homogeneous medium is

$$\frac{W^{equiv}}{D} = \frac{1}{2}\sigma^0_{ij} S^c_{ijkl} \sigma^0_{kl} \tag{3.10}$$

where S^c_{ijkl} is the (unknown) compliance of the composite.

The effective elastic constants can be obtained through the equality of the elastic strain energy stored in the heterogeneous medium (3.9) to that stored in the equivalent homogeneous medium (3.10)

$$\sigma^0_{ij} S^c_{ijkl} \sigma^0_{kl} = \sigma^0_{ij} S_{ijkl} \sigma^0_{kl} + \frac{f}{\Omega} \int_{|\Omega|} (\sigma^0_{ij} n_j u_i - \sigma_{ij} n_j u^0_i) dS \tag{3.11}$$

where f is the area or volume fraction of inclusions. Since the stress and displacement fields of the isolated inclusion are to be substituted in (3.11), the above expression will be valid only in the *dilute limit* (small f).

3.4 TWO-DIMENSIONAL UNIDIRECTIONAL COMPOSITE

3.4.1 Single-inclusion Solution

First, a solution for the problem of a single circular inclusion embedded in the infinite matrix is found by using standard techniques involving the Airy stress function [23]. We employ a polar coordinate system, related to the Cartesian system by $x = r\cos\theta$ and $y = r\sin\theta$, and let the origin of the coordinate system be at the center of the inclusion. When the applied loading is uniaxial tension at infinity $\sigma^0_{xx} = p$, the stresses in the matrix are given as

$$\sigma_{rr} = \frac{p}{2}\left[1 - \frac{Aa^2}{r^2} + \left(1 - \frac{2Ba^2}{r^2} - \frac{3Ca^4}{r^4}\right)\cos 2\theta\right]$$

$$\sigma_{\theta\theta} = \frac{p}{2}\left[1 + \frac{Aa^2}{r^2} - \left(1 - \frac{3Ca^4}{r^4}\right)\cos 2\theta\right]$$

$$\sigma_{r\theta} = -\frac{p}{2}\left(1 + \frac{Ba^2}{r^2} + \frac{3Ca^4}{r^4}\right)\sin 2\theta \tag{3.12}$$

and the displacements are

$$u_r = \frac{p}{8\mu}\left\{(\eta - 1)r + \frac{2Aa^2}{r} + \left[2r + B(\eta + 1)\frac{a^2}{r} + \frac{2Ca^4}{r^3}\right]\cos 2\theta\right\}$$

$$u_\theta = -\frac{p}{8\mu}\left[2r + B(\eta - 1)\frac{a^2}{r} - \frac{2Ca^4}{r^3}\right]\sin 2\theta \tag{3.13}$$

where a is the radius of the inclusion and μ is the shear modulus of the matrix. The constants A, B and C are evaluated subject to the boundary conditions (3.3) and are given by:

$$A = -\frac{(\eta - 1)}{2}$$

$$B = -\frac{4(1 + \tilde{k})}{3\eta + 1 + 2\tilde{k}\eta}$$

$$C = \frac{2\tilde{k} + 1 - \eta}{3\eta + 1 + 2\tilde{k}\eta} \tag{3.14}$$

where

$$\tilde{k} = \frac{ka}{2\mu} \tag{3.15}$$

and

$$\eta = \frac{(3 - \nu')}{(1 + \nu')} \text{ or } (3 - 4\nu') \tag{3.16}$$

where ν' is the Poisson's ratio of the matrix. The first option in (3.16) corresponds to the *plane stress* case and the second option corresponds to the *plane strain* condition. In our analysis η is taken as $(3 - 4\nu')$, since we assume plane strain. The results could readily be adapted to the plane stress case. We will refer to the important dimensionless quantity $\tilde{k}$ as the *interface-sliding parameter.*

When the applied loading is either all-around tension $\sigma^0_{xx} = \sigma^0_{yy} = p$ at infinity, or shear loading $\sigma^0_{xx} = -\sigma^0_{yy} = p$, the stresses and the displacements in the matrix can be obtained by superposition of the solution given in (3.12) and (3.13). Then the stress and displacement fields obtained above are used directly in the elastic energy calculations [Eqn. (3.11)] to predict the elastic moduli of the composite with a dilute concentration of fibers.

3.4.2 Dilute Result

Using (3.11), the expressions for the effective transverse properties of the unidirectional composite with a dilute volume fraction f of fibers are

$$\frac{K^c}{K} = 1 + f\frac{2}{(1+\nu)} \tag{3.17}$$

$$\frac{\mu^c}{\mu} = 1 + f\frac{4(1+\tilde{k})}{(5+3\tilde{k}) - (1+\tilde{k})\nu} \tag{3.18}$$

where μ^c, K^c are the transverse shear modulus and the area bulk modulus for the composite; K, μ are the transverse shear modulus and the area bulk modulus of the matrix, and ν is the plane strain transverse Poisson's ratio (area Poisson's ratio) of the matrix. Since we assume that the ends of the composite are clamped, the longitudinal Poisson's ratio of the composite is zero, and the whole deformation takes place in the transverse plane. Therefore, it is convenient to use the transformation equation relating Poisson's ratio ν' (three-dimensional) with the plane strain transverse Poisson's ratio ν (two-dimensional) as given by THORPE and SEN [24]

$$\nu = \frac{\nu'}{(1-\nu')} \tag{3.19}$$

It should be noted that ν is bounded from above by 1, while ν' is bounded by 1/2. This can be explained as follows: since the material does not deform in the longitudinal direction (due to clamped ends or because it is infinitely rigid in the longitudinal direction), then, if a uniaxial loading is applied in one transverse direction and the material is incompressible, it must contract by the same amount in the other transverse direction [3].

We note that the area bulk modulus (3.17) for the dilute case is independent of the interface-sliding parameter $\tilde{k}$, as would be expected. This is because no sliding is allowed by symmetry when an area pressure is applied in the plane containing a single inclusion. The initial slope of K^c depends only on the (dilute) volume fraction

of fibers f and on the area Poisson's ratio ν of the matrix material. The initial slope of the μ^c depends on these two parameters and also upon the interface -sliding parameter $\tilde{k}$. From (3.18), we see that

$$\frac{\partial \mu^c}{\partial \tilde{k}} > 0, \text{ for all } \tilde{k}, \nu \tag{3.20}$$

so that, as the sliding tendency increases, the interface-sliding parameter $\tilde{k}$ decreases, and the shear modulus μ^c decreases. This is in accord with what would be expected intuitively. Similar behavior holds for the three-dimensional composite discussed later in this chapter. From the two elastic moduli, given in (3.17) and (3.18), the other quantities of interest in the plane, the transverse Young's modulus E^c and the plane strain transverse Poisson's ratio ν^c, can be obtained via

$$E^c = \frac{4K^c\mu^c}{K^c + \mu^c}$$

$$\nu^c = \frac{K^c - \mu^c}{K^c + \mu^c} \tag{3.21}$$

Similar relations to (3.21) exist for the matrix in the absence of inclusions if the superscripts are dropped from Eqns. (3.21). The area Poisson's ratio in the dilute limit is obtained from (3.17), (3.18) and (3.21):

$$\nu^c = \nu + f(1-\nu)\frac{(3+\tilde{k}) - 3(1+\tilde{k})\nu}{(5+3\tilde{k}) - (1+\tilde{k})\nu} \tag{3.22}$$

Note that the initial slope of Poisson's ratio depends on ν, $\tilde{k}$ and f. By differentiating (3.22), it is easy to show that

$$\frac{\partial \nu^c}{\partial \tilde{k}} < 0, \text{ for all } \tilde{k}, \nu \tag{3.23}$$

so that as the sliding tendency increases, $\tilde{k}$ decreases, and therefore ν^c increases. This is also true for the three-dimensional composite.

For a *special* initial value ν^* of the plane strain transverse Poisson's ratio, Eqn. (3.22) shows that there is no change in the area Poisson's ratio of the composite to first order in f. This important value of ν^* is given by:

$$\nu^* = \frac{3 + \tilde{k}}{3(1 + \tilde{k})} \tag{3.24}$$

For perfect bonding $\nu^* = 1/3$ and for perfect sliding $\nu^* = 1$. Other values of $\tilde{k}$ lead to $1/3 < \nu^* < 1$. The quantity ν^* does depend on the nature of the interface through $\tilde{k}$, but is independent of the Poisson's ratio of the matrix material.

After calculating the effective elastic constants for a dilute concentration of inclusions we would like to predict the effective elastic properties for the nondilute case. Many approximate methods, accounting for the effect of interactions between the inclusions, exist in literature (see [1] [2] [3]). In this chapter, the self-consistent method [19] [20] and the differential scheme [21] [22] are modified to include the effect of sliding. In both of these methods, it is assumed that the inclusions are embedded in an infinite matrix having the same properties as the composite. In the differential scheme, a gradation of sizes is implied. In the discussion at the end of this chapter, we will refer to other popular models, such as the composite spheres and cylinders [25], three-phase model [26], which is often referred to as the generalized self-consistent method [14] and Mori-Tanaka method [27].

3.4.3 Self-Consistent Solution

It is convenient to invert Eqns. (3.17) and (3.18) to give

$$\frac{K}{K^c} = 1 - f\frac{2}{1 + \nu} \tag{3.25}$$

$$\frac{\mu}{\mu^c} = 1 - f\frac{4(1 + \tilde{k})}{(5 + 3\tilde{k}) - (1 + \tilde{k})\nu} \tag{3.26}$$

These are equally acceptable as solutions, given that (3.17) and (3.18) are only good to first order in f. The forms (3.25) and (3.26) are better to work with since the quantities on the left hand sides decrease, rather than increase, as more fibers are added to the composite. Self-consistency is achieved by replacing ν by ν^c on the right hand side of (3.25) and (3.26) to give:

$$\frac{K}{K^c} = 1 - f\frac{2}{1+\nu^c} \tag{3.27}$$

$$\frac{\mu}{\mu^c} = 1 - f\frac{4(1+\tilde{k})}{(5+3\tilde{k}) - (1+\tilde{k})\nu^c} \tag{3.28}$$

A more formal justification for this procedure can be given [19] [20], but operationally the above procedure is most straightforward. These equations are solved by forming a single equation for ν^c using (3.21), (3.27) and (3.28)

$$\frac{1+\nu}{1-\nu} = \frac{1+\nu^c}{1-\nu^c}\left\{\frac{1-2f/(1+\nu^c)}{1-4f(1+\tilde{k})/[(5+3\tilde{k})-(1+\tilde{k})\nu^c]}\right\} \tag{3.29}$$

which can be solved numerically to give the results for ν^c as a function of f as shown in Fig. 3.2 for the extreme cases of perfect bonding and pure sliding. The fixed point is most easily obtained from Eqns. (3.27) and (3.28) by setting K^c and μ^c to infinity. This leads to an area Poisson's ratio at the fixed point given by (3.24) and an associated volume fraction f^* given by:

$$f^* = \frac{2\tilde{k}+3}{3(\tilde{k}+1)} \tag{3.30}$$

This critical volume fraction f^* depends on $\tilde{k}$, but like ν^* is independent of the Poisson's ratio of the matrix. The fixed point is characterized by the pair (f^*, ν^*). Similar behavior is well known in other random elastic systems [28]. The point f^* is where the (overlapping) fibers form a continuous path through the composite, which becomes rigid under hydrostatic and shear loading. Although we have not explicitly put in the overlapping or non-overlapping of fibers in the theory, the result of the

self-consistent approach only makes sense if we assume that the fibers can overlap leading to an $f^* < 1$. Note that for the self-consistent method $f^* = (1 + \nu^*)/2$ for *all* values of $\tilde{k}$. The area bulk modulus K^c can be found by substituting ν^c obtained from (3.29) back into (3.27), and the transverse shear modulus can be obtained by using (3.28) and (3.29). The results for the bulk and shear moduli indicate that as the sliding increases the moduli decrease.

3.4.4 Differential Scheme

In this method, it is assumed that the composite has a wide distribution of fiber diameters. At each level of the iteration, a few larger fibers are put in the medium, which is made up of smaller fibers. This is done successively and in the limit a differential equation can be written using (3.22) as input:

$$d\nu^c = \frac{df}{(1-f)}(1-\nu^c)\frac{(3+\tilde{k}) - 3(1+\tilde{k})\nu^c}{(5+3\tilde{k}) - (1+\tilde{k})\nu^c} \tag{3.31}$$

This equation is integrated with the boundary condition, $f = 0$, when $\nu^c = \nu$, to give:

$$\left[\frac{(1-\nu)}{(1-\nu^c)}(1-f)^3\right]^{\tilde{k}/(6+4\tilde{k})} = \frac{(3+\tilde{k}) - 3(1+\tilde{k})\nu^c}{(3+\tilde{k}) - 3(1+\tilde{k})\nu}\frac{(1-\nu)}{(1-\nu^c)} \tag{3.32}$$

This is an implicit equation for $\nu^c(\nu, f)$, that is more easily interpreted as $f(\nu, \nu^c)$, and is shown in Fig. 3.3. Note that the fixed point is now always at $f^* = 1$ and the value of the area Poisson's ratio at this fixed point is again given by (3.24). The behavior of a composite at an intermediate value of f is heavily influenced by the flow diagram and fixed point in Fig. 3.3. In Eqn. (3.32), care must be used in taking the pure sliding limit ($\tilde{k} = 0$), by expanding both sides for small $\tilde{k}$. The result is:

$$(1-f)^3 = \frac{(1-\nu^c)}{(1-\nu)} exp\left[4\left(\frac{1}{1-\nu} - \frac{1}{1-\nu^c}\right)\right] \tag{3.33}$$

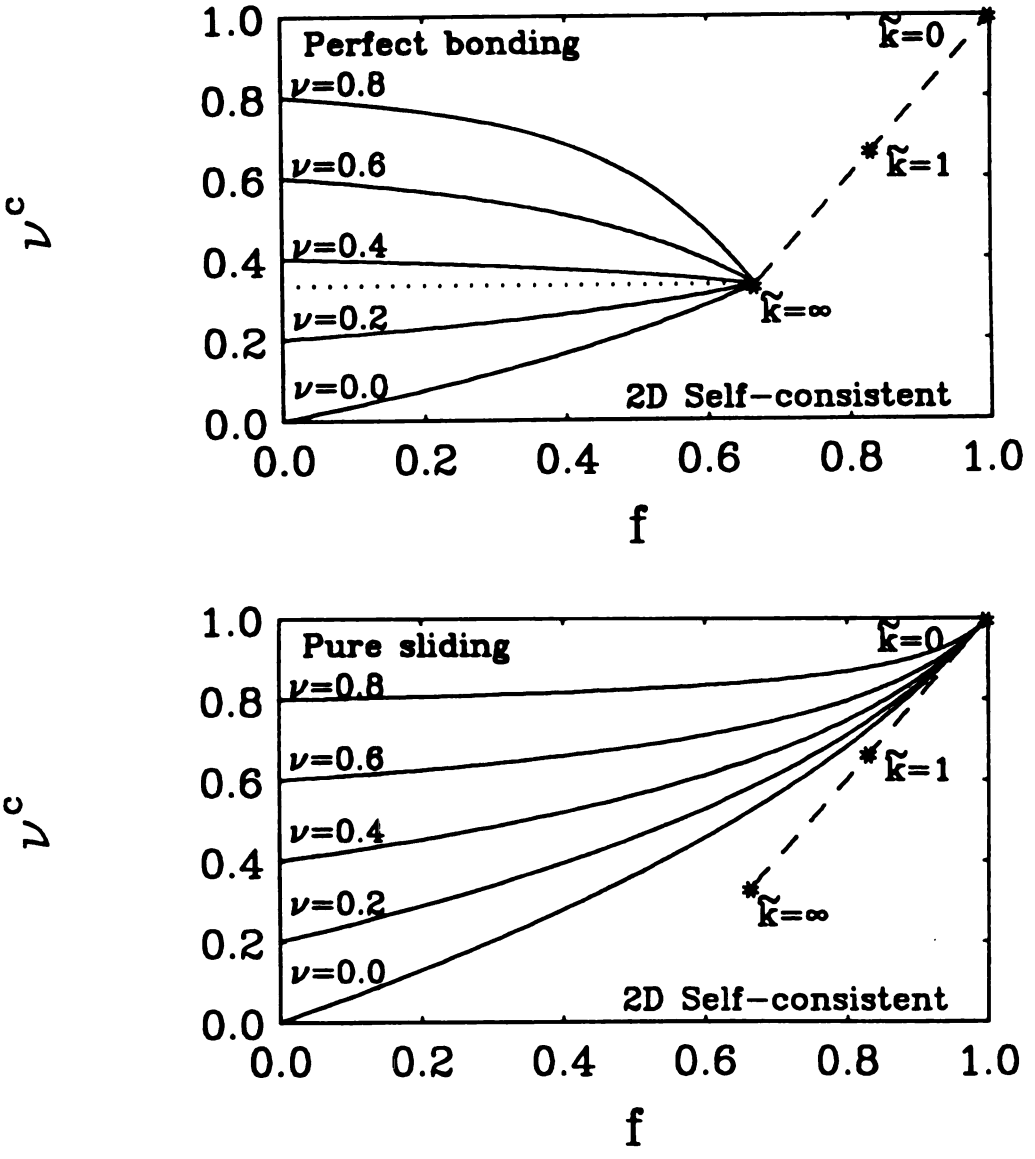

Figure 3.2: Flow diagram, using the self-consistent method, for the area Poisson's ratio of the composite ν^c is shown for a unidirectional (two-dimensional) composite with perfect bonding ($\tilde{k} = \infty$) or pure sliding ($\tilde{k}$=0) at the interfaces. For perfect bonding, the value of ν^c at the fixed point, $\nu^* = 1/3$, is indicated by the dotted line. The trajectory of the fixed point for various values of the interface-sliding parameter $\tilde{k}$ is indicated by a dashed line.

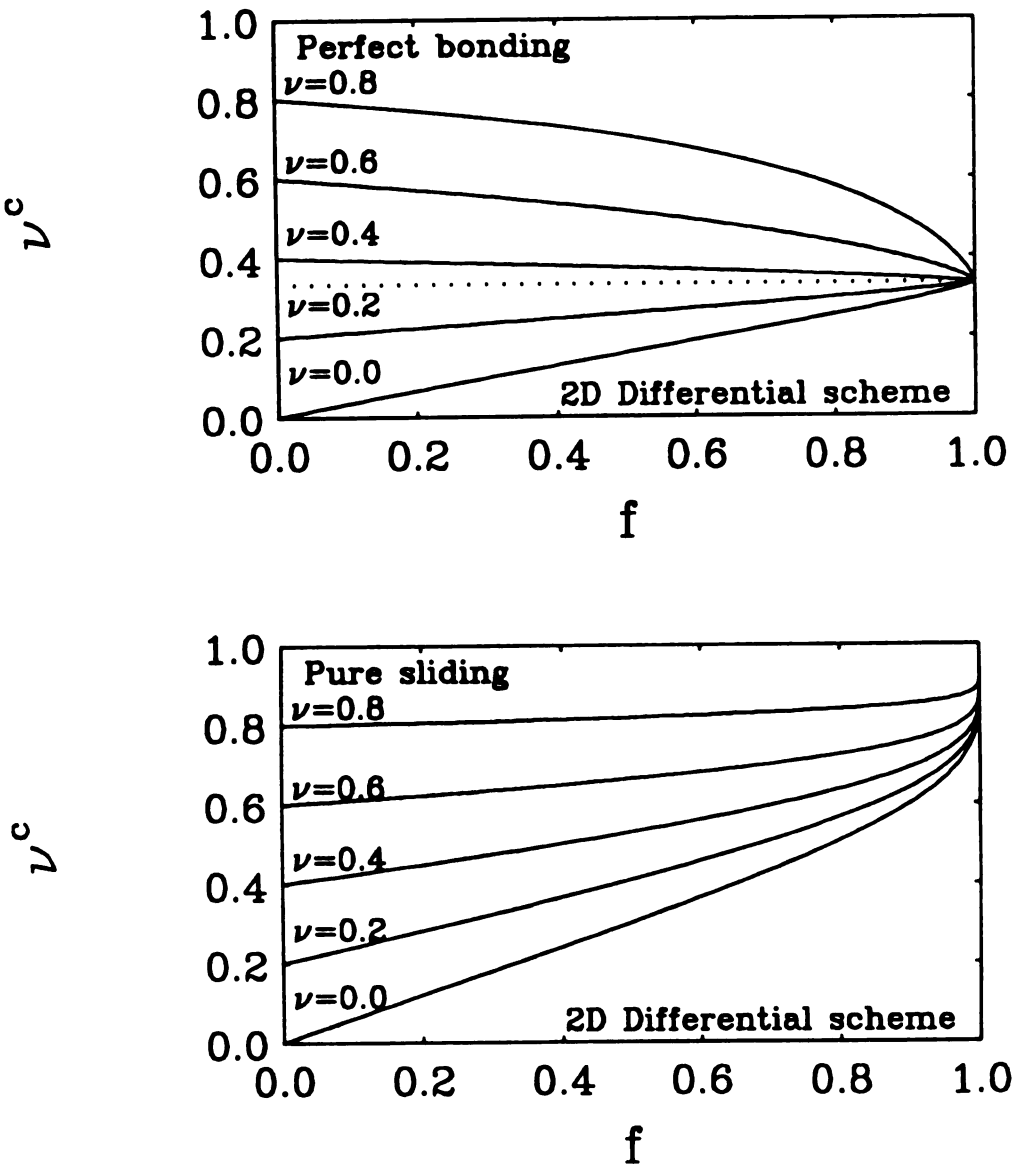

Figure 3.3: Flow diagram, using the differential scheme, for the area Poisson's ratio of the composite ν^c is shown for a unidirectional (two-dimensional) composite with perfect bonding ($\tilde{k} = \infty$) or pure sliding ($\tilde{k} = 0$) at the interfaces. For perfect bonding, the value of ν^c at the fixed point, $\nu^* = 1/3$, is indicated by the dotted line.

The transverse shear modulus μ^c can be found by iterating on the dilute solution (3.18) to give:

$$\frac{d\mu^c}{\mu^c} = 4\frac{df}{(1-f)}\frac{(1+\tilde{k})}{(5+3\tilde{k})-(1+\tilde{k})\nu^c} \tag{3.34}$$

This equation can also be integrated in closed form, if we use (3.31) to eliminate $df/(1-f)$ and do the integrals over μ^c and ν^c. The solution is most compactly written as:

$$\frac{\mu}{\mu^c} = \left[\frac{(1-\nu)}{(1-\nu^c)}(1-f)^3\right]^{(1+\tilde{k})/(3+2\tilde{k})} \tag{3.35}$$

From a knowledge of μ^c and ν^c, the other elastic constants K^c and E^c can be found from (3.21). The area bulk modulus is given by:

$$\frac{K}{K^c} = \frac{(1+\nu)(1-\nu^c)}{(1+\nu^c)(1-\nu)}\left[\frac{(1-\nu)}{(1-\nu^c)}(1-f)^3\right]^{(1+\tilde{k})/(3+2\tilde{k})} \tag{3.36}$$

The results for the area bulk and transverse shear moduli for differential scheme are very similar to the results from the self-consistent method at small f, as they must be by design, but there are differences at large f. The two methods give very different results for the perfect-bonding case. Interestingly, however, in the pure-sliding limit, the shear moduli from the self-consistent and differential methods are almost indistinguishable numerically, although the functional forms are very different. This is illustrated in Fig. 3.4, where we look at the change in the shear modulus as $\tilde{k}$ is varied from perfect bonding to pure sliding for both methods. The dependence on $\tilde{k}$ is substantial, even at small f, where the results are exact and the same for the two schemes. Similar plots for the bulk modulus given by differential scheme show much less sensitivity to $\tilde{k}$. This is to be expected as the bulk modulus is independent of $\tilde{k}$ at small f.

3.5 THREE-DIMENSIONAL PARTICULATE COMPOSITE

The expressions for the effective properties of the particulate composite with rigid spherical particles are calculated in an analogous way to the two-dimensional example, so we will omit some of the details.

3.5.1 Dilute Result

The stresses and displacements for an isolated particle with spring-type interface are calculated in a standard way following GOODIER [29] or GHAHREMANI [30]. Then, the results are substituted directly in Eqn. (3.11) and the bulk modulus K^c and shear modulus μ^c are obtained as:

$$\frac{K^c}{K} = 1 + f\frac{3(1-\nu)}{(1+\nu)} \tag{3.37}$$

$$\frac{\mu^c}{\mu} = 1 + f\frac{15(1+2\tilde{k})(1-\nu)}{(17+16\tilde{k}) - (19+20\tilde{k})\nu} \tag{3.38}$$

Here, the notation is changed so that ν denotes the more conventional three-dimensional Poisson's ratio. The expressions given in (3.37) and (3.38) in the limit as $\tilde{k} \to \infty$ (perfect bonding) coincide with published results [3] [31]. Note that here the interface-sliding parameter $\tilde{k} = ka/4\mu$ and a is the radius of the sphere [this definition of $\tilde{k}$ differs by a factor of 2 from that used in two dimensions in (3.15)]. From the two elastic moduli, given in (3.37) and (3.38), the other quantities of interest, the Young's modulus E^c and the Poisson's ratio ν^c, can be obtained via:

$$E^c = \frac{9K^c\mu^c}{3K^c + \mu^c} \tag{3.39}$$

$$\nu^c = \frac{3K^c - 2\mu^c}{2(3K^c + \mu^c)} \tag{3.40}$$

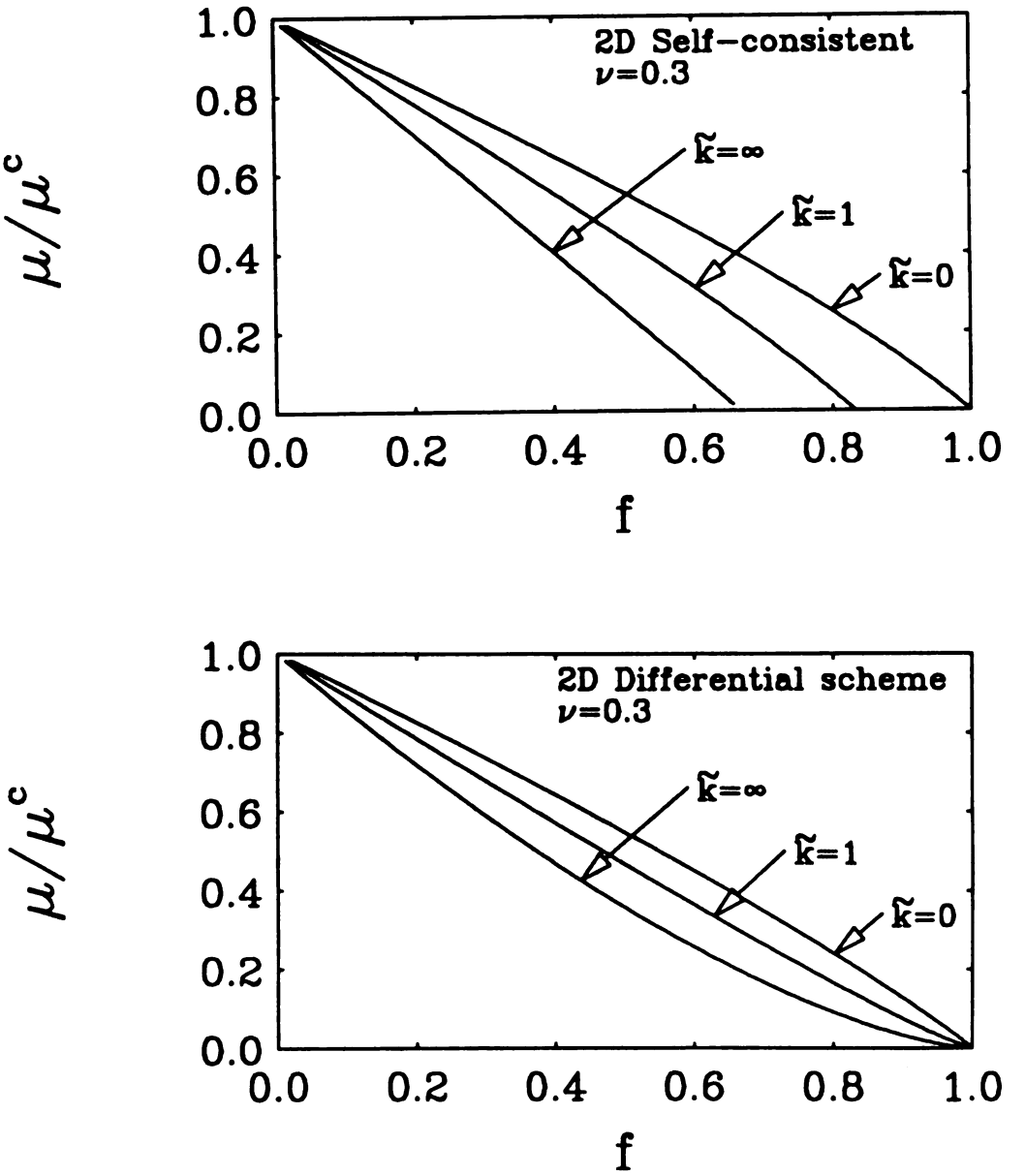

Figure 3.4: Transverse shear modulus μ^c, using both the self-consistent method and the differential scheme, is shown for various values of the interface-sliding parameter $\tilde{k}$ for area Poisson's ratio $\nu = 0.3$ for a unidirectional (two-dimensional) composite.

Similar relations to (3.39) and (3.40) exist for the matrix in the absence of inclusions if the superscripts are dropped from Eqns. (3.39) and (3.40).

3.5.2 Self-Consistent Solution

Again it is convenient to invert Eqns. (3.37) and (3.38) to give

$$\frac{K}{K^c} = 1 - f\frac{3(1-\nu)}{(1+\nu)} \tag{3.41}$$

$$\frac{\mu}{\mu^c} = 1 - f\frac{15(1+2\tilde{k})(1-\nu)}{(17+16\tilde{k}) - (19+20\tilde{k})\nu} \tag{3.42}$$

Self-consistency is most simply achieved by replacing ν by ν^c on the right hand side of (3.41) and (3.42) to give:

$$\frac{K}{K^c} = 1 - f\frac{3(1-\nu^c)}{(1+\nu^c)} \tag{3.43}$$

$$\frac{\mu}{\mu^c} = 1 - f\frac{15(1+2\tilde{k})(1-\nu^c)}{(17+16\tilde{k}) - (19+20\tilde{k})\nu^c} \tag{3.44}$$

Using (3.40), we form a single equation for ν^c

$$\frac{1+\nu}{1-2\nu} = \frac{1+\nu^c}{1-2\nu^c}\left\{\frac{1 - f\left[\frac{3(1-\nu^c)}{(1+\nu^c)}\right]}{1 - f\left[\frac{15(1+2\tilde{k})(1-\nu^c)}{(17+16\tilde{k})-(19+20\tilde{k})\nu^c}\right]}\right\} \tag{3.45}$$

which can be solved for ν^c numerically. The result is shown in Fig. 3.5. The fixed point (f^*, ν^*) is given by

$$\nu^* = \frac{2+\tilde{k}}{4+5\tilde{k}}$$

$$f^* = \frac{1+\tilde{k}}{1+2\tilde{k}} \tag{3.46}$$

For the perfect bonding case, the moduli become infinite at $f^* = 1/2$ and Poisson's ratio tends to a *universal value* $\nu^* = 1/5$. For the pure sliding case, the critical

volume fraction is $f^* = 1$, while the Poisson's ratio is $\nu^* = 1/2$, as illustrated in Fig. 3.5. Note that for the self-consistent method $f^* = (1+\nu^*)/[3(1-\nu^*)]$ for all values of $\tilde{k}$. The elastic moduli K^c and μ^c can be calculated by substituting ν^c in Eqns. (3.43) and (3.44). As in the two-dimensional composite, the moduli decrease as sliding increases.

3.5.3 Differential Scheme

Next, the differential scheme is employed. We use the dilute results for K^c and μ^c, and the constitutive relation (3.40) to give

$$\nu^c = \nu + 6f(1-\nu)(1-2\nu)\left[\frac{(2+\tilde{k}) - (4+5\tilde{k})\nu}{(17+16\tilde{k}) - (19+20\tilde{k})\nu}\right] \tag{3.47}$$

By iterating this equation as before, the following differential equation is obtained:

$$d\nu^c = 6\frac{df}{(1-f)}(1-\nu^c)(1-2\nu^c)\left[\frac{(2+\tilde{k}) - (4+5\tilde{k})\nu^c}{(17+16\tilde{k}) - (19+20\tilde{k})\nu^c}\right] \tag{3.48}$$

Integrating this result we obtain:

$$(1-f)^6 = \frac{(1-\nu)(1-2\nu^c)}{(1-\nu^c)(1-2\nu)}\left\{\frac{(1-2\nu)}{(1-2\nu^c)}\frac{[(2+\tilde{k}) - (4+5\tilde{k})\nu^c]}{[(2+\tilde{k}) - (4+5\tilde{k})\nu]}\right\}^{5(1+\tilde{k})/\tilde{k}} \tag{3.49}$$

Care must be taken in taking the pure sliding limit ($\tilde{k} = 0$) in Eqn. (3.49). The result is

$$(1-f)^6 = \frac{(1-\nu)(1-2\nu^c)}{(1-\nu^c)(1-2\nu)} exp\left[\frac{15}{4}\left(\frac{1}{1-2\nu} - \frac{1}{1-2\nu^c}\right)\right] \tag{3.50}$$

The elastic moduli are now obtained in a similar way to that described in the two dimensional case. The expression for μ^c is

$$\frac{\mu}{\mu^c} = \left[\frac{(1-\nu^c)(1-2\nu)}{(1-\nu)(1-2\nu^c)}(1-f)^6\right]^{(1+2\tilde{k})/[6(1+\tilde{k})]} \tag{3.51}$$

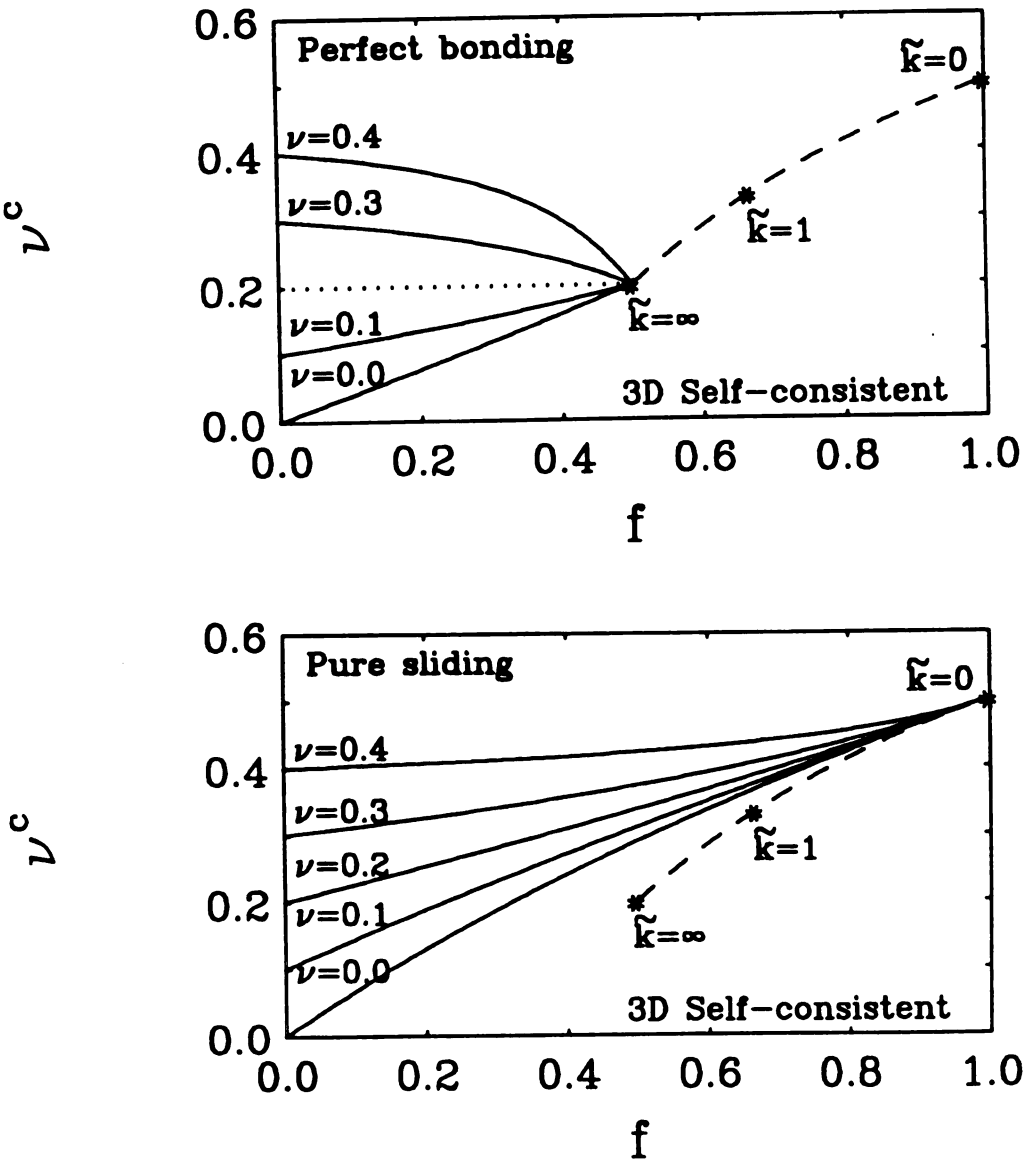

Figure 3.5: Flow diagram, using the self-consistent method, for the Poisson's ratio of the composite ν^c is shown for a particulate (three-dimensional) composite with perfect bonding ($\tilde{k} = \infty$) or pure sliding ($\tilde{k} = 0$) at the interfaces. For perfect bonding, the value of ν^c at the fixed point, $\nu^* = 1/5$ (indicated by the dotted line) and for pure sliding $\nu^* = 1/2$. The trajectory of the fixed point for various values of the interface-sliding parameter $\tilde{k}$ is indicated by a dashed line.

From a knowledge of μ^c and ν^c, the other elastic constants K^c and E^c can be found from (3.39) and (3.40). The bulk modulus K^c of the composite is given by:

$$\frac{K}{K^c} = \frac{(1+\nu)(1-2\nu^c)}{(1+\nu^c)(1-2\nu)} \left[\frac{(1-\nu^c)(1-2\nu)}{(1-\nu)(1-2\nu^c)} (1-f)^6 \right]^{(1+2\tilde{k})/[6(1+\tilde{k})]} \tag{3.52}$$

As in two dimensions, for shear modulus there is a remarkably strong dependence on $\tilde{k}$, even at small volume fraction f. Similar plots for the bulk modulus show much less sensitivity to $\tilde{k}$. Note that, as in two dimensions, in the pure sliding limit, the shear moduli from the self-consistent and the differential methods are almost indistinguishable numerically, although the functional forms are very different. The other two quantities, K^c and ν^c, are also remarkably similar in the pure-sliding limit from both the self-consistent theory and the differential scheme. This is in contrast to the perfect-bonding limit, where the two approaches give quite different results.

3.6 DISCUSSION

Fig. 3.2 and 3.3 illustrate the effective area Poisson's ratio for the unidirectional material (two dimensions) and Figs. 3.5 give the Poisson's ratio of the particular composite (three dimensions). Both the self-consistent method and the differential scheme exhibit a very interesting and characteristic behavior for the Poisson's ratio of the composite. The results obtained from these two methods vary significantly at higher volume fractions of inclusions, but for both methods Poisson's ratio of the composite tends to a *universal value*, which is independent of the Poisson's ratio of the matrix material, but does depend on the interface-sliding parameter $\tilde{k}$. For perfect bonding in two dimensions, $\nu^* = 1/3$ and for pure sliding $\nu^* = 1$. Other values of $\tilde{k}$ lead to $1/3 \leq \nu^* \leq 1$. For perfect bonding in three dimensions, $\nu^* = 1/5$ and for pure sliding $\nu^* = 1/2$. Other values of $\tilde{k}$ leads to $1/5 \leq \nu^* \leq 1/2$. These values of ν^* are the same for both the self-consistent method and the differential scheme, and are determined by the behavior in the dilute limit. It is important to know ν^*

for a given material, because, as it can be seen from Figs. 3.2, 3.3 and 3.5, it is rather easy to tell if the Poisson's ratio of composite will increase or decrease upon the further addition of rigid fibers. It is also important in determining the character of our effective medium solutions. We see that all materials "flow" toward ν^* as the percolation point, at which all the elastic moduli of the composite become infinite, is approached. This holds for both the self-consistent and the differential scheme, and therefore seems to be independent of the particular effective medium scheme used and is a rather robust result. Other models, such as three-phase [26] or composite spheres models [25] do not exhibit such a clear behavior, but the tendency is still there. Similar observations have also been made by ZIMMERMAN [32] for the case of material with holes or perfectly bonded rigid inclusions. This conclusion awaits an experimental verification.

It is interesting to observe that the self-consistent method shows a significant influence of the interface on the elastic constants, since the fixed point has a strong dependence on $\tilde{k}$. It is not entirely clear what is the physical origin of this strong dependence, but it will be commented on later. The numerical examples for the shear modulus are given in Figs. 3.4 for changing $\tilde{k}$. Note that as the interface-sliding parameter $\tilde{k}$ decreases the curves shift to the right, which implies that the shear modulus μ^c decreases as the degree of sliding increases, as shown by Eqn. (3.20). A similar observation can be made about the behavior of the bulk modulus K^c. Note that both the self-consistent approach and the differential scheme yield a solution for the bulk modulus which does depend on sliding. Recall, that for composites with spherical inclusions, for example, the other models such as composite with spherical inclusions, for example, the other models such as composite spheres model [25], three-phase model [26], and Mori-Tanaka method [14] [33] would give the result, which does *not* depend on sliding, since they assume that symmetry is maintained for whole range of f. For composites with rigid spherical particles the above three methods gives:

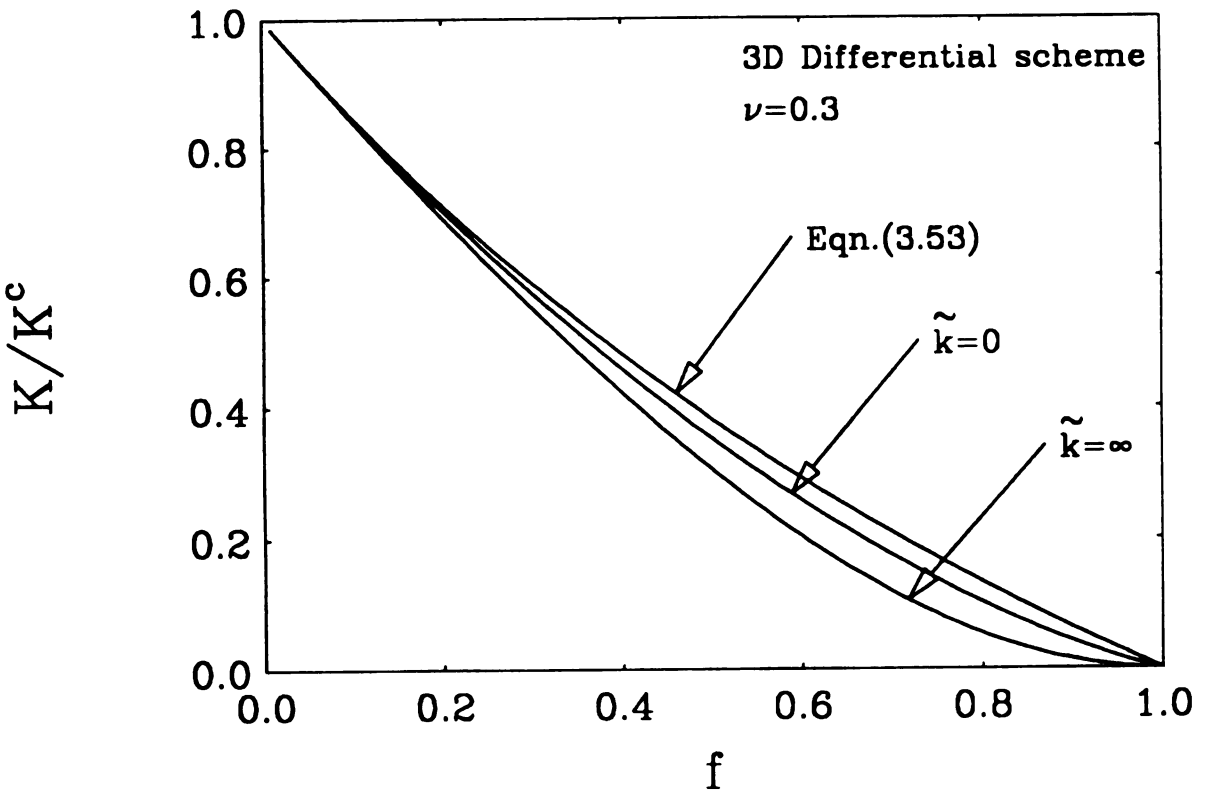

Figure 3.6: Comparison of the bulk modulus K^c given by the differential scheme for perfect bonding ($\tilde{k} = \infty$) and pure sliding ($\tilde{k} = 0$) and (3.53) for a particulate (three dimensional) composite with Poisson's ratio $\nu = 0.3$.

$$K^c = \frac{3K + 4f\mu}{3(1-f)} \tag{3.53}$$

for all $\tilde{k}$, which coincides with the perfect bonding solution [3]. The methods used in this chapter assume that the inclusions are randomly distributed in the matrix. But the randomness does not imply any local symmetry and locally every inclusion does undergo some degree of sliding, even under a macroscopic hydrostatic pressure. This local sliding decreases the effective bulk moduli of the composite. The comparison between Eqn. (3.53) and the differential scheme results for perfect bonding and pure sliding for composites with spherical particles is given in Fig. 3.6. Note that for a small volume fraction of inclusions both perfect bonding and pure sliding results coincide, but as the volume fraction increases the bulk modulus decreases due to sliding. It is interesting to note that Eqn. (3.53) gives results that are closer to the pure sliding limit than to the perfect bonding limit. This is somewhat counter-intuitive.

It might be noted that, for the special case of a composite in which the matrix has the same elastic properties as the inclusions, both the self-consistent method and the differential scheme give the result that the bulk modulus $K^c = K$, for all values of f and $\tilde{k}$. This is an exact result and provides a weak check on the reasonableness of both the self-consistent and the differential schemes. However, even in this special case, the shear modulus depends on both f and $\tilde{k}$, as expected.

Another interesting observation is that the dimensionless interface-sliding parameter $\tilde{k} \sim ka/\mu$ does include a "size effect". This has been observed by BENVENISTE [6], but was not discussed further. Note that the parameter k used in the boundary conditions (3.3) and (3.4) defines the resistance to sliding, which is an interface property. It is independent of the size of inclusions. Now, let us assume, for simplicity that the inclusions are of the same size. This assumption seems justified at least for the self-consistent method. Next, let us consider two composite systems with the same volume fraction f, one containing smaller inclusions and the other consisting of larger inclusions. Therefore, $\tilde{k}$ is smaller for the second case, which implies that the

composite with the larger inclusions, with interfaces defined by (3.3) and (3.4), will be stiffer than the composite with smaller inclusions. This seems reasonable, since in the second composite the surface area of inclusions is smaller, and, therefore the fictitious volume associated with a thin interface layer is smaller. This argument does not carry over to the pure sliding case when $\tilde{k} = k = 0$ or to the perfect bonding case when $\tilde{k} = k = \infty$, in which there is no size effect. For these two cases we may assume that the volume of the interface vanishes.

In this chapter the inclusions are assumed to be rigid for several reasons. One is simplicity, the other is that in that limit the differences between the various effective medium theories are greatest. Also, when the inclusion is much stiffer than the matrix the effect of the interface is more pronounced.

It is always very difficult to know what precisely is being described in effective medium theories, as the approximations are uncontrolled. In the two-dimensional case, for the composite with perfectly bonded rigid circular fibers, the self-consistent theory gives $f^* = 2/3$, which is within a percent or so of the percolation concentration (0.67) for randomly centered overlapping circles in two-dimensions [34]. An example of such an arrangement is shown in Fig. 3.7. Although we have not explicitly put in the overlapping or nonoverlapping of fibers in the theory, the result of the self-consistent approach only makes sense if we assume that the fibers can overlap. In this case it is clear that the cylinders must *bond perfectly* to each other when they overlap. For pure sliding, $f^* = 1$ and the critical point is only reached when the material is 100% fiber. Therefore, the implied boundary condition, in this case, is that the cylinders can slide perfectly past each other when they overlap. We conclude, from these two-dimensional results, that the self-consistent method implies the same boundary conditions between overlapping fibers as between fiber and matrix. Both are described by the interface-sliding parameter $\tilde{k}$. In the three-dimensional case, however, the fixed point and the percolation points do not coincide. The self-consistent method gives $f^* = 1/2$ for perfect bonding, whereas the corresponding value for overlapping

spheres from percolation theory is 0.29 [35] and the geometrical interpretation of the volume fraction at the critical point is not so clear. Again, for perfect bonding, $f^* = 1$, and the critical point is only reached when the material is 100% fiber. As noted previously, the elastic constants of composite obtained from the self-consistent method are strongly influenced by the value of f^*, as seen for example in Fig. 3.4. The above discussion on the possible overlaps and the boundary conditions between the inclusions may partially explain this strong dependence, However, the significant effect of interface on the bulk modulus seems hard to justify.

Both effective medium theories discussed in this chapter are based on the single inclusion solution. In the limit of small f, both methods reduce to the dilute fiber limit as would be expected. For larger values of f they provide us with approximate solutions for composites containing large volume fractions of inclusions. Our solutions become less reliable the larger f is. As we have mentioned, the self-consistent solution for the two-dimensional case may be appropriate to the unphysical case of overlapping fibers, all of which have the same diameter. The differential scheme is most appropriate for the case when there is a wide distribution of fiber diameters. Thus, caution must be used in applying either of these results to the physical case of high volume fraction of non-overlapping fibers all with the same diameter. For additional discussion on the several effective medium theories for the case of composites reinforced with perfectly bonded rigid spherical inclusions see the recent paper by CHRISTENSEN [31].

3.7 CONCLUSIONS

We investigate the effect of interface on the elastic properties of composites with randomly distributed inclusions. Initially, the solution for a single isolated sliding inclusion is obtained and this result is used in two separate effective medium theories: the self-consistent method and the differential scheme, to predict the elastic properties

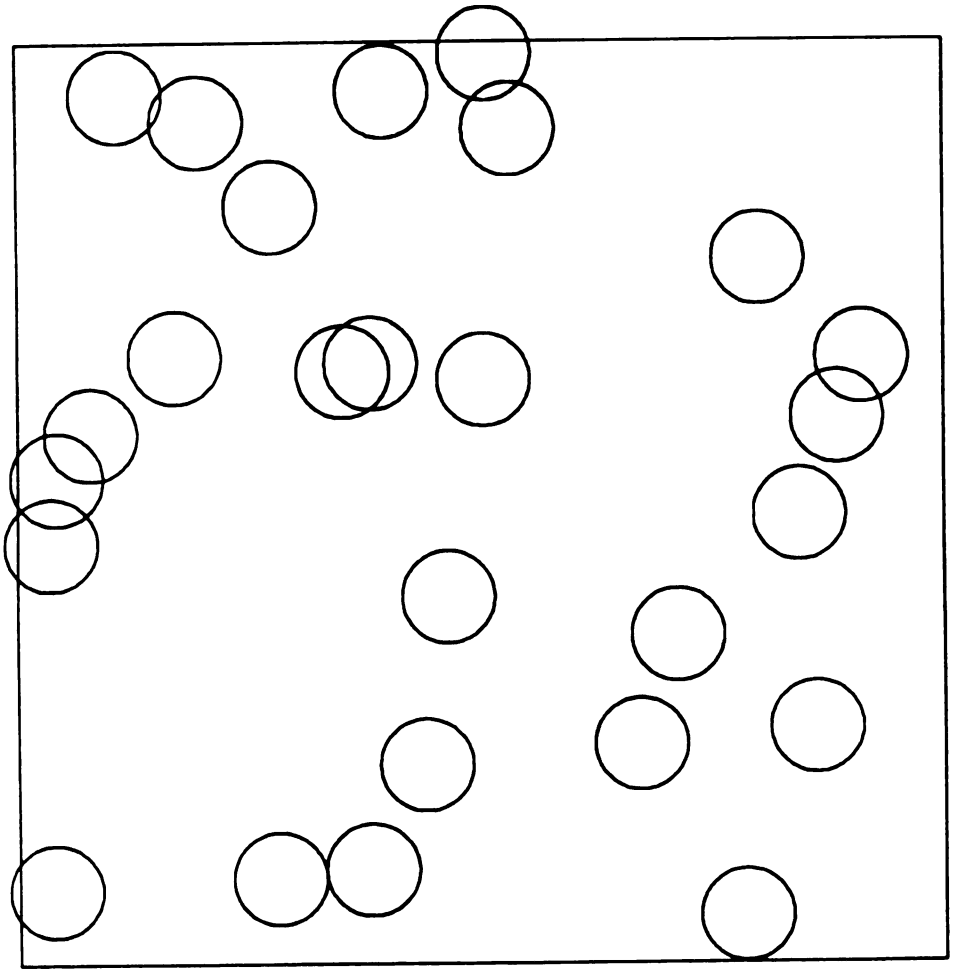

Figure 3.7: Sketch of a cross section through a unidirectional composite containing random arrangement of aligned fibers with a circular cross-section and volume fraction $f = 0.2$. The centers of the fibers were generated using pairs of random numbers, with overlaps allowed.

of composites containing a finite volume fraction of inclusions. For simplicity, the inclusions are assumed to be rigid. In the analysis, a parameter is introduced to describe the degree of sliding at the interface. Two limiting cases are perfect bonding and pure sliding at the inclusion-matrix interface. We show that the Poisson's ratio of the composite tends towards a universal value that is independent of the material parameters of the matrix, as the number of inclusions is increased. In contrast to the perfect-bonding case, both effective medium theories give remarkably similar results in the pure-sliding limit.

Bibliography

[1] T. Mura, Micromechanics of Defects in Solids, 2nd. edition, Martinus Nijhoff, Dordrecht (1987).

[2] Z. Hashin, J. Appl. Mech., **50**, 481 (1983).

[3] R. M. Christensen, Mechanics of Composite Materials, John Wiley, New York (1979).

[4] L. J. Broutman and B. D. Agarwal, Polym. Engng. Sci., **14**, 581 (1974).

[5] F. Lene and D. Leguillon, Int. J. Solids Struct., **18**, 443 (1982).

[6] Y. Benveniste, Mech. Mater., **4**, 197 (1985).

[7] J. Aboudi, Compos. Sci. Technol., **28**, 103 (1987).

[8] P. S. Steif and S. F. Hoysan, Mech. Mater., **6**, 197 (1987).

[9] P. S. Theocharis, Composite Interfaces, p.329, edited by H. Ishida and J. H. Koenig, North-Holland, New York (1986).

[10] F. H. J. Maurer, R. Simha and R. K. Jain, Composite Interfaces, p.367, edited by H. Ishida and J. H. Koenig, North-Holland, New York (1986).

[11] E. Sideridis, Compos. Sci. Technol., **31**, 35 (1988).

[12] N. J. Pagano and G. P. Tandon, Compos. Sci. Technol., **31**, 273 (1988).

[13] N. J. Pagano and G. P. Tandon, Mech. Mater., **9**, 49 (1990).

[14] Y. Benveniste, Mech. Mater., **6**, 147 (1987).

[15] J. D. Achenbach and H. Zhu, J. Mech. Phys. Solids, **37**, 381 (1989).

[16] I. Jasiuk and Y. Tong, Mechanics of Composite Materials and Structures, p.49, edited by J. N. Reddy and J. L. Teply, ASME, New York (1989).

[17] I. Jasiuk, J. Chen and M. F. Thorpe, Proc. Am. Soc. Compos., Fourth Technical Conference, p.513, Technomic, Lancaster (1989).

[18] Z. Hashin, Mech. Mater., **8**, 333 (1990).

[19] B. Budiansky, J. Mech. Phys. Solids, **13**, 223 (1965).

[20] R. Hill, J. Mech. Phys. Solids, **13**, 213 (1965).

[21] R. McLaughlin, Int. J. Engng Sci., **15**, 237 (1977).

[22] A. N. Norris, Mech. Mater., **4**, 1 (1985).

[23] S. P. Timoshenko and J. N. Goodier, Theory of Elasticity, 3rd. edition, McGraw-Hill, New York (1970).

[24] M. F. Thorpe and P. N. Sen, J. Acoust. Soc. Am., **77**, 1674 (1985).

[25] Z. Hashin and B. W. Rosen, J. Appl. Mech., **31**, 223 (1964).

[26] R. M. Christensen and K. H. Lo, J. Mech. Phys. Solids, **27**, 223 (1979).

[27] T. Mori and K. Tanaka, Acta Metall., **21**, 571 (1973).

[28] E. J. Garboczi and M. F. Thorpe, Phys. Rev. B, **31**, 7276 (1985).

[29] J. N. Goodier, ASME Trans., **55**, 39 (1933).

[30] F. Ghaharemani, Int. J. Solids Struct., **16**, 825 (1980).

[31] R. M. Christensen, J. Mech. Phys. Solids, **38**, 379 (1990).

[32] R. Zimmerman, presentation at Symposium on Micromechanics and Inhomogeneity at ASME Winter Annual Meeting, San Francisco, CA (1989).

[33] S. Shibata, I. Jasiuk, T. Mori and T. Mura, Mech. Mater., **9**, 229 (1990).

[34] W. Xia and M. F. Thorpe, Phys. Rev. A, **38**, 2650 (1988).

[35] V. K. S. Shante and S. Kirkpartick, Adv. Phys., **20**, 325 (1971).

Chapter 4

RIGID FIBER-REINFORCED COMPOSITES

4.1 INTRODUCTION

It is well known that fiber-reinforced composites can have better properties than conventional engineering materials, such as steel, aluminum, glass and carbon. Using composites to replace those single-component materials has become important in the polymer industry [1]. Recently, researchers have done extensively to understand toughening and crazing in composites by using finite element analysis [2] [3]. This standard technique is powerful when only a small number of fibers or particles are embedded in matrix. It is beyond current computational power to study the case in which hundreds of fibers or particles are randomly embedded in a matrix, which is a case that may occur in practical applications. In this chapter, we develop a *Digital-Imaged-Based* model which can easily handle such random systems.

For fiber-reinforced composites used in practice, such as graphite fiber tennis rackets, fibers are usually much stiffer than the matrix. This is where the name *fiber-reinforced* comes from. For example, glass is usually considered as an isotropic material and has Young's modulus of 76 GPa for E-Glass [4] [5]. Compared with the

Young's modulus of IMHS Epoxy, which is about 3.5 Gpa, glass is a very stiff material. Therefore, in glass-epoxy composite we can regard the glass fibers as perfectly rigid inclusions. This assumption not only simplifies mathematical calculations considerably, but also correctly gives the characteristic behavior of the composite. In this chapter, we study one of the typical interface conditions, that is, fibers are assumed to be perfectly adhered to the matrix. In other words, we assume the boundary condition on fiber-matrix interface is *perfect bonding.*

4.2 THEORY

4.2.1 Elasticity Theory for a Two-dimensional Isotropic System

For a two-dimensional isotropic system, there exist only two independent elastic constants. Once any two of the elastic constants are determined, all other elastic coefficients are obtained. Suppose we choose the Young's modulus E and Poisson's ratio ν as the two basic elastic constants, then the bulk modulus K, shear modulus μ and elastic stiffness constant C_{11} are obtained through the following equations [6].

$$K = \frac{E}{2(1-\nu)},$$

$$\mu = \frac{E}{2(1+\nu)},$$

$$C_{11} = \frac{E}{(1+\nu)(1-\nu)}. \tag{4.1}$$

4.2.2 Dilute Limit

When the area fraction of the rigid fibers is very small, the elastic moduli of composites can be obtained exactly [7]. For simplicity, let the fiber-matrix interface be *perfectly bonding*, which means that the fibers are *glued* together with the matrix and no sliding

on interfaces is allowed. Under these conditions, the effective elastic properties of composites, such as bulk modulus K, shear modulus μ, Young's modulus E and Poisson's ratio ν, can be obtained analytically through the following equations [7].

$$\frac{K_0}{K} = 1 - (1-p)\frac{2}{(1+\nu_0)},$$

$$\frac{\mu_0}{\mu} = 1 - (1-p)\frac{4}{(3-\nu_0)},$$

$$\frac{E_0}{E} = 1 - (1-p)\left[\frac{1-\nu_0}{1+\nu_0} + \frac{2(1+\nu_0)}{(3-\nu_0)}\right],$$

$$\nu = \nu_0 + (1-p)\frac{(1-\nu_0)(1-3\nu_0)}{3-\nu_0}. \tag{4.2}$$

where p is the area fraction of matrix and the subscript 0 denotes the quantities for the matrix. These results are only valid when $p \to 1$, that is when the area fraction of fibers is very small. It is also obviously true that the effective elastic moduli always increase when rigid fibers are added into matrix. But whether the Poisson's ratio of the composite increases or decreases depends upon the Poisson's ratio of the matrix. If $\nu_0 > 1/3$, then after adding some rigid inclusions into the matrix, the Poisson's ratio of composite decreases; otherwise it increases.

4.2.3 Results Near the Rigidity Threshold

When the area fraction of fibers increases, these fibers may touch each other at some critical value $p = p_c$. At this point, all of the elastic moduli go to infinity, and this is the rigidity threshold. For different ordered structures, p_c is different. When two rigid fibers are very close, the stress energy is confined to the narrow region between them, which we define as the *neck*.

In Fig. 4.1(a) and (b), we show the general case in which two rigid fibers are embedded in a matrix. In this configuration, there exist only two breakdown modes. One is the *compression mode* which is shown in Fig. 4.1(a), and the other one is the *shear mode*, which is shown in Fig. 4.1(b).

4.2.4 Compression Mode

In compression mode, the external force F acts on the fibers and pushes them together. F can be expressed as

$$F = A \mid \vec{u}_1 - \vec{u}_2 \mid = A\Delta u, \tag{4.3}$$

where Δu is the relative motion of the centers of two fibers under compression. A is the effective force constant which describes the relation between the external force and the relative motion of the fibers, and can be obtained by doing appropriate integration over the neck region. In Fig. 4.1(a), the x axis is drawn through the center of the neck, with the origin at the narrowest part. To the leading order, the width of the neck $W(x)$, at a distance x from the center, is obtained by doing parabolic approximation.

$$W(x) = w + \frac{x^2}{R}, \tag{4.4}$$

where w is the narrowest width of the neck and R is the radius of the two rigid fibers. Define R_c as the radius of the fibers when they get touched, we have

$$1 - p \sim R^2,$$

$$1 - p_c \sim R_c^2. \tag{4.5}$$

Since

$$R_c = R + \frac{w}{2}, \tag{4.6}$$

we have

$$\frac{w}{R} = \frac{p - p_c}{1 - p_c}. \tag{4.7}$$

When a small strip of the neck at distance x, with width dx and length $W(x)$, is under compression, the stress-strain relation is given by

$$\frac{dF}{dx} = C_{11}^0 \frac{\Delta u}{W(x)}, \tag{4.8}$$

where Δu is the relative motion of two rigid fibers and is independent of x, because the fibers are perfectly rigid; C_{11}^0 is the elastic stiffness constant of the matrix in the

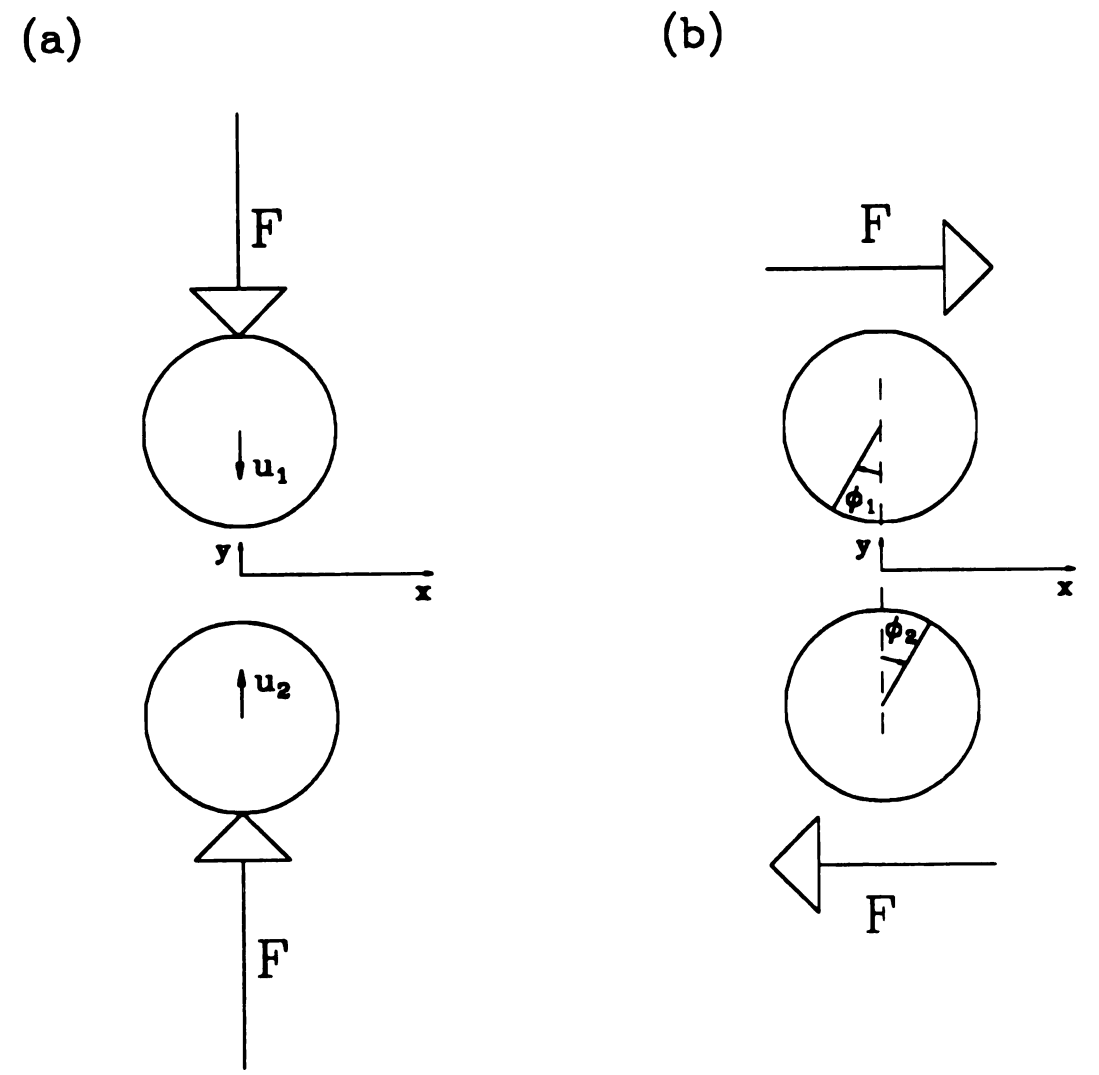

Figure 4.1: Showing the two modes in rigid fiber-reinforced composites. (a) Compression mode; (b) Shear mode.

direction of the external force F. This is a good approximation because this small strip is embedded in the matrix, and to the first order, we can assume that it is clamped by the surrounding matrix.

Integrating Eqn. 4.8, we get

$$F = \int_{-\infty}^{+\infty} C_{11}^0 \frac{\Delta u}{w + \frac{x^2}{R}} dx, \tag{4.9}$$

which gives the force constant A by using Eqn. (4.7).

$$A = \pi C_{11}^0 \sqrt{\frac{R}{w}} = \pi C_{11}^0 \left(\frac{1-p_c}{p-p_c}\right)^{\frac{1}{2}}. \tag{4.10}$$

4.2.5 Shear Mode

The force constant B for the shear mode is obtained similarly. When the neck is acted by a shear force F, as shown in Fig. 4.1(b), the two rigid fibers have a relative rotation $\Delta\phi = \mid \vec{\phi}_1 - \vec{\phi}_2 \mid$. Therefore,

$$\frac{dF}{dx} = \mu_0 \frac{R\Delta\phi}{W(x)}, \tag{4.11}$$

where μ_0 is the shear modulus of the matrix. Define $F = BR \mid \Delta\phi \mid$, and integrate Eqn. (4.11) from $-\infty$ to $+\infty$, we get

$$B = \pi\mu_0 \sqrt{\frac{R}{w}} = \pi\mu_0 \left(\frac{1-p_c}{p-p_c}\right)^{\frac{1}{2}}. \tag{4.12}$$

4.3 CRITICAL BEHAVIORS

In this section, we study the asymptotic formulas of the effective elastic moduli of composites when $p \to p_c$. Three ordered structures are studied, which are rigid fibers located on triangular superlattice, hexagonal superlattice and Kagomé superlattice. In each structure, we give the asymptotic formulas for effective Young's modulus E, bulk modulus K, shear modulus μ and the Poisson's ratio ν at the rigidity threshold.

4.3.1 Triangular Arrangement

In Fig. 4.2, we show such a composite under the external uniform strain ϵ_L in x direction, and there is no constrains on the composite in y direction. Therefore, by calculating the energy per unit area, we can find the effective Young's modulus E and Poisson's ratio ν. After that, all of the elastic moduli, such as bulk modulus K and shear modulus μ, are obtained by using Eqs. (4.1).

Let ϵ_L be the longitudinal strain applied to the composite in x direction, and ϵ_T be the corresponding transverse strain in y direction. Then we have

$$\epsilon_L = \frac{2u}{a},$$
$$\epsilon_T = \frac{2v}{\sqrt{3}a}, \tag{4.13}$$

where a is the intra-fiber distance and u, v are the displacements of the fibers shown in Fig. 4.2. Therefore, U, the energy per cell (shown by dash lines in Fig. 4.2) is obtained by calculating the energy stored in the corresponding necks. Define $\phi_0 = \pi/6$, we obtain

$$U = \frac{1}{2}A(2u)^2 + 2\left[\frac{1}{2}A(u\sin\phi_0 - v\cos\phi_0)^2 + \frac{1}{2}B(u\cos\phi_0 + v\sin\phi_0)^2\right]. \tag{4.14}$$

The area of this cell is

$$S_{cell} = \frac{\sqrt{3}}{2}a^2. \tag{4.15}$$

Thus, the energy per unit area is given by

$$\frac{U}{S_{cell}} = \frac{2}{\sqrt{3}a^2}\left[2Au^2 + \frac{1}{4}A(u - \sqrt{3}v)^2 + \frac{1}{4}B(\sqrt{3}u + v)^2\right]. \tag{4.16}$$

Minimize Eqn. (4.16) with respect to v (since there is no applied stress in the y direction), we get

$$\frac{v}{u} = \frac{\sqrt{3}(1 - \frac{B}{A})}{3 + \frac{B}{A}}. \tag{4.17}$$

The Poisson's ratio ν is obtained by using Eqs. (4.13) and (4.17)

$$\nu = \frac{\epsilon_T}{\epsilon_L} = \frac{1 - \frac{B}{A}}{3 + \frac{B}{A}}. \tag{4.18}$$

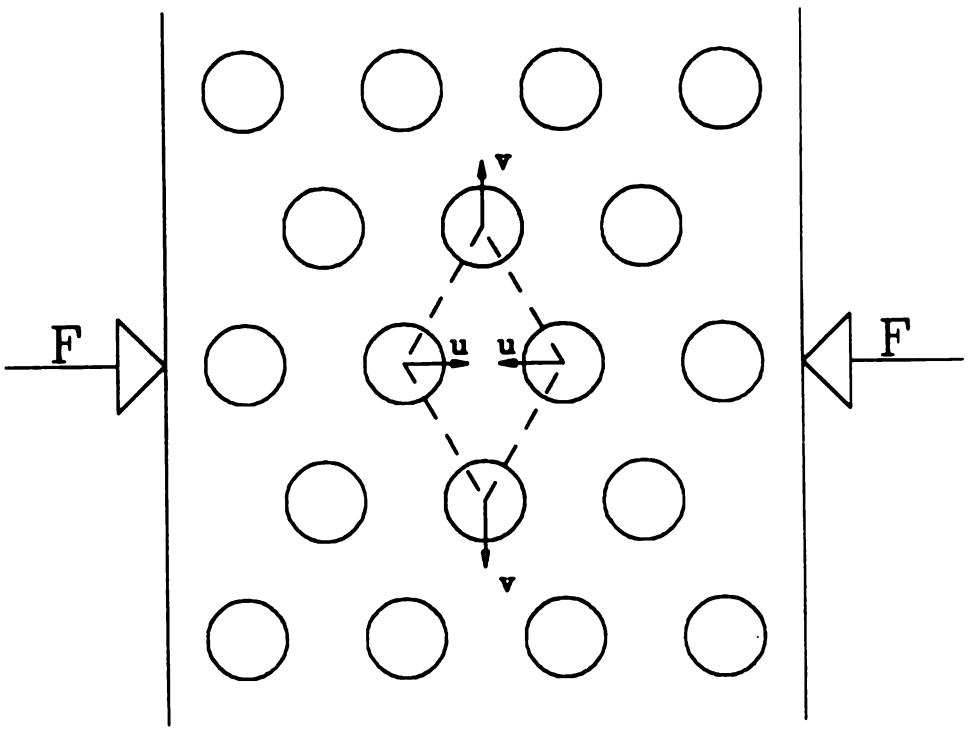

Figure 4.2: Showing the composites in which rigid fibers are located on triangular superlattice.

By definition

$$\frac{U}{S_{cell}} = \frac{1}{2} E \epsilon_L^2, \tag{4.19}$$

so the effective Young's modulus is

$$E = 2\sqrt{3} A \left(\frac{1 + \frac{B}{A}}{3 + \frac{B}{A}} \right). \tag{4.20}$$

Therefore, the effective bulk modulus and shear modulus are given by using Eqs. (4.1)

$$K = \frac{\sqrt{3}}{2} A,$$

$$\mu = \frac{\sqrt{3}}{4} (A + B). \tag{4.21}$$

where K relates only to the compression mode as expected.

From Eqs. (4.1), (4.10) and (4.12), we find

$$\frac{A}{B} = \frac{C_{11}^0}{\mu_0} = \frac{2}{1 - \nu_0}, \tag{4.22}$$

where ν_0 is the Poisson's ratio of the matrix. Therefore, by substituting Eqn. (4.22) into Eqs. (4.18), (4.20), (4.21), and using Eqs. (4.10), (4.12), we get

$$\nu = \frac{1 + \nu_0}{7 - \nu_0}, \tag{4.23}$$

$$\frac{K_0}{K} = \frac{(1 + \nu_0)}{\sqrt{3}\pi} \left(\frac{p - p_c}{1 - p_c} \right)^{\frac{1}{2}}, \tag{4.24}$$

$$\frac{\mu_0}{\mu} = \frac{4}{\sqrt{3}\pi} \left(\frac{1 - \nu_0}{3 - \nu_0} \right) \left(\frac{p - p_c}{1 - p_c} \right)^{\frac{1}{2}}, \tag{4.25}$$

$$\frac{E_0}{E} = \frac{1}{2\sqrt{3}\pi} \frac{(1 + \nu_0)(1 - \nu_0)(7 - \nu_0)}{(3 - \nu_0)} \left(\frac{p - p_c}{1 - p_c} \right)^{\frac{1}{2}}, \tag{4.26}$$

where p_c is given by

$$p_c = 1 - \frac{\pi}{2\sqrt{3}} \simeq 0.0931. \tag{4.27}$$

4.3.2 Hexagonal Arrangement

Another ordered structure consists of rigid fibers located on a hexagonal superlattice (Fig. 4.3). The effective elastic properties are obtained by using the same technique as we used in the above subsection. Define $\phi_0 = \pi/6$, then the total energy per cell (shown by dash lines in Fig. 4.3) is given by

$$U = \frac{1}{2}A(2v)^2 + 2\left[\frac{1}{2}A(u\cos\phi_0 + v\sin\phi_0 - w\sin\phi_0)^2 + \frac{1}{2}B(u\sin\phi_0 - v\cos\phi_0 + w\cos\phi_0)^2\right], \tag{4.28}$$

where u, v, w are defined in Fig. 4.3 and obey the following relation.

$$\epsilon_L = \frac{2u}{\sqrt{3}a},$$
$$\epsilon_T = \frac{2w + 2v}{3a}. \tag{4.29}$$

The area of this cell is

$$S_{cell} = \frac{3\sqrt{3}}{2}a^2. \tag{4.30}$$

Thus, the energy per unit area is given by

$$\frac{U}{S_{cell}} = \frac{4}{3\sqrt{3}a^2}\left[Av^2 + \frac{1}{8}A(\sqrt{3}u + v - w)^2 + \frac{1}{8}B(u - \sqrt{3}v + \sqrt{3}w)^2\right]. \tag{4.31}$$

Minimize Eqn. (4.31) with respect to v, w respectively and solve those equations, we find

$$v = 0,$$

and

$$\frac{w}{u} = \frac{\sqrt{3}(1 - \frac{B}{A})}{1 + 3\frac{B}{A}}. \tag{4.32}$$

Use Eqs. (4.29), (4.32) and the definition of Poisson's ratio $\nu = \epsilon_T/\epsilon_L$, we obtain

$$\nu = \frac{1 - \frac{B}{A}}{(1 + 3\frac{B}{A})}. \tag{4.33}$$

From Eqs. (4.1), (4.19), (4.29), (4.31) and (4.32), we get

$$E = \frac{4}{\sqrt{3}}\frac{B}{(1 + 3\frac{B}{A})},$$

$$K = \frac{A}{2\sqrt{3}},$$

$$\mu = \frac{1}{\sqrt{3}} \frac{B}{(1 + \frac{B}{A})}. \tag{4.34}$$

Thus, from Eqs. (4.10), (4.12) and (4.22), we get

$$\nu = \frac{1 + \nu_0}{5 - 3\nu_0}, \tag{4.35}$$

$$\frac{K_0}{K} = \frac{\sqrt{3}}{\pi}(1 + \nu_0)\left(\frac{p - p_c}{1 - p_c}\right)^{\frac{1}{2}}, \tag{4.36}$$

$$\frac{\mu_0}{\mu} = \frac{\sqrt{3}}{2\pi}(3 - \nu_0)\left(\frac{p - p_c}{1 - p_c}\right)^{\frac{1}{2}}, \tag{4.37}$$

$$\frac{E_0}{E} = \frac{\sqrt{3}}{4\pi}(1 + \nu_0)(5 - 3\nu_0)\left(\frac{p - p_c}{1 - p_c}\right)^{\frac{1}{2}}, \tag{4.38}$$

where p_c is given by

$$p_c = 1 - \frac{\pi}{3\sqrt{3}} \simeq 0.3954. \tag{4.39}$$

4.3.3 Kagomé Arrangement

Another interesting case is the Kagomé superlattice (Fig. 4.4). By defining $\phi_0 = \pi/6$ and assuming that the intra-fiber distance is $\sqrt{3}a$, we find that the total energy per unit cell U can be written as

$$\begin{aligned} U &= 2 \cdot \frac{1}{2} A u^2 \\ &+ 2\left\{\frac{1}{2} A \left[v \sin\phi_0 + w \cos\phi_0 - u \sin\phi_0\right]^2 + \frac{1}{2} B \left[w \sin\phi_0 - v \cos\phi_0 + u \cos\phi_0 - \frac{\sqrt{3}}{2} a\theta\right]^2\right\} \\ &+ 2\left\{\frac{1}{2} A \left[v \sin\phi_0 - w \cos\phi_0\right]^2 + \frac{1}{2} B \left[v \cos\phi_0 + w \sin\phi_0 - \frac{\sqrt{3}}{2} a\theta\right]^2\right\}. \end{aligned} \tag{4.40}$$

where the displacements u, v, w, and the rotational angle θ are defined in Fig. 4.4, and we also have the following relations

$$\epsilon_L = \frac{u}{\sqrt{3}a},$$

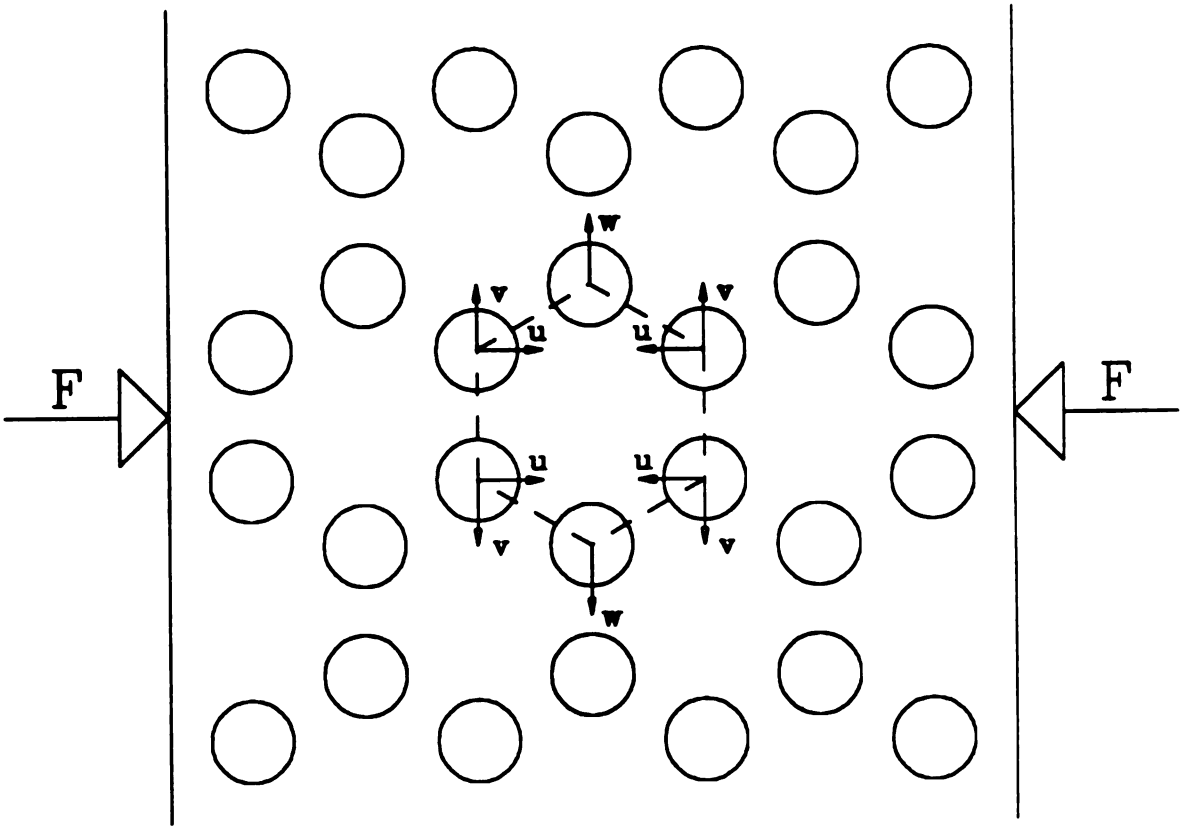

Figure 4.3: Showing the composites in which rigid fibers are located on hexagonal superlattice.

$$\epsilon_T = \frac{2w}{3a}. \tag{4.41}$$

The unit cell is shown by dash lines in Fig. 4.4, and its area is

$$S_{cell} = 6\sqrt{3}a^2. \tag{4.42}$$

Thus the total energy per unit area is

$$\begin{aligned}\frac{U}{S_{cell}} = Au^2 \;+\; & \frac{1}{4}A(v-u+\sqrt{3}w)^2 + \frac{1}{4}B(w-\sqrt{3}v+\sqrt{3}u-\sqrt{3}a\theta)^2 \\ + \; & \frac{1}{4}A(v-\sqrt{3}w)^2 + \frac{1}{4}B(\sqrt{3}v+w-\sqrt{3}a\theta)^2,\end{aligned} \tag{4.43}$$

Minimize Eqn. (4.43) with respect to v, w, θ respectively, we get

$$v = \frac{1}{2}u,$$

$$w = \frac{1}{2\sqrt{3}}u,$$

$$\frac{\sqrt{3}}{2}u + w - \sqrt{3}a\theta = 0. \tag{4.44}$$

Thus, by using Eqs. (4.41) and (4.44), we find

$$\nu = \frac{\epsilon_T}{\epsilon_L} = \frac{1}{3}. \tag{4.45}$$

Substituting Eqs. (4.44) into (4.43), and using Eqn. (4.19), we obtain the effective Young's modulus

$$E = \frac{1}{\sqrt{3}}A, \tag{4.46}$$

From Eqs. (4.1), we get the bulk modulus and shear modulus are

$$K = \frac{\sqrt{3}}{4}A,$$

$$\mu = \frac{\sqrt{3}}{8}A. \tag{4.47}$$

Combining Eqs. (4.10), (4.46) and (4.47), we obtain the elastic moduli for Kagomé arrangement:

$$\frac{K_0}{K} = \frac{2}{\sqrt{3}\pi}(1+\nu_0)\left(\frac{p-p_c}{1-p_c}\right)^{\frac{1}{2}}, \tag{4.48}$$

$$\frac{\mu_0}{\mu} = \frac{4}{\sqrt{3}\pi}(1-\nu_0)\left(\frac{p-p_c}{1-p_c}\right)^{\frac{1}{2}}, \tag{4.49}$$

$$\frac{E_0}{E} = \frac{\sqrt{3}}{\pi}(1+\nu_0)(1-\nu_0)\left(\frac{p-p_c}{1-p_c}\right)^{\frac{1}{2}}, \tag{4.50}$$

where p_c is given by

$$p_c = 1 - \frac{\sqrt{3}\pi}{8} \simeq 0.3198. \tag{4.51}$$

4.4 IMPROVEMENTS IN THE BULK MODULUS AT RIGIDITY THRESHOLD

In Eqs. (4.24), (4.36) and (4.48), we have the expressions for the bulk modulus to the leading order. These formulas can be improved by including the next order term enabling us to describe the critical behavior over a larger range of p.

In Fig. 4.5(a), we show three rigid fibers with radius R located on a triangular superlattice. This time we use the full expression for $W(x)$ rather than the parabolic approximation. We redefine W as a function of θ by using $x = R\sin\theta$, where θ is the angle relative to the line joining the centers of two nearest fibers.

$$W(\theta) = w + 2R(1-\cos\theta). \tag{4.52}$$

Defining $\phi_0 = \pi/6$ and $b = W(\phi_0)$, we can decompose Fig. 4.5(a) into three necks (θ from 0 to ϕ_0) plus an equilateral triangular of matrix with side length b. Suppose this composite is under a hydrostatic pressure which induces an uniform radial strain ϵ, then the force constant for compression mode is obtained through

$$F = C_{11}^0 \Delta u \int_{-\phi_0}^{+\phi_0} \frac{d(R\sin\theta)}{W(\theta)}. \tag{4.53}$$

Doing this integral and using Eqn. (4.52), we get the force constant for compression mode

$$A = C_{11}^0 \pi \left[\left(\frac{1-p_c}{p-p_c}\right)^{\frac{1}{2}} - \frac{\phi_0}{\pi} - \frac{1}{\pi\tan\frac{\phi_0}{2}}\right]. \tag{4.54}$$

The total energy is the energy stored in the necks plus the energy stored in the central equilateral triangular piece of matrix. Noticing that only 3/2 necks are involved inside the equilateral triangle with side length a, we get

$$\frac{3}{2}\cdot\frac{1}{2}A(\epsilon a)^2+\frac{\sqrt{3}}{4}b^2\cdot 2K_0\epsilon_0^2=\frac{\sqrt{3}}{4}a^2\cdot 2K\epsilon^2, \tag{4.55}$$

where ϵ_0 is the uniform strain in the inner equilateral triangular matrix. Since

$$\epsilon=\frac{\Delta u}{a},$$

$$\epsilon_0=\frac{\Delta u}{b}, \tag{4.56}$$

we have

$$\frac{\epsilon_0}{\epsilon}=\frac{a}{b}. \tag{4.57}$$

Combining Eqn. (4.55) and (4.57), we get

$$\frac{K_0}{K}=\frac{1}{\alpha}\left(\frac{p-p_c}{1-p_c}\right)^{\frac{1}{2}}\left[1-\frac{\beta}{\alpha}\left(\frac{p-p_c}{1-p_c}\right)^{\frac{1}{2}}\right], \tag{4.58}$$

where

$$\alpha=\frac{\sqrt{3}\pi}{1+\nu_0},$$

$$\beta=1-\alpha\left(\frac{1}{6}+\frac{1}{\pi\tan\frac{\pi}{12}}\right). \tag{4.59}$$

The modified formulas for hexagonal and Kagomé arrangements are obtained in a similar way, as shown in Fig. 4.5(b), (c). The intra-fiber distance for hexagonal arrangement is (Fig. 4.5)

$$a=w+2R, \tag{4.60}$$

where w is the narrowest width of the neck and R is the radius of the fibers. The side length of the inner hexagonal matrix is

$$b=W(\phi_0)=w+2R(1-\cos\phi_0)=w+R, \tag{4.61}$$

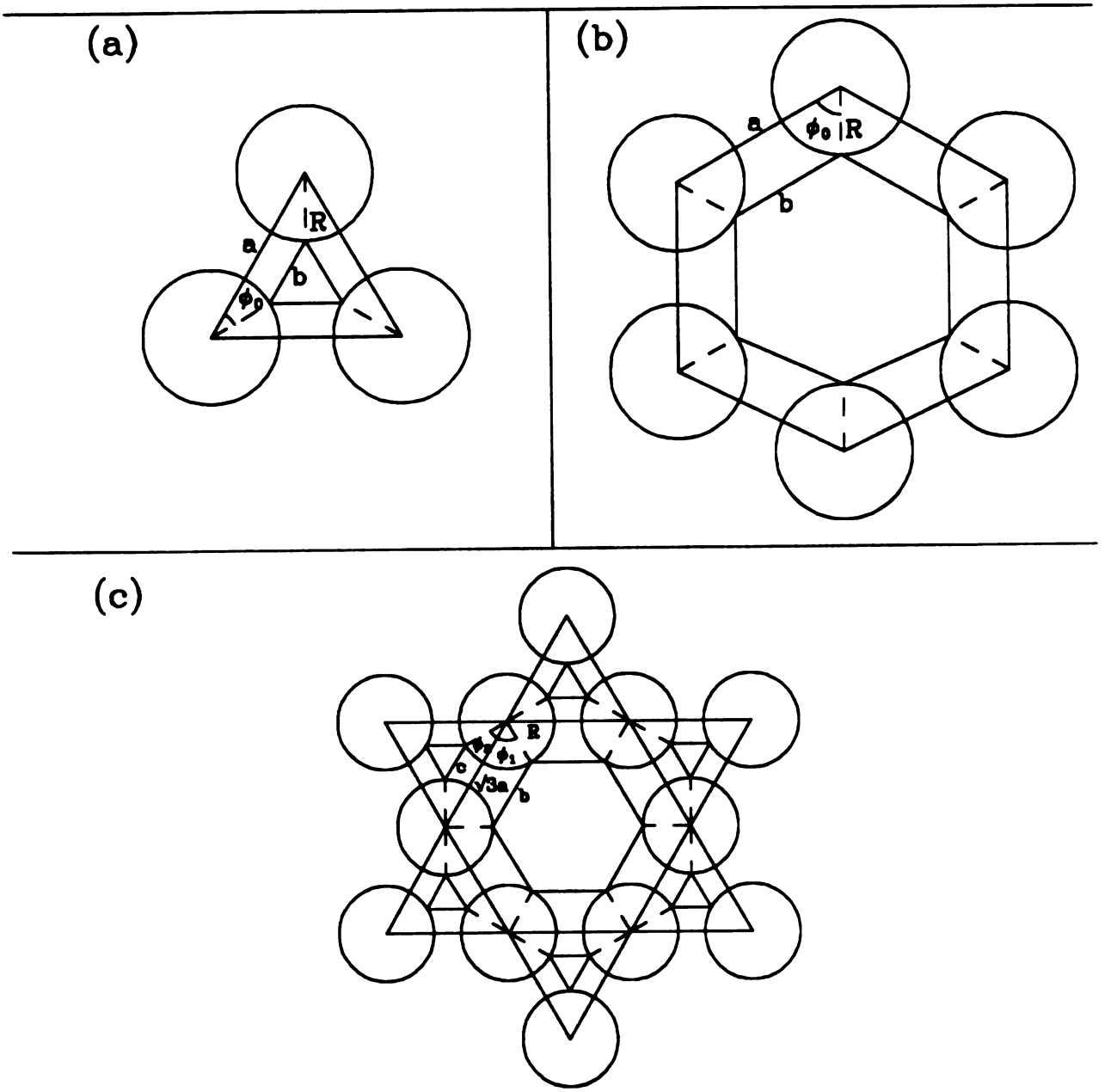

Figure 4.5: Showing the configuration used for calculating modified bulk modulus. (a) Triangular arrangement; (b) Hexagonal arrangement; (c) Kagomé arrangement.

where $\phi_0 = \pi/3$. Under hydrostatic pressure, the centers of two nearest fibers are compressed by an amount Δu. Thus, the force caused by this compression is given by

$$F = C_{11}^0 \Delta u \int_{-\phi_0}^{+\phi_0} \frac{d(R\sin\theta)}{W(\theta)}, \tag{4.62}$$

which gives out the force constant through definition $F = A\Delta u$.

$$A = C_{11}^0 \pi \left[\left(\frac{1-p_c}{p-p_c} \right)^{\frac{1}{2}} - \frac{\phi_0}{\pi} - \frac{1}{\pi \tan\frac{\phi_0}{2}} \right]. \tag{4.63}$$

Since the necks on the boundary of this cell (shown by dash lines in Fig. 4.5) are shared with its neighbors, there are only 3 *full* necks belonging to this cell. Also, by noticing the area of this cell is $6 \cdot \frac{\sqrt{3}}{4}a^2$, and the area of the inner hexagonal matrix is $6 \cdot \frac{\sqrt{3}}{4}b^2$, we can define the effective area bulk modulus K through the following equation.

$$3 \cdot \frac{1}{2}A(\epsilon a)^2 + 6 \cdot \frac{\sqrt{3}}{4}b^2 \cdot 2K_0\epsilon_0^2 = 6 \cdot \frac{\sqrt{3}}{4}a^2 \cdot 2K\epsilon^2, \tag{4.64}$$

where ϵ is the uniform strain on the composite caused the hydrostatic pressure, and ϵ_0 is the strain inside the inner hexagonal matrix. Since

$$\epsilon = \frac{\Delta u}{a},$$

$$\epsilon_0 = \frac{\Delta u}{b}, \tag{4.65}$$

we get

$$\epsilon_0 = \epsilon \left(\frac{a}{b} \right). \tag{4.66}$$

Solve Eqn. (4.64) by using relation (4.66), we get

$$K = \frac{1}{2\sqrt{3}}A + K_0. \tag{4.67}$$

Thus, combining Eqs. (4.63) and (4.67), we have

$$\frac{K}{K_0} = \frac{\pi}{\sqrt{3}(1+\nu_0)} \left[\sqrt{\frac{R}{w}} - \frac{\phi_0}{\pi} - \frac{1}{\pi \tan\frac{\phi_0}{2}} \right] + 1. \tag{4.68}$$

Keeping the leading two terms and using $w/R = (p - p_c)/(1 - p_c)$, we have

$$\frac{K_0}{K} = \frac{1}{\alpha}\left(\frac{1-p_c}{p-p_c}\right)^{\frac{1}{2}}\left[1 - \frac{\beta}{\alpha}\left(\frac{1-p_c}{p-p_c}\right)^{\frac{1}{2}}\right], \tag{4.69}$$

where

$$\alpha = \frac{\pi}{\sqrt{3}(1+\nu_0)},$$

$$\beta = 1 - \alpha\left(\frac{1}{3} + \frac{1}{\pi \tan\frac{\pi}{6}}\right). \tag{4.70}$$

For Kagomé arrangement, we can get the modified bulk modulus in the same way. Referring to Fig. 4.5 the intra-fiber distance is assumed to be $\sqrt{3}a$. So we have

$$\sqrt{3}a = w + 2R. \tag{4.71}$$

Assume that the relative movement of nearest fibers is Δu under a hydrostatic pressure, which induces a strain $\epsilon = \Delta u/\sqrt{3}a$ on the composite. The force acted on a neck due to this hydrostatic pressure is,

$$F = C_{11}^0 \Delta u \int_{-\phi_2}^{+\phi_1} \frac{d(R\sin\theta)}{W(\theta)}, \tag{4.72}$$

which gives out the force constant through definition $F = A\Delta u$.

$$\begin{aligned} A &= -\frac{1}{2}C_{11}^0(\phi_1+\phi_2) + C_{11}^0\sqrt{\frac{R}{w}}\frac{1+\frac{w}{2R}}{\sqrt{1+\frac{w}{4R}}} \\ &\left[\arctan\left(\frac{2\left(\tan\frac{\phi_1}{2}\right)\sqrt{1+\frac{w}{4R}}}{\sqrt{\frac{w}{R}}}\right) + \arctan\left(\frac{2\left(\tan\frac{\phi_2}{2}\right)\sqrt{1+\frac{w}{4R}}}{\sqrt{\frac{w}{R}}}\right)\right], \end{aligned} \tag{4.73}$$

where $\phi_1 = \pi/3$ and $\phi_2 = \pi/6$.

Let the side length of the inner hexagonal matrix be b, and the strain inside it be ϵ_1. Let the side length of the corner equilateral triangular matrix is c, and the strain inside it be ϵ_2. By noticing that the fibers are perfectly rigid, we have

$$\epsilon_1 = \frac{\Delta u}{b},$$

$$\epsilon_2 = \frac{\Delta u}{c}. \tag{4.74}$$

Therefore,

$$\epsilon_1 = \epsilon\left(\frac{\sqrt{3}a}{b}\right),$$

and

$$\epsilon_2 = \epsilon\left(\frac{\sqrt{3}a}{c}\right). \tag{4.75}$$

By calculating the total energy inside this primitive cell, as shown in Fig. 4.5, we have

$$6\cdot\frac{1}{2}A\left[\epsilon(2a\cos\phi_2)\right]^2 + 6\frac{\sqrt{3}}{4}b^2\cdot 2K_0\epsilon_1^2 + 2\cdot\frac{\sqrt{3}}{4}c^2\cdot 2K_0\epsilon_2^2 = 6\frac{\sqrt{3}}{4}(2a)^2\cdot 2K\epsilon^2. \tag{4.76}$$

Solve Eqn. (4.76) by using Eqn. (4.75), we get

$$K = \frac{\sqrt{3}}{4}A + K_0. \tag{4.77}$$

From Eqs. (4.73), (4.77) and keeping only the first two leading terms, we obtained the effective bulk modulus.

$$\frac{K_0}{K} = \frac{1}{\alpha}\left(\frac{1-p_c}{p-p_c}\right)^{\frac{1}{2}}\left[1-\frac{\beta}{\alpha}\left(\frac{1-p_c}{p-p_c}\right)^{\frac{1}{2}}\right], \tag{4.78}$$

where

$$\alpha = \frac{\sqrt{3}\pi}{2(1+\nu_0)},$$

$$\beta = 1 - \frac{\sqrt{3}\pi}{8(1+\nu_0)}, \tag{4.79}$$

and

$$p_c = 1 - \frac{\sqrt{3}\pi}{8} \approx 0.3198. \tag{4.80}$$

It should be noted that Eqs. (4.58), (4.69), (4.78) are exactly the same as Eqs. (4.24), (4.36), (4.48), except that a higher order term in $(\frac{p-p_c}{1-p_c})$ has been included.

4.5 EFFECTIVE MEDIUM THEORY

For a composite with randomly distributed fibers embedded in a matrix, we can use effective medium theory to calculate its effective elastic properties approximately. One of the effective medium theories is the *self-consistent method*, and the other one is the *three-phase model*, which is a more sophisticated method. In self-consistent method, the elastic properties are obtained by solving the following equations [7].

$$\frac{1+\nu_0}{1-\nu_0} = \frac{1+\nu}{1-\nu}\left\{\frac{1-2(1-p)/(1+\nu)}{1-4(1-p)/(3-\nu)}\right\},$$

$$\frac{K_0}{K} = 1-(1-p)\frac{2}{(1+\nu)},$$

$$\frac{\mu_0}{\mu} = 1-(1-p)\frac{4}{(3-\nu)},$$

$$\frac{4}{E} = \frac{1}{K}+\frac{1}{\mu}. \tag{4.81}$$

In three-phase model, the elastic moduli are given by [8]

$$\frac{K_0}{K} = \frac{p}{1+(1-p)\left(\frac{1-\nu_0}{1+\nu_0}\right)},$$

$$\frac{\mu_0}{\mu} = \frac{-\beta+\sqrt{\beta^2-4\alpha\gamma}}{2\alpha}, \tag{4.82}$$

where

$$f = 1-p,$$

$$\eta = \frac{3-\nu_0}{1+\nu_0},$$

$$a = \frac{f^2+1}{\eta+1},$$

$$b = f^2+(\eta-1)f,$$

$$c = 1,$$

$$d = (\eta - 3)f^3 + 3f^2,$$

$$e = \frac{3}{2}f^2 - \frac{1}{2}f^3(\eta + 3),$$

$$g = \frac{1}{2},$$

$$h = 2(1 - f^2)(\eta + 1),$$

$$i = 2[(\eta + 1)f + f^2],$$

$$\alpha = bd - ei + b + gi + cd + 2e,$$

$$\beta = ad + eh + a - gh - 2(bd - ei) + (b + gi)(\eta - 1) - (cd + 2e)(\eta + 3),$$

$$\gamma = -ad - eh + \eta(a - gh) + bd - ei - \eta(b + gi) + (cd + 2e)(2 + \eta). \tag{4.83}$$

The Poisson's ratio and Young's modulus are obtained from Eqs. (4.82),

$$\nu = \frac{\frac{1+\nu_0}{1-\nu_0}\frac{\mu_0/\mu}{K_0/K} - 1}{\frac{1+\nu_0}{1-\nu_0}\frac{\mu_0/\mu}{K_0/K} + 1},$$

$$\frac{E_0}{E} = \frac{K_0}{K}\left(\frac{1-\nu_0}{1-\nu}\right). \tag{4.84}$$

4.6 SIMULATON RESULTS

We use a spring-grid-scheme to calculate the transverse effective elastic moduli of fiber-reinforced materials [9] [10]. This method has been discussed in detail in **Chapter 2**.

In our simulation, we use a 210 × 210 triangular lattice as a unit supercell and impose periodic boundary conditions. We use two sets of spring constants α, β and γ. One set is chosen to give the elastic constants of the continuum matrix, in which α, β, γ are all of order 1. The other set is chosen to be $\alpha = \beta = \gamma = 1000$, which simulates the rigid fibers. We find that the 1000 : 1 ratio is rigid enough to give accurate results by comparing to another program in which the rigid fibers are *perfectly* rigid (imposed by a bonding condition on the fiber interface). We found that the results are the same within computational errors.

After setting the configuration, we impose an external uniform strain in x direction, $e_{xx} = 0.001$, on the unit cell and let the system relax with no constrains in y direction. We use *Conjugate Gradient Method* [11] to obtain the stresses. By calculating the energy per unit area and by measuring the change of the length of the cell in y direction, we find Young's modulus E and Poisson's ratio ν. After that, all other elastic constants are known through Eqs. (4.1).

For ordered structures, we did the simulation on three different arrangement of rigid fibers: triangular, hexagonal and Kagomé arrangements. We show the flow diagram for Poisson's ratio in Fig. 4.6(a), (b) and (c). We plot the analytical results in the dilute region by using Eqs. (4.2), as shown by solid lines in those figures. The interesting point is that in general there exists **no** fixed points in these diagrams. This is quite different from the results we obtained from self-consistent method in which the existence of fixed points is predicted. Also, our results show the difference between porous composites and fiber-reinforced composites. In porous composites, the fixed point always exists in the flow diagram for Poisson's ratio, which is independent of the size and the shape of the holes. Recently, this result has been verified by computer simulations [9] and has been proven analytically [12] [13]. This is true because there exits only one independent elastic constant in porous composites. Therefore, all of the elastic constants are scaled to this unique parameter near rigidity threshold, which makes Poisson's ratio become a constant. But this argument is not true in fiber-

reinforced composites, because in this case energy comes from two modes, compression and shear. As we have seen from Eqs. (4.10) and (4.12), the compression mode basically relates to the elastic constant C_{11} and the shear mode relates to the shear modulus μ. Therefore, in general, the elastic moduli of fiber-reinforced composites with perfect bonding at the interface depend upon two independent parameters of the matrix rather than one. Therefore, no universal curve exists for the effective elastic moduli, which means that the fixed point in fiber-reinforced composites does not exist in general. We have also studied the same structure recently by using *Finite Element Analysis* with the commercial software *ABAQUS* [14] and obtained the same conclusion.

Under certain arrangement of rigid fibers, say the Kagomé arrangement, a fixed point does exist in the Poisson's ratio flow diagram, because of the special symmetry of this arrangement. This result has been proven analytically in Eqn. (4.45) and has been verified by our simulation results (Fig. 4.6(c)). Therefore, our conclusion is that *the fixed point in Poisson's ratio flow diagram does not exist in general for fiber-reinforced composites, but it can exist in certain cases with special symmetry.* If the boundary condition is *pure sliding* on the fiber-matrix interface, which means that there is no friction force on interfaces, then there will be no shear mode in the energy expression. Therefore, all of the elastic moduli scale to one elastic constant of matrix again, which always gives a fixed point in the Poisson's ratio flow diagram. (See **Chapter 5** for details)

A big advantage of the Digital-Image-Based method used here is that it is easy to study the case in which hundreds of fibers are embedded in matrix, whereas Finite Element Modeling has no such ability at present [14]. For the overlapping fiber case, a configuration is generated by randomly placing fibers on the matrix. The center of the rigid fibers are determined by a random number generator. For the nonoverlapping case, we use the Metropolis version of the Monte Carlo method to generate configurations [10] [15]. The unit cell is still 210×210 and the diameter of

the rigid fibers is chosen to be 11. For this choice of the diameter, there are enough pixels inside a rigid fiber, which makes the surfaces of the fibers are smooth enough after digitalizing.

In Fig. 4.6(d), we show the Poisson's ratio flow diagram for both overlapping (represented by symbol $\diamond$) and nonoverlapping (represented by symbol $\bullet$) cases. The solid lines are the results obtained from self-consistent method [7] and the dash lines are the results of three-phase model [8]. In both cases, we did the average over 6 configurations and the error bars are shown in this figure. As we see from Fig. 4.6(d), three-phase model is better than the self-consistent method, in the sense that it agrees with the simulation data that no fixed point exists in Poisson's ratio flow diagram for random fiber-reinforced composites. It is also true that the data for nonoverlapping case is close to the prediction of the three-phase model, and the data for overlapping case is close to the prediction of the self-consistent method. This result is expected because of the nature of those two effective medium methods.

In Fig. 4.7 we also plotted the area bulk modulus with respect to the area fraction of matrix. In Fig. 4.7(a), (b) and (c), the solid lines around $p = 1$ are the exact results in the dilute region, which are given by Eqs. (4.2); the solid lines around the rigidity threshold p_c are the improved area bulk modulus obtained by Eqs. (4.58), (4.69) and (4.78); the dash lines around p_c are results given by Eqs. (4.24), (4.36) and (4.48), which are the lowest order results. In Fig. 4.7(d), the solid lines are the analytical results obtained from self-consistent method by using Eqn. (4.81), and the dash lines are the results obtained from three-phase model by using Eqn. (4.82). It is obvious that our simulation data agrees very well with the theoretical analysis. In dilute limit, simulation data agree nicely with analytical results until $p = 0.8$. Around the rigidity threshold, the analytical results can explain the simulation data up to $p - p_c = 0.2$. Again, it is still true that three-phase model gives better results for nonoverlapping case, and the self-consistent method agrees more closely to the overlapping case.

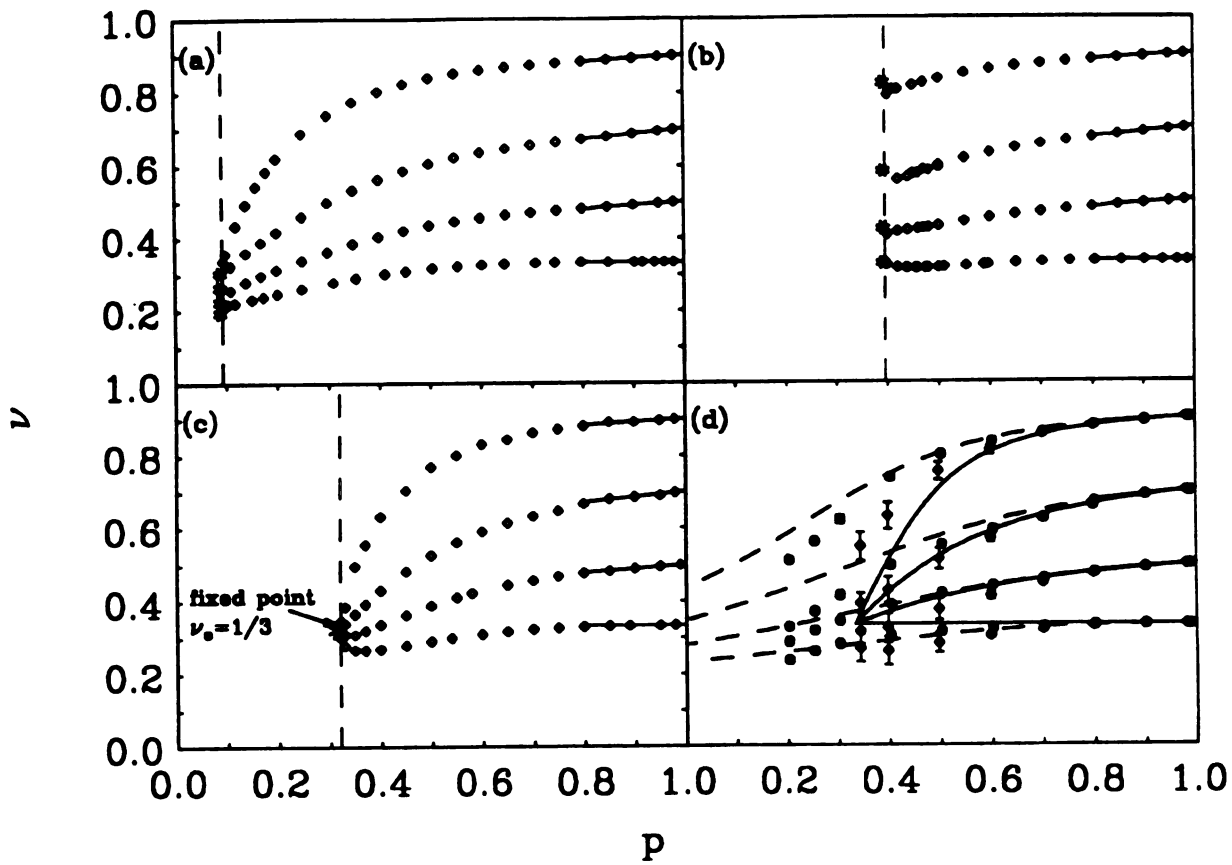

Figure 4.6: Showing the poisson's ratio flow diagram for different arrangements of rigid fibers. (a) Triangular arrangement; (b) Hexagonal arrangement; (c) Kagomé arrangement; (d) Random arrangements, symbol ◇ for overlapping case and • for nonoverlapping case.

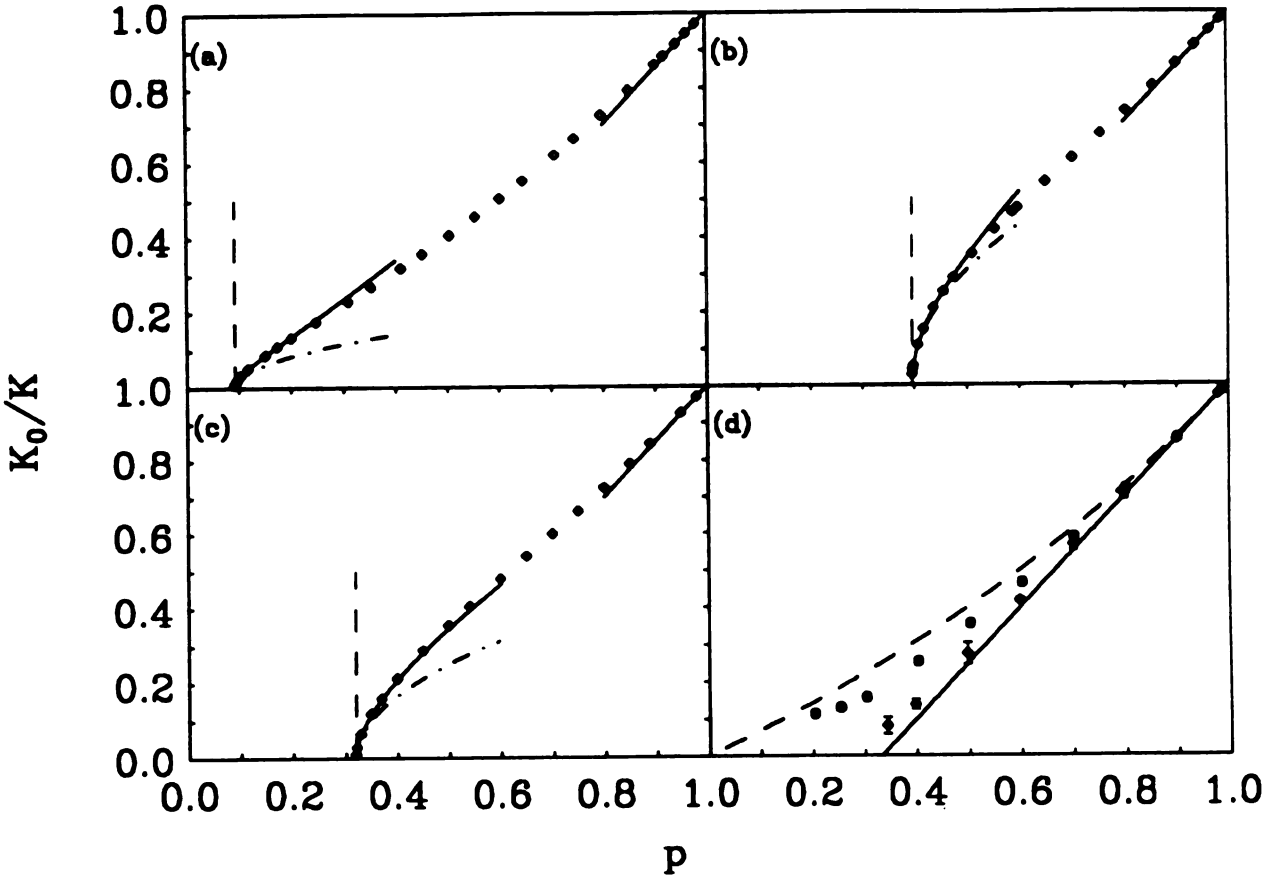

Figure 4.7: Showing the bulk modulus as a function of p for different arrangements of rigid fibers. (a) Triangular arrangement; (b) Hexagonal arrangement; (c) Kagomé arrangement; (d) Random arrangements, symbol $\diamond$ for overlapping case and $\bullet$ for nonoverlapping case.

4.7 CONCLUSIONS

In this chapter, we studied the elastic properties of rigid fiber-reinforced composites. The interface between fibers and matrix was assumed to be perfectly bonded. We studied three ordered structures in which rigid fibers are located on triangular, hexagonal and Kagomé superlattices, and two random structures which are overlapping and nonoverlapping rigid fibers randomly embedded in matrix. In the dilute limit, we obtained the elastic moduli and Poisson's ratio exactly. Around the rigidity threshold, we obtained these quantities approximately by calculating the energies dumped in the narrow necks between rigid fibers. We noted that all of the effective elastic moduli have the same scaling factor $-1/2$, that is, (elastic moduli) $\sim (p-p_c)^{-\frac{1}{2}}$ when $p \to p_c$.

We also developed Digital-Image-Based method to simulate such composites and obtained the effective elastic properties over the whole range of the area fraction of matrix. We showed that the fixed point in Poisson's ratio flow diagram does not exist in general for perfect bonding, which is quite different from the results obtained by self-consistent method and is also different from the behavior of porous composites. But the Kagomé arrangement of rigid fibers is an exception, in which we do find a fixed point in Poisson's ratio flow diagram, because of its special symmetry involved. We also predict that fixed points always exist if the boundary condition between fibers and matrix is pure sliding, which means that the portion of the matrix on fiber-matrix interface can move freely on the surface of fibers.

Bibliography

[1] E. B. Nauman, *et. al.* , Chem. Eng. Comm., **66**, 29 (1988).

[2] J. S. Furno and E. B. Nauman, J. Mater. Sci., **27** 1428 (1992).

[3] M. E. Boyce, A. S. Argon and D. M. Parks, Polymer, **28**, 1680 (1987).

[4] D. Hull, An Introduction to Composite Materials, Cambridge University Press (1981).

[5] J. Caruso and C. Chamis, Journal of Technology and Research, **8**, 77 (1986).

[6] M. F. Thorpe, lecture note, unpublished.

[7] I. Jasiuk, J. Chen and M. F. Thorpe, J. Mech. Phys. Solids, **40**, No. 2, 373 (1992)

[8] I. Jasiuk, unpublished.

[9] A. R. Day, K. A. Snyder, E. J. Garboczi and M. F. Thorpe, J. Mech. Phys. Solids, **40**, No. 5, 1031 (1992).

[10] J. Chen, M. F. Thorpe and A. R. Day, unpublished.

[11] W. H. Press, B. P. Flannery, S. A. Teukolsky and W. T. Vetterling, Numerical Recipes, p.301, Cambridge University Press, Cambridge, England (1986).

[12] K. A. Lurie and A. V. Cherkaev, J. Opt. Th. Appl., **42**, 305 (1984).

[13] A. Cherkaev, K. Lurie and G. W. Milton, Proc. Roy. Soc. A, **438**, 519 (1992).

[14] L. C. Davis, J. Chen and M. F. Thorpe, Proceedings of the American Society for Composites $7th$ Technical Conference on Composite Materials, Pennsylvania State University, October 13-15 (1992).

[15] M. P. Allen and D. J. Tildesley, Computer Simulation of Liquids, p.118, Oxford University Press, Oxford, England (1987).

Chapter 5

FINITE ELEMENT ANALYSIS

5.1 INTRODUCTION

In this chapter we are going to investigate the elastic properties of composites with ordered structures by using *finite element analysis.* For simplicity, we assume that the inclusions are perfectly rigid. In $2d$, this corresponds to *fiber-reinforced* composites and in $3d$ it is *particulate-reinforced.* In the last chapter, we have studied the elastic properties of such composites, but all of the boundary conditions there are assumed to be *perfect bonding.* This is a good approximation for most of the composites used today, such as graphite-epoxy composites. But it is still very interesting to ask what is the effect of the boundary conditions on the fiber-matrix interfaces in $2d$ or on the particle-matrix interfaces in $3d$. We studied these effects before theoretically by using *self-consistent method* and *differential scheme* [1]. But these effective medium methods just give accurate results in dilute regions. When the area or volume fraction of inclusions is large, the accuracy of these methods needs to be checked and they usually give wrong answers.

For fiber-reinforced or particulate-reinforced composites, the boundary condition on the inclusion-matrix interface has two extreme cases. One of them is *perfect bonding*, which we have studied in the last two chapters, and the other one is *pure*

sliding, which we are going to study here.

5.2 DILUTE RESULTS

In dilute limit, the effective elastic moduli can be obtained through the elastic strain energy. By assuming the **pure sliding boundary conditions**, the effective bulk modulus K, shear modulus μ, Young's modulus E and the Poisson's ratio ν for the composite are given by [1]

$$\frac{K_0}{K} = 1 - f\frac{2}{1+\nu_0}$$

$$\frac{\mu_0}{\mu} = 1 - f\frac{4}{5-\nu_0}$$

$$\frac{E_0}{E} = 1 - f\left[\frac{(1-\nu_0)}{(1+\nu_0)} + \frac{2(1+\nu_0)}{5-\nu_0}\right]$$

$$\nu = \nu_0 + f\frac{3(1-\nu_0)^2}{(5-\nu_0)} \tag{5.1}$$

in $2d$ for fiber-reinforced composites, and

$$\frac{K_0}{K} = 1 - f\frac{3(1-\nu_0)}{(1+\nu_0)}$$

$$\frac{\mu_0}{\mu} = 1 - f\frac{15(1-\nu_0)}{(17-19\nu_0)}$$

$$\frac{E_0}{E} = 1 - f\frac{3(1-\nu_0)}{(17-19\nu_0)}\left[5 + \frac{4(1-2\nu_0)^2}{(1+\nu_0)}\right]$$

$$\nu = \nu_0 + f\frac{12(1-\nu_0)(1-2\nu_0)^2}{(17-19\nu_0)} \tag{5.2}$$

in $3d$ for particulate-reinforced composites, where the subscript 0 denotes the corresponding quantities for the matrix. We note that the Poisson's ratio always increases when a small amount of rigid inclusions added into the matrix. This is different from the case with perfect bonding boundary condition. In that case, the Poisson's ratio increases if the Poisson's ratio of matrix is less than 1/3 and decreases otherwise. These dilute results provide a good check for the correctness of simulation results.

5.3 SIMULATION RESULTS

For rigid inclusions with pure sliding boundary condition, the *spring-grid scheme* we used before is very difficult to implement in simulation [2]. So we switch to ABAQUS, the commercial software package of finite element analysis.

To discretize the matrix, the four-node bilinear plane strain elements (CPE4) are used in $2d$ and the six-node linear displacement triangular prism (C3D6) elements are used in $3d$. Those elements are shown in Fig. 5.1. Since it is pure sliding on the interfaces between the rigid inclusions and the matrix, the nodes on the interfaces can move freely under the constraint that the distances between these nodes and the centers of inclusions are fixed. In $2d$, three ordered structures are studied, which are rigid inclusions located on a triangular superlattice, a hexagonal superlattice and a Kagomé superlattice. The meshes generated for these structures are illustrated in Fig. 5.2 - 5.5. Both Fig. 5.2 and Fig. 5.3 are the meshes for triangular arrangement of fibers, but for different choice of unit cell. Mesh 5.2 is the usual choice for this scheme, but it fails when the size of the inclusion goes beyond the territory of the unit cell. Mesh 5.3 seems odd, but it works when we approach the percolation threshold. The total number of elements in each of these meshes is around 1000, which is large enough to get decent results. We doubled the number of elements, but we found that the error due to this size effect is less than 0.5%.

In order to eliminate the surface effects, we use periodic boundary condition. An external strain e_{yy} is then imposed in the y direction and the effective Young's modulus E is obtained by calculating the elastic strain energy U per unit area.

$$E = \frac{2U}{e_{yy}^2} \tag{5.3}$$

The Poisson's ratio ν is obtained by calculating the change of the period of a unit cell in the direction perpendicular to the external loading. After that, the effective bulk modulus K and the effective shear modulus μ are found through

$$K = \frac{E}{2(1-\nu)} \tag{5.4}$$

$$\mu = \frac{E}{2(1+\nu)} \tag{5.5}$$

Similar method is used in $3d$ simulation in which FCC superlattice is studied. We must be careful in this case because FCC is an *anisotropic* system. An uniform strain $e_{xx} = 0.01$ along 100 direction is applied to the unit cell of FCC superlattice and we have the stress-strain relation

$$e_{xx} = S_{xxxx}\sigma_{xx}$$

$$e_{yy} = S_{yyxx}\sigma_{xx} \tag{5.6}$$

So the Poisson's ratio corresponding to this loading is given by

$$\nu = -\frac{S_{yyxx}}{S_{xxxx}} = -\frac{S_{12}}{S_{11}} \tag{5.7}$$

Since [3]

$$S_{11} = \frac{C_{11}+C_{12}}{(C_{11}-C_{12})(C_{11}+2C_{12})}$$

$$S_{12} = -\frac{C_{12}}{(C_{11}-C_{12})(C_{11}+2C_{12})} \tag{5.8}$$

we get

$$\nu = \frac{C_{12}}{C_{11}+C_{12}} = 1 + \frac{C_{11}}{C_{12}}^{-1} \tag{5.9}$$

For FCC central-force spring network [4], we know

$$C_{11} = 2C_{12} \tag{5.10}$$

This is a good approximation when we approach the percolation threshold. Combining Eqn. (5.9) and (5.10), we find that a fixed point $\nu_c = 1/3$ exists in the Poisson's ratio flow diagram. Using Eqs. (5.8), (5.9) and noticing that $E = 1/S_{11}$, we get the bulk modulus K

$$K = \frac{C_{11}+2C_{12}}{3} = \frac{E}{3(1-2\nu)} \tag{5.11}$$

This relation is exactly the same as that for a $3d$ isotropic system.

In Fig. 5.6, we plot the relation between the Poisson's ratio ν and the area or the volume fraction of the matrix p for different ν_0, the Poisson's ratio of matrix. In Fig. 5.7, we plot the effective bulk modulus of the composite for $\nu_0 = 1/3$ for $2d$ ordered structures and $\nu_0 = 0.30$ for FCC superlattice. The solid lines in all of these figures are the dilute results which are obtained from Eqs. (5.1) and (5.2). It is obvious that our simulation results agree very well with the theoretical predictions in the dilute regions. In $2d$, since the it is pure sliding on the inclusion-matrix interfaces, the coefficient $\mathbf{B}$, which we derived from last chapter, is always equal to zero, which means that a fixed point always exists for these order structures. Simply by letting $\mathbf{B} = 0$ in Eqs. (3.18), (3.33) and using Eqn. (3.45), we obtain the fixed points in Poisson's ratio flow diagrams for triangular, hexagonal, Kagomé arrangements, which are $p_c = 1/3$, $p_c = 1$, $p_c = 1/3$, respectively. In Fig. 5.6, we find that the Poisson's ratios do flow to the fixed points which are marked by the $\star$ symbols, unless there exists a dramatic change in the Poisson's ratios when p approaches to the percolation threshold p_c. In Fig. 5.7, our results are compared with the one with perfect bonding boundary conditions which are obtained by using the spring-grid scheme [5] in $2d$ and by using FEA in $3d$ [6]. They should be the same because the details of the boundary conditions on the inclusion-matrix interfaces are irrelevant under the hydrostatic pressure. This agreement is easy to see from Fig. 5.7. One color figure (Fig. 5.8) is shown to display the distribution of the yy component of the stress tensor for hexagonal arrangement of fibers. In order to check the correctness of our simulation, we plot the stress component σ_{rr} and $\sigma_{r\phi}$ for triangular superlattice in Fig. 5.9. Since it is pure sliding on the fiber-matrix interfaces, the stress component $\sigma_{r\phi}$ should be zero on the interfaces. Because the external strain $e_{yy} > 0$ is acted on the unit cell, the symmetry should be kept with respect to the y-axis, and σ_{rr} should be maximum (positive) at $\phi = \frac{1}{2}\pi, \frac{3}{2}\pi$ and should be minimum (negative) at $\phi = 0, \pi$. It is clearly shown in Fig. 5.9 that the simulation data agree very well with the above arguments within the computational errors.

5.4 CONCLUSIONS

In this chapter, we calculate the effective elastic moduli and obtain the Poisson's ratio flow diagram for fiber-reinforced and particular-reinforced composites. The inclusions are perfectly rigid and the inclusion-matrix interfaces are pure sliding. Three ordered structures in $2d$ (triangular, hexagonal, Kagomé) and one ordered structure in $3d$ (FCC) are studied by using finite element method with the aid of ABAQUS and PATRAN. In $2d$ we find that a fixed point always exists in the Poisson's ratio flow diagram. This statement is quite general because under the pure sliding boundary condition, all of the effective elastic moduli are scaled to only one elastic constant, C_{11} of the matrix, when we approach the percolation threshold. Since the Poisson's ratio of a composite is basically the effective bulk modulus divided by the effective shear modulus, it should be a constant (independent of the Poisson's ratio of the matrix) at the percolation threshold. The composites with randomly distributed fibers or particles, with pure sliding boundary condition on the inclusion-matrix interfaces, is another interesting field to investigate, but it is beyond the current the computational ability of finite element packages.

(a)

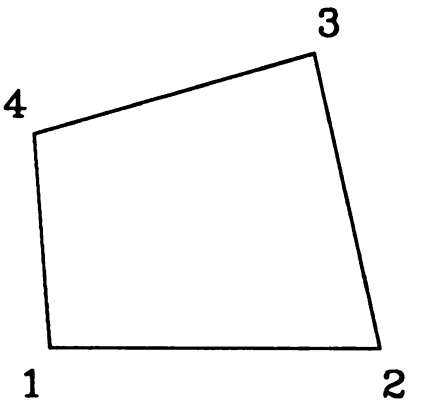

(b)

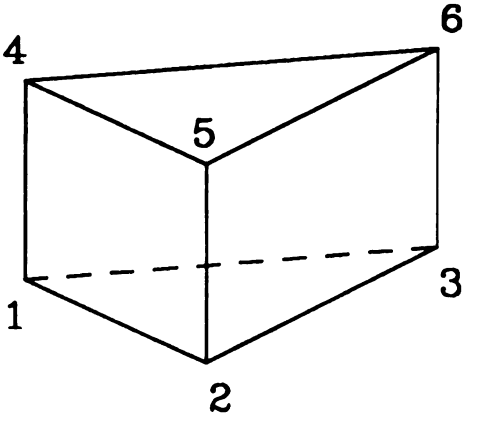

Figure 5.1: Showing the type of basic elements for $2d$ and $3d$ used in simulation. (a) 4 node, bilinear plane strain element CPE4; (b) 6 node, linear displacement triangular prism C3D6.

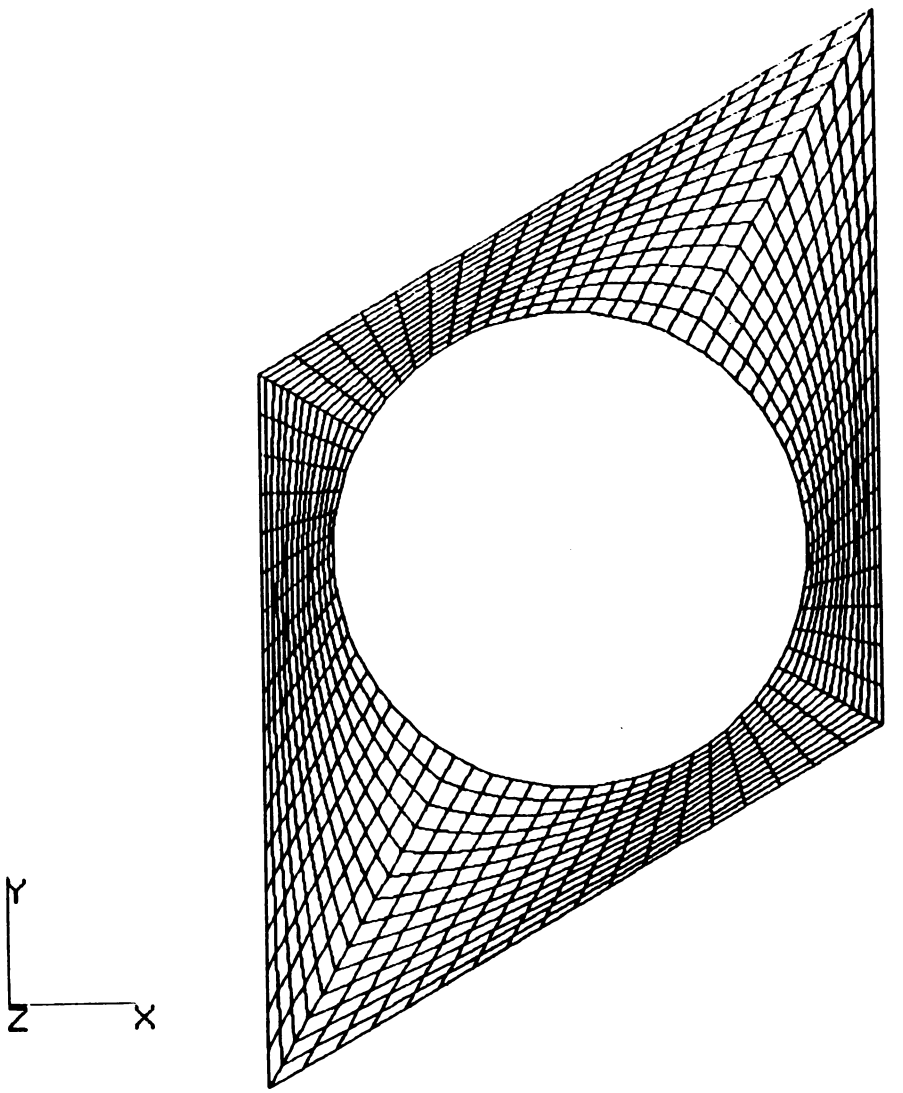

Figure 5.2: Showing the mesh of a unit cell for triangular arrangement of fibers. Version 1.

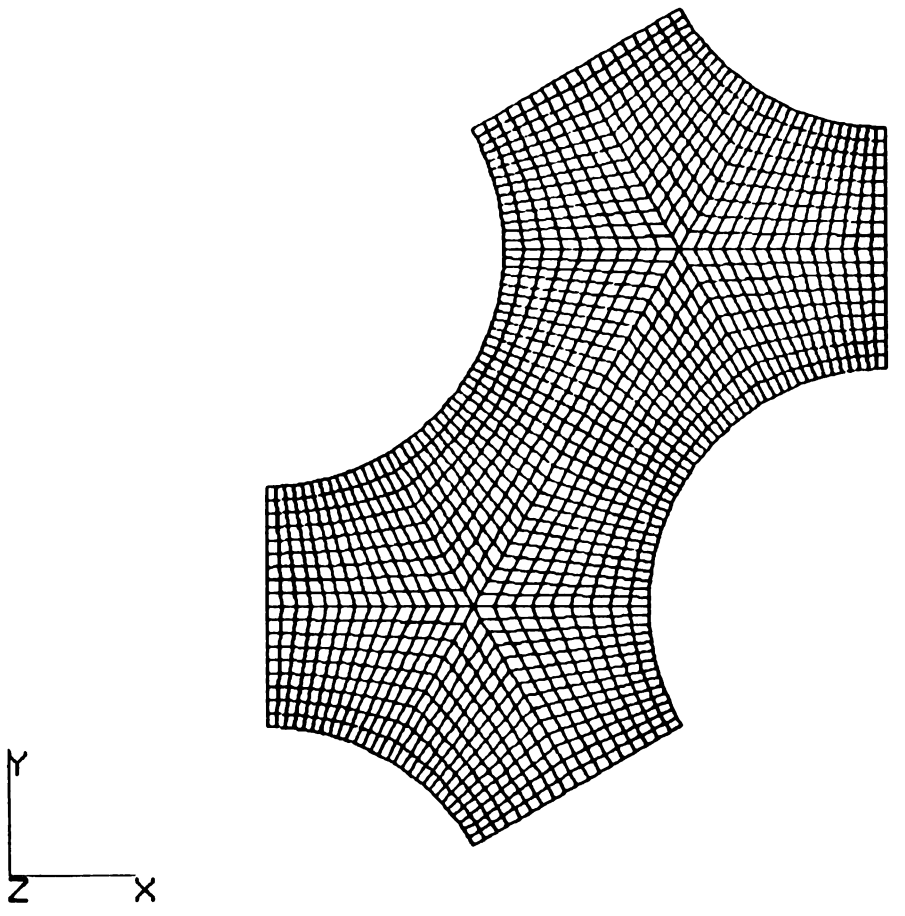

Figure 5.3: Showing the mesh of a unit cell for triangular arrangement of fibers. Version 2.

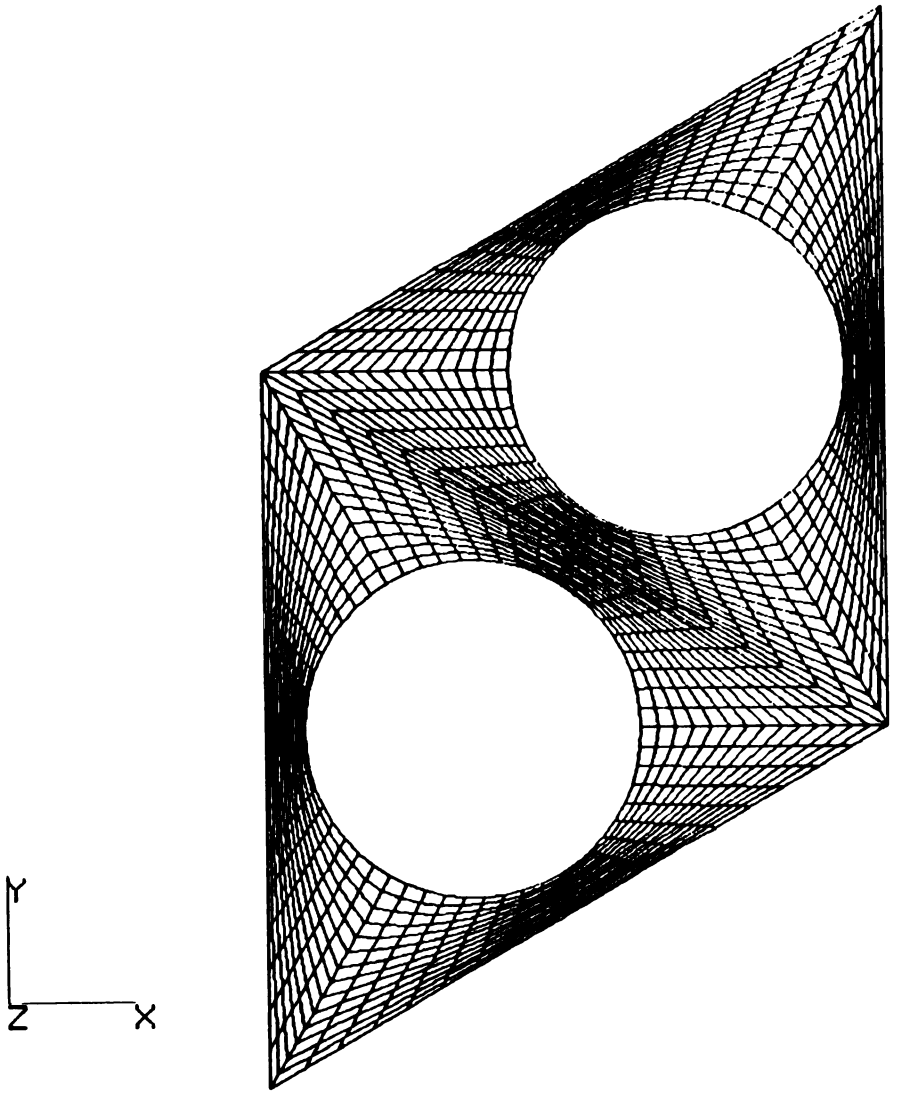

Figure 5.4: Showing the mesh of a unit cell for hexagonal arrangement of fibers.

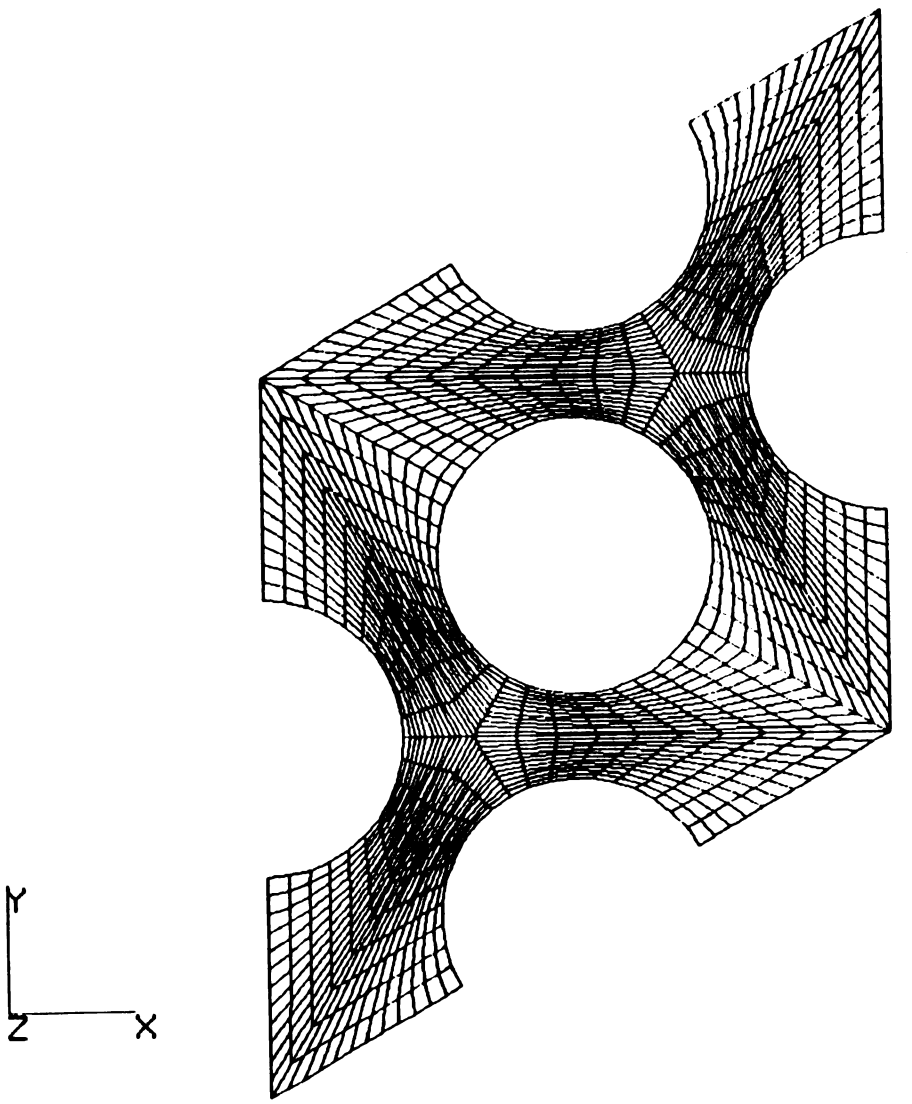

Figure 5.5: Showing the mesh of a unit cell for Kagomé arrangement of fibers.

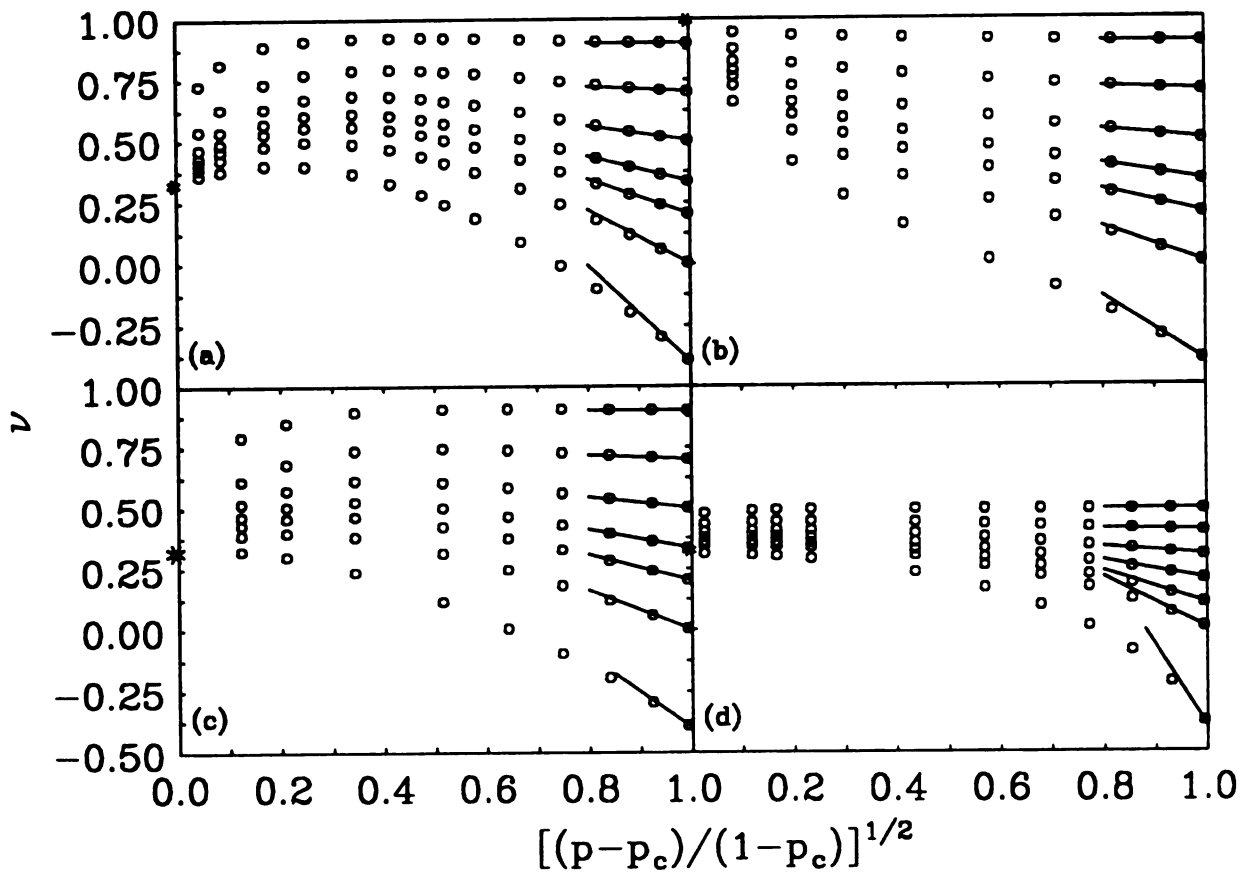

Figure 5.6: Showing the Poisson's ratio flow diagram for composites with rigid inclusions under pure sliding boundary condition. The solid lines are dilute results from Eqn. (5.1). (a) triangular superlattice; (b) hexagonal superlattice; (c) Kagomé superlattice; (d) FCC superlattice.

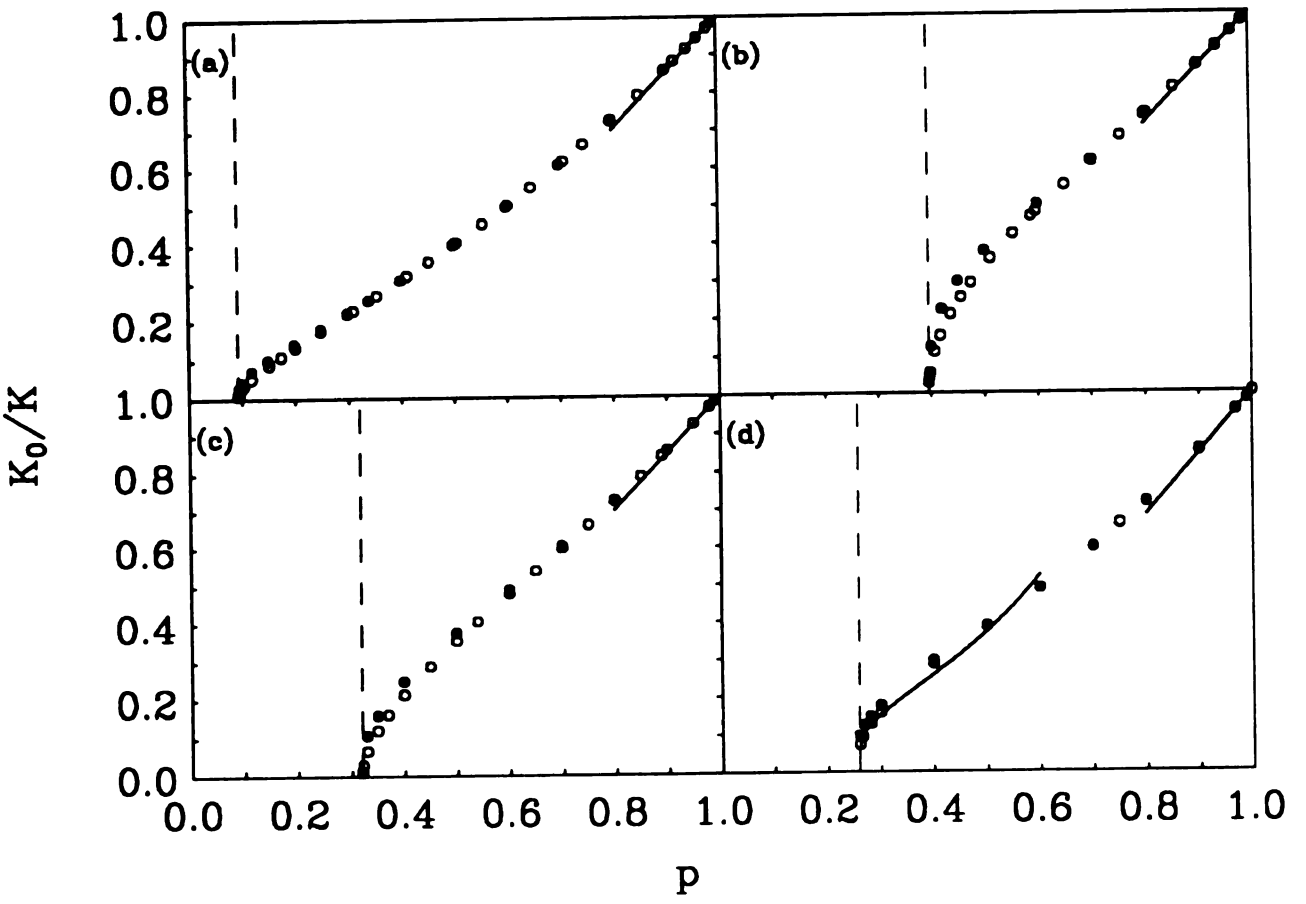

Figure 5.7: Showing the effective bulk modulus for composites with rigid inclusions under pure sliding boundary condition (solid dots). The simulation results under the perfect bonding boundary condition are also included for comparison (open circles). The solid lines are dilute results from Eqn. (5.1). In (a), (b) and (c), the Poisson's ratio of matrix $\nu_0 = 1/3$. In (d), $\nu_0 = 0.30$. (a) triangular superlattice; (b) hexagonal superlattice; (c) Kagomé superlattice; (d) FCC superlattice.

Figure 5.8: Showing the distribution pattern of the yy component of the stress tensor for composite with rigid inclusions, with pure sliding boundary condition, located on hexagonal superlattice. An external strain $e_{yy} = 0.01$ is imposed on this unit cell. The Poisson's ratio of the matrix is $\nu_0 = 0.50$ and the area fraction of the matrix is $p = 0.60$.

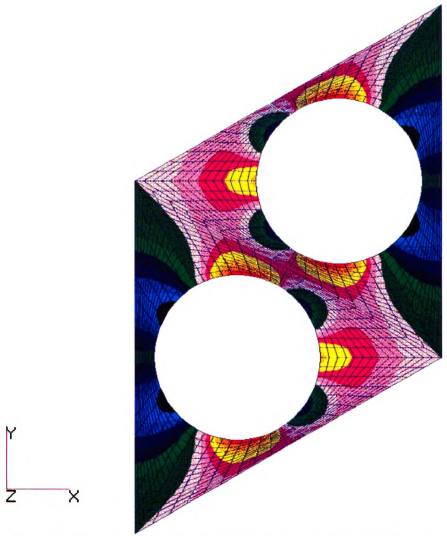

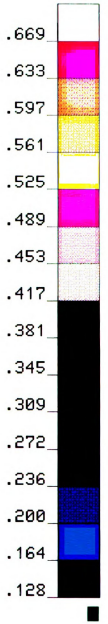

STRESS YY, 2D, PURE SLIDING, HEXAGONAL, EYY=0.01, P=0.60, NU0=0.5
ABAQUS V4-9-1 27-AUG-92 09:07:27 1512 1713
PROCEDURE 2 TIME STEP 1 INCREMENT 1

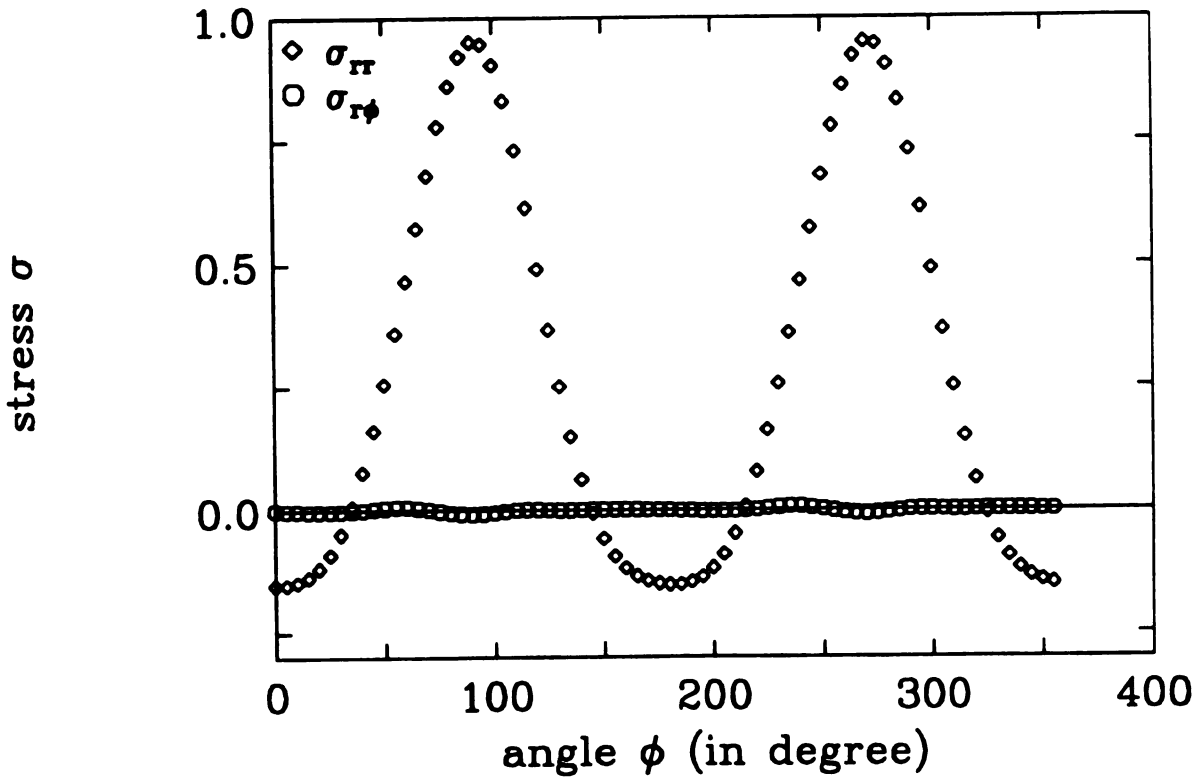

Figure 5.9: Showing the stress component σ_{rr} and $\sigma_{r\phi}$ on the fiber-matrix interface for triangular superlattice arrangement of fibers. An external strain $e_{yy} = 0.01$ is imposed on this unit cell, and $p = 0.6$, $\nu_0 = 0.50$.

Bibliography

[1] I. Jasiuk, J. Chen and M. F. Thorpe, J. Mech. Phys. Solids, **40**, No. 2, 373 (1992).

[2] J. Chen, M. F. Thorpe and A. R. Day, unpublished.

[3] C. Kittle, Introduction to Solid State Physics, John Wiley & Sons, Inc., New York (1957).

[4] S. Feng and M. F. Thorpe, Phys. Rev. B, **31**, 276 (1985).

[5] J. Chen, M. F. Thorpe and L. C. Davis, unpublished.

[6] L. C. Davis, J. Chen and M. F. Thorpe, Proceedings of the American Society for Composites $7th$ Technical Conference on Composite Materials, Pennsylvania State University, October 13-15 (1992).

Chapter 6

LOCAL STRAIN IN RANDOM COMPOSITES

6.1 INTRODUCTION

The study of the local strains in random composites with rigid inclusions is very important because it not only provides a scheme for breakdown modes but also predicts the effective elastic moduli of composites. In this chapter I am going to examine the elastic response of random, rigid inclusions in an elastic, continuum matrix in the high concentration limit. A surprising result has been found for hydrostatic deformation. In this work, we minimize the total elastic energy subject to the constraint that the average dilatation is the macroscopically imposed value. A consequence is that the local strain between any two nearest neighbor inclusions is a simple and well defined function of only the gap between them, independent of orientation and location. This prediction has been verified statistically by simulations on random, uniform rigid disks in $2D$, and we believe that this prediction is still true in $3D$. Such local behavior is not expected and, indeed, is not observed for uniaxial strains or in the related case of the electric conductivity of sheets with random holes [1] [2]. Such local behavior is completely opposite to the breakdown of electrical or mechanical

systems where extreme statistics dominate [3].

6.2 THEORY

In this section, we present the derivation of the local strain for a highly concentrated $2D$ and $3D$ composite consisting of an elastic matrix with uniform, perfectly rigid circular (for $2D$) or spherical (for $3D$) inclusions. These formulae apply to any macroscopically isotropic array of disks, either ordered or disordered.

Let us consider two neighboring disks with the same radius R and a distance between centers r_i, as shown in Fig. 6.1. Thus, the gap between the disks is $w_i = r_i - 2R$. Let the macroscopic strain in a hydrostatic deformation be $\epsilon_{xx} = \epsilon_{yy} = \epsilon$. The relative area dilation is $\Delta A/A = 2\epsilon$ to the leading order. We assume that the local deformation is a dilatation in which the change in r_i is along the line from center to center and is given by

$$\delta r_i = \epsilon_i r_i. \tag{6.1}$$

The ϵ_i are to be determined variationally by minimizing the elastic energy of the system subject to the following constraint:

$$\frac{1}{N}\sum_{i=1}^{N} \epsilon_i = \epsilon, \tag{6.2}$$

where the sum is over all N nearest neighbor pairs which can be determined by a Voronoi construction for a disordered system. Typically there will be 5, 6 or 7 nearest neighbors for each disk at high concentration limit, as shown in Table 6.1.

The elastic energy associated with each gap is given to the leading order in $\sqrt{R/w_i}$ by [4] [5]

$$U(i)_{gap} = \frac{\pi}{2} C_{11}^0 \epsilon_i^2 r_i^2 \sqrt{\frac{R}{w_i}}. \tag{6.3}$$

where C_{11}^0 is the elastic constant of the matrix in $2D$ with plane strain conditions, and perfect bonding at the interface between the matrix and the disk is assumed.

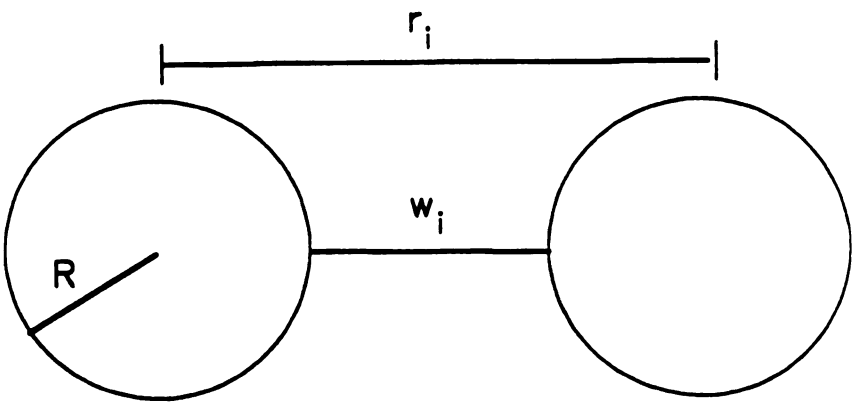

Figure 6.1: Neck region between two rigid disks. The width of the gap on the line joining the centers is w_i and the center-to-center distance is r_i.

Table 6.1: Occurrence of nearest neighbors for a configuration with 240 disks. For example, 62 of 240 disks have 5 nearest neighbors.

Number of nearest neighbors	Number of disks
4	0
5	62
6	128
7	38
8	12
9	0

The result of minimizing the total energy, which is just the sum of the $U(i)_{gap}$ over all pairs, subject to the constrain given by Eqn. 6.2 is:

$$\epsilon_i = \frac{B\epsilon}{r_i^2}\sqrt{\frac{w_i}{R}}, \tag{6.4}$$

where the constant B is given by

$$B = \left(\frac{1}{N}\sum_{i=1}^{N} r_i^{-2}\sqrt{\frac{w_i}{R}}\right)^{-1}. \tag{6.5}$$

Eqs. (6.4) and (6.5) represent the central result of this chapter. In the following section, we show that simulations verify this approximation statistically. This is, the mean value of the strain ϵ_i for a given gap w_i averaged over several realizations is given by Eqs. 6.4 and 6.5.

The same procedure can be used for $3D$. In this case, the total elastic energy is given by

$$U = \sum_{i=1}^{N} \frac{\pi}{2} C_{11}^0 \epsilon_i^2 r_i^2 R \ln\left(\frac{R}{w_i}\right). \tag{6.6}$$

where N is the total number of pairs of nearest neighbor. Minimizing U under the constrain of Eqs. 6.2, we have

$$\epsilon_i = \frac{B\epsilon}{r_i^2 \ln\left(\frac{R}{w_i}\right)}, \tag{6.7}$$

where

$$B = \left\{ \frac{1}{N} \sum_{i=1}^{N} \left[r_i^2 \ln\left(\frac{R}{w_i}\right) \right]^{-1} \right\}^{-1}. \tag{6.8}$$

Here the relative change in volume is $\Delta V/V = 3\epsilon$. We have no simulations to confirm these Eqs. (6.7) and (6.8) yet, so the results for $3D$ remain as predictions.

Returning to $2D$, we can calculate the area bulk modulus k using the expressions for the energy in each gap, Eqn. (6.3), and the strain, Eqs. (6.4) and (6.5). After summing over all gaps in the sample and setting the energy per unit area equal to $1/2k(\Delta A/A)^2$, we find the area bulk modulus to be

$$k = \frac{\phi C_{11}^0 B}{8R^2} \frac{2N}{M}, \tag{6.9}$$

where ϕ is the area fraction of disks and M is the number of disks in the sample, and the average number of nearest neighbors per disk is given by $2N/M$. The elastic constant C_{11}^0 is related to the area modulus of the matrix by

$$C_{11}^0 = \frac{2k_0}{1+\nu_0}, \tag{6.10}$$

where ν_0 is the matrix Poisson's ratio in $2D$ plane strain.

6.3 SIMULATIONS

The digital-image-based method or spring-grid scheme (see **chapter 2** for details) used in the simulations has been described previously [4] [6]. Essentially, it is a convenient technique to represent the matrix with embedded rigid disks. The disks are placed randomly on the sheet but without overlapping. A shaking algorithm is used to generate the random configurations [7]. A small hydrostatic strain of 10^{-3} is

imposed on the sample using periodic boundary conditions. The sample (supercell) was a 210×210 triangular lattice with disks of diameter 11 units.

In this section, the results for an average over 49 configurations with 240 disks are presented. The area fraction of rigid fibers is $\phi = 1 - p = 0.6029$. This area fraction was chosen for illustration since the algorithm for generating the positions of the disks gives truly random array at $\phi = 0.6029$, yet the system is concentrated. For $\phi \geq 0.7$, the arrays tend to crystallize into a triangular lattice and develop long range order. This does not invalidate the approximation, but it may be a less stringent test since the approximation becomes exact for an ordered array. In Fig. 6.2, the average value of ϵ_i as a function of w_i is plotted (open circles). The function Eq. (6.4), with B determined by Eq. (6.5), is also shown as the solid curve. The functional form provides an excellent fit when the gap is small, and it is about 10% larger compared with least-square-fit when the gap is as large as the radius of the disk. This small discrepancy may be caused by including too many nearest neighbors at large w_i in the sum appearing in Eq. (6.5). The simulations further support our assumption of a purely tensile local deformation; the calculated shear energies in the neck regions are two orders of magnitude smaller than the tensile energies.

The definition of a nearest neighbor in a random composite is somewhat arbitrary. Here we used a Voronoi construction [7] such as that displayed in Fig. 6.3. Around each disk, we draw a cell that contains all the points closest to the disk center. Each section of the perimeter of the cell defines one nearest neighbor. It is apparent that some nearest neighbors are rather distant, particularly if the number exceeds six. For one configuration, the occurrence of nearest neighbors is summarized in Table I.

The width of the distribution of values of ϵ_i for a given w_i is measured by the root mean square (RMS) deviation from the mean, which is plotted as the solid circles in Fig. 2. The RMS is only about 30% of the mean value of ϵ_i for the entire range of w_i. The narrowness of this distribution confirms the main approximation of the previous section.

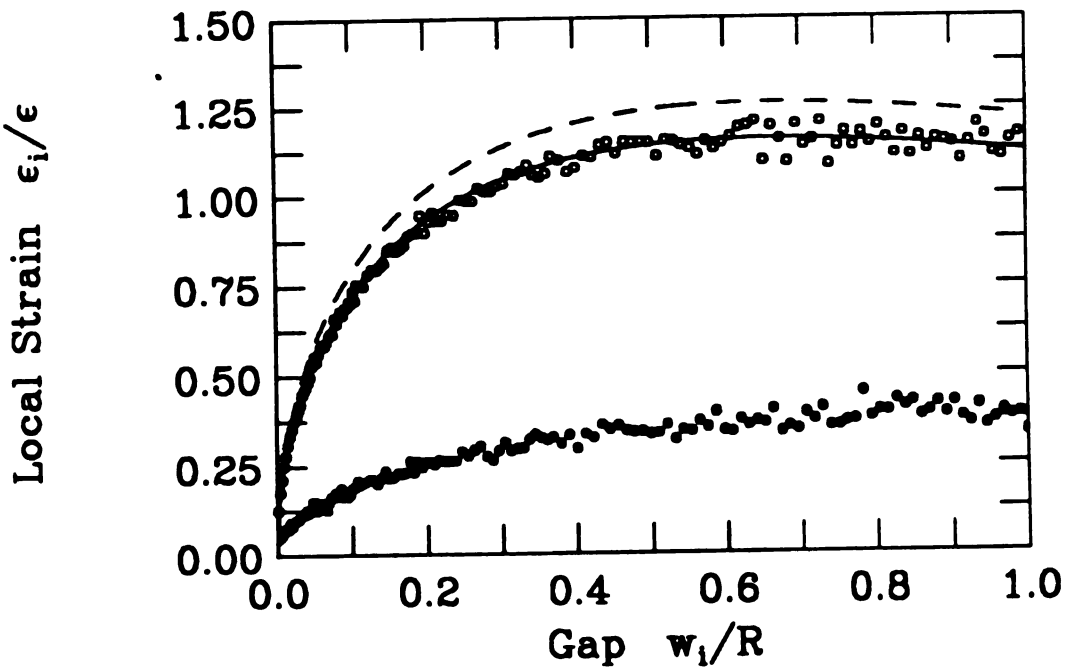

Figure 6.2: Local strain $\epsilon_i = \delta r_i/r_i$ vs gap width w_i for random rigid disks with area fraction $\phi = 0.6029$. The open circles are the results from simulation. The solid circles are the root mean square (RMS) deviation from the mean. The dashed line is the analytical result given by Eq. (6.4), and the solid line is the least-square-fit of the simulation data.

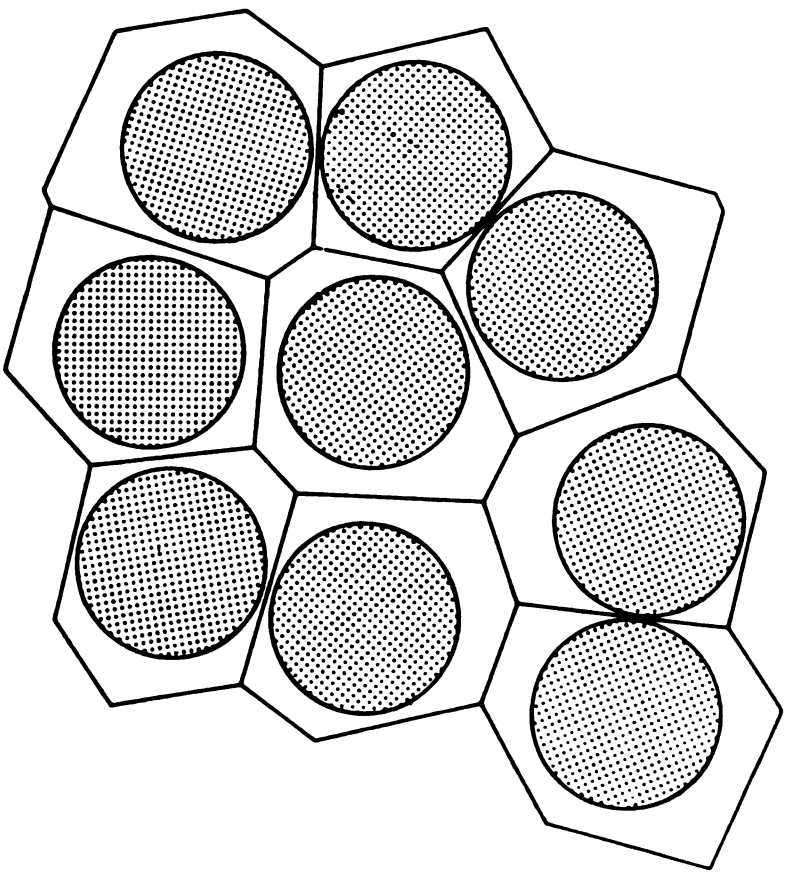

Figure 6.3: A typical Voronoi construction for a random array of disks. The Voronoi cell contains all points closer to the center of disk than any other.

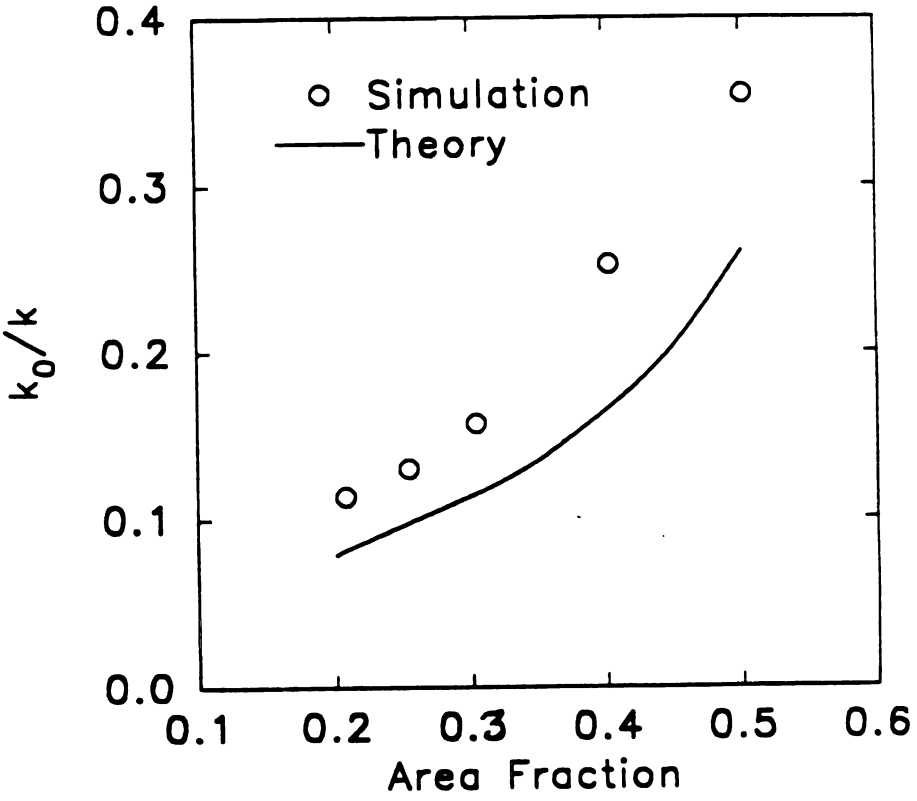

Figure 6.4: Reciprocal of the area modulus k relative to the matrix modulus k_0 vs area fraction of matrix. Open circles are from simulations and the solid line is a theory correct to first order in $\sqrt{(R/w)}$ [see Eq. (6.9)].

Although $p = 1 - 0.6029 = 0.3971$ is considered concentrated, by any reasonable definition of p_c for random close packing [8], this matrix area fraction is not in the asymptotic regime where critical exponents are observed. The best estimate of p_c nonoverlapping disks is $p_c = 0.18 \pm 0.02$. For $p \leq 0.3$, the present shaking algorithm does not give truly random arrays. However, the plot of ϵ_i vs w_i at $p = 0.3$ fits the theory [Eqs. (6.4) and (6.5) even better than in Fig. 6.2 (At $p = 0.3$ the result from theory is about 8.5% larger than the least-square-fit of the simulation results.)

The reciprocal of the area modulus k normalized to the matrix modulus k_0 is shown in Fig. 6.4 as a function of matrix area function. The matrix $2D$ Poisson's ratio is $\nu_0 = 1/3$. The open circles are from the simulation and the solid curve is from Eq. (6.9) with B calculated from Eq. (6.5). The calculated value of k_0/k is smaller than the simulation value, but this is not surprising. In the case of the triangular lattice [4], the leading term in k_0/k, which is of order $\sqrt{(R/w)}$, is also an underestimate and terms of order (R/w) are required to obtain good agreement for $p - p_c \leq 0.3$. We have not included higher order terms in Eq. (6.9) or Fig. 6.4.

6.4 CONCLUSIONS

The principal conclusion of this work is that the local strain, as represented by $\epsilon_i = \delta r_i/r_i$, can be approximated by a simple function of the gap w_i, but not the surrounding environment, in a concentrated random array of rigid inclusions in an elastic matrix under hydrostatic deformation. This conclusion has been verified by simulations on rigid disks in $2D$, but should also apply to rigid spheres in $3D$. A first order theory of the area or bulk modulus has been derived and compares reasonably well with simulations. Higher order corrections would be required for a really good fit.

Our findings appear to be the first example of local geometry dominating the strain near close packing. This notion does not work for uniaxial stress, nor does

an analogous approach work for high contrast conductivity problems. This localized situation is the opposite of the extreme statistics observed in breakdown.

Our work is also of interest in the more general context of calculating properties of real composites. Most finite element calculations, especially in $3D$, are limited to ordered arrays of inclusions. Real materials are seldom well approximated by ordered (periodic) arrays of inclusions. Thus it is useful to have some new insights into random composites.

Bibliography

[1] B. I. Halperin, S. Feng and P. N. Sen, Phys. Rev. Lett., **54**, 22, 2391 (1985).

[2] C. J. Lobb and M. G. Forrester, Phys. Rev. B, **35**, 4, 1999 (1987).

[3] P. M. Duxbury, P. L. Leath and P. D. Beale, Phys. Rev. B, **36**, 1, 367 (1987).

[4] J. Chen, M. F. Thorpe and L. C. Davis, unpublished.

[5] L. C. Davis, J. Chen and M. F. Thorpe, Proceedings of the American Society for Composites - Seventh Technical Conference, p.339, Thechnomic, Lancaster, PA (1992).

[6] A. R. Day, K. A. Snyder, E. J. Garboczi and M. F. Thorpe, J. Mech. Phys. Solid, **40**, 5, 1031 (1992).

[7] M. P. Allen and D. J. Tildesley, Computer Simulation of Liquids, p.118, Oxford, UK (1987).

[8] J. P. Berryman, Phys. Rev. A, **27**, 2, 1053 (1983).

Chapter 7

BOUNDS FOR FIBER ALIGNED COMPOSITES

7.1 INTRODUCTION

Fiber reinforced materials are composites which contain two materials - *parallel cylindrical fibers* are embedded in another material called the *matrix*. If the fibers are very long compared with their diameters, we can neglect the end effect of the fibers and treat the composite as a two-dimensional system, in so far as the transverse properties are concerned.

One of the most important properties of fiber aligned composites is the effective transverse elastic moduli. Usually the composite is assumed to be statistically homogeneous and statistically transversely isotropic over length scales large compared to both the diameter of the fibers and the spacing between the fibers. Furthermore the fibers are assumed to be perfectly bonded to the matrix. Since the 1960's much analytic work has been done to calculate the *bounds* for the various elastic moduli of composites [1]-[15]. In principle, the effective properties of composites can be obtained from the corresponding properties of the individual constituents, but because of the complexity of this problem, few exact results for the effective elastic moduli

are available, although one can obtain tighter and tighter bounds on those quantities. In this paper we use computer simulations to obtain *numerically exact* results for the elastic moduli of fiber aligned glass - epoxy composites. We compare our simulation results with second and third order bounds for the area bulk modulus and transverse shear modulus.

7.2 BOUNDS FOR THE TRANSVERSE ELASTIC MODULI

All of the bounds for the elastic moduli can be determined mathematically by calculating the n-point matrix probability functions $S_n(\mathbf{r_1}, \mathbf{r_2}, ..., \mathbf{r_n})$, which is the probability of simultaneously finding n points in the matrix phase [10]. Most of the work done to date has focused on calculating S_n to higher and higher orders to give tighter bounds [2] [9] [10] [11]. An nth order bound on some effective elastic modulus X_e of a composite means that the bound is exact up to $(X_1 - X_2)^n$, where 1 and 2 label the matrix and fiber respectively [14].

Hill [7] derived the second order bounds for the area bulk modulus, Young's modulus and the area Poisson's ratio of a transversely isotropic aligned fiber composite. Later Hashin [2] obtained upper and lower bounds to the same order for the area bulk modulus and transverse shear modulus by using a different method. These second order bounds are functions of the area fraction of the two individual phases but are *independent* of the geometry of the fibers.

Let k_1, k_2, G_1 and G_2 be the plane-strain bulk moduli and shear moduli of the two phases, where 1 and 2 label the matrix and fiber respectively, and define k_e, G_e as the corresponding effective moduli of the composite. Up to second order, k_e and G_e are bounded by

$$k_L^{(2)} \leq k_e \leq k_U^{(2)},$$

$$G_L^{(2)} \leq G_e \leq G_U^{(2)}. \tag{7.1}$$

where $k_L^{(2)}$, $k_U^{(2)}$ are the second order lower and upper bounds for the effective area bulk modulus, and $G_L^{(2)}$, $G_U^{(2)}$ are similar bounds for the effective transverse shear modulus. Assuming that $k_2 > k_1$ and $G_2 > G_1$, the second order bounds are given by [2],

$$k_L^{(2)} = k_1 + \frac{f_2}{\frac{1}{k_2-k_1} + \frac{f_1}{k_1+G_1}},$$

$$k_U^{(2)} = k_2 + \frac{f_1}{\frac{1}{k_1-k_2} + \frac{f_2}{k_2+G_2}},$$

$$G_L^{(2)} = G_1 + \frac{f_2}{\frac{1}{G_2-G_1} + \frac{f_1(k_1+2G_1)}{2G_1(k_1+G_1)}},$$

$$G_U^{(2)} = G_2 + \frac{f_1}{\frac{1}{G_1-G_2} + \frac{f_2(k_2+2G_2)}{2G_2(k_2+G_2)}}, \tag{7.2}$$

where f_1 and $f_2 = 1 - f_1$ are the area fraction of the matrix and fiber respectively.

The third order bounds are obtained by calculating S_1, S_2 and S_3. From these three distribution functions, one can obtain the two important microstructural parameters ζ and η, which relate directly to the the third order bounds. Then ζ and η are expressed as the triple integrals [10],

$$\zeta_1 = \frac{4}{\pi f_1 f_2} \int_0^\infty \frac{dz}{z} \int_0^\infty \frac{dy}{y} \int_0^\pi d\theta \left[S_3(y,z,\theta) - \frac{S_2(y)S_2(z)}{S_1} \right] \cos 2\theta,$$

$$\eta_1 = \frac{16}{\pi f_1 f_2} \int_0^\infty \frac{dz}{z} \int_0^\infty \frac{dy}{y} \int_0^\pi d\theta \left[S_3(y,z,\theta) - \frac{S_2(y)S_2(z)}{S_1} \right] \cos 4\theta. \tag{7.3}$$

where S_1 is simply f_1, and the triangle formed by $\mathbf{r_1}$, $\mathbf{r_2}$ and $\mathbf{r_3}$ is parameterized by two edges of length y and z and the angle θ between them. After evaluating ζ and η, the third order bounds for the effective area bulk modulus and transverse shear modulus are obtained through [9]

$$k_L^{(3)} \leq k_e \leq k_U^{(3)},$$

and

$$G_L^{(3)} \leq G_e \leq G_U^{(3)}. \tag{7.4}$$

where

$$k_L^{(3)} = \left[\langle 1/k\rangle - \frac{f_1 f_2 (1/k_2 - 1/k_1)^2}{\langle 1/\tilde{k}\rangle + \langle 1/G\rangle_\zeta}\right]^{-1},$$

$$k_U^{(3)} = \left[\langle k\rangle - \frac{f_1 f_2 (k_2 - k_1)^2}{\langle \tilde{k}\rangle + \langle G\rangle_\zeta}\right],$$

$$G_L^{(3)} = \left[\langle 1/G\rangle - \frac{f_1 f_2 (1/G_2 - 1/G_1)^2}{\langle 1/\tilde{G}\rangle + \Xi}\right]^{-1},$$

$$G_U^{(3)} = \left[\langle G\rangle - \frac{f_1 f_2 (G_2 - G_1)^2}{\langle \tilde{G}\rangle + \Theta}\right], \tag{7.5}$$

and

$$\Xi = 2\langle 1/k\rangle_\zeta + \langle 1/G\rangle_\eta,$$

$$\Theta = \left[2\langle k\rangle_\zeta \langle G\rangle^2 + \langle k\rangle^2 \langle G\rangle_\eta\right] / \langle k + 2G\rangle^2. \tag{7.6}$$

The notations used in the above equations are defined as follows,

$$\langle b\rangle = b_1 f_1 + b_2 f_2,$$

$$\langle \tilde{b} \rangle = b_1 f_2 + b_2 f_1,$$

$$\langle b \rangle_\zeta = b_1 \zeta_1 + b_2 \zeta_2,$$

$$\langle b \rangle_\eta = b_1 \eta_1 + b_2 \eta_2. \tag{7.7}$$

where $\zeta_2 = 1 - \zeta_1$ and $\eta_2 = 1 - \eta_1$.

Miller and Torquato [11] calculate the microstructural parameters ζ and η for identical *nonoverlapping* fibers distributed randomly throughout the matrix. In this case, ζ and η can be expressed as

$$\zeta_2 = \frac{f_2}{3} + O(f_2^2), \tag{7.8}$$

and

$$\eta_2 = \frac{56}{81} f_2 + O(f_2^2). \tag{7.9}$$

Actually Torquato and Lado [12] calculate ζ_2 and η_2 through $O(f_2^2)$, but they find that the linear term dominates.

The ζ_1 and η_1 for *overlapping* fibers, randomly embedded in a matrix, are also obtained by Torquato and Beasley [10]. They obtain these two microstructural parameters by numerically evaluating the triple integrals in Eqs. (7.3) and the results are listed in Table 7.1.

7.3 EFFECTIVE MEDIUM THEORY

Hill [13] calculated the effective area bulk modulus k_e and transverse shear modulus G_e of the fiber reinforced composite by using effective medium theory. The transverse

Table 7.1: The microstructural parameter ζ and η, for identical overlapping fibers randomly distributed in a matrix, as a function of f_2. This table is obtained from Ref. [10].

f_2	ζ_1	η_1
0.00	1.0	1.0
0.10	0.93855	0.91591
0.20	0.87673	0.83273
0.30	0.81443	0.75045
0.40	0.75149	0.66916
0.50	0.68772	0.58896
0.60	0.62277	0.50998
0.70	0.55602	0.43232
0.80	0.48621	0.35595
0.90	0.40969	0.27996
0.95	0.36455	0.24012
0.99	0.31291	0.19928

shear modulus G_e is found by solving the following cubic equation and taking the positive root.

$$\frac{f_1 k_1}{k_1 + G_e} + \frac{f_2 k_2}{k_2 + G_e} = 2\left(\frac{f_1 G_2}{G_2 - G_e} + \frac{f_2 G_1}{G_1 - G_e}\right), \tag{7.10}$$

and k_e is obtained through

$$k_e = \left(\frac{f_1}{k_1 + G_e} + \frac{f_2}{k_2 + G_e}\right)^{-1} - G_e. \tag{7.11}$$

When $f_2 \to 0$, we have $k_e = k_L^{(3)} = k_U^{(3)}$ and $G_e = G_L^{(3)} = G_U^{(3)}$ up to the linear term in f_2, which is true for both overlapping and nonoverlapping cases.

7.4 STRAIN AND STRESS TENSOR FOR A TRIANGULAR NETWORK

In our calculation of the effective elastic moduli, we obtain the displacements of every node in the lattice. This information can be used to generate the components of the local local stress and strain tensors using the following method.

Consider a single triangle with vertices A, B and C which have coordinates $A = (0,0)$, $B = (\frac{1}{2}, \frac{\sqrt{3}}{2})$ and $C = (1,0)$ in the unstrained lattice and let the spring constants of the bonds AB, BC and AC be α, β and γ respectively. When the network is relaxed, the *strains* along the bonds AB, BC and AC are ϵ_1, ϵ_2 and ϵ_3, respectively. If

$$\epsilon = \begin{pmatrix} \epsilon_{xx} & \epsilon_{xy} \\ \epsilon_{yx} & \epsilon_{yy} \end{pmatrix}, \tag{7.12}$$

is the strain tensor at the center of the triangle ABC then the ϵ_i are given by $\epsilon_i = \hat{r}_i \cdot \epsilon \cdot \hat{r}_i$ where the $\hat{r}_i$ are unit vectors along the bonds. For the triangle ABC this gives us the following set of equations.

$$\epsilon_1 = \left(\frac{1}{2}, \frac{\sqrt{3}}{2}\right) \begin{pmatrix} \epsilon_{xx} & \epsilon_{xy} \\ \epsilon_{yx} & \epsilon_{yy} \end{pmatrix} \begin{pmatrix} \frac{1}{2} \\ \frac{\sqrt{3}}{2} \end{pmatrix},$$

$$\epsilon_2 = \left(\frac{1}{2}, -\frac{\sqrt{3}}{2}\right) \begin{pmatrix} \epsilon_{xx} & \epsilon_{xy} \\ \epsilon_{yx} & \epsilon_{yy} \end{pmatrix} \begin{pmatrix} \frac{1}{2} \\ -\frac{\sqrt{3}}{2} \end{pmatrix},$$

$$\epsilon_3 = (1,0) \begin{pmatrix} \epsilon_{xx} & \epsilon_{xy} \\ \epsilon_{yx} & \epsilon_{yy} \end{pmatrix} \begin{pmatrix} 1 \\ 0 \end{pmatrix}. \tag{7.13}$$

By symmetry $\epsilon_{xy} = \epsilon_{yx}$ and thus Eq. (7.13) forms a set of three equations in three unknowns which can be solved to give the components of the strain tensor,

$$\epsilon_{xx} = \epsilon_3,$$

$$\epsilon_{yy} = \frac{2}{3}\left(\epsilon_1 + \epsilon_2 - \frac{1}{2}\epsilon_3\right),$$

$$\epsilon_{xy} = \epsilon_{yx} = \frac{1}{\sqrt{3}}(\epsilon_1 - \epsilon_2). \tag{7.14}$$

This procedure is analogous to the use of a strain gauge to find the components of the strain tensor experimentally [16].

The components of the *stress* tensor are found by considering the normal forces acting on each edge of the triangle. Because the bonds all have unit length, the normal force is equal to the normal stress. If

$$\sigma = \begin{pmatrix} \sigma_{xx} & \sigma_{xy} \\ \sigma_{yx} & \sigma_{yy} \end{pmatrix}, \tag{7.15}$$

is the stress tensor at the center of the triangle ABC, the normal forces are given by $\vec{f} \cdot \hat{n} = \hat{n} \cdot \sigma \cdot \hat{n}$ where $\hat{n}$ is the unit normal vector. For the triangle ABC this gives us the following set of equations.

$$\frac{\sqrt{3}}{2}(\alpha\epsilon_1 + \gamma\epsilon_3) = \left(\frac{\sqrt{3}}{2}, \frac{1}{2}\right) \begin{pmatrix} \sigma_{xx} & \sigma_{xy} \\ \sigma_{yx} & \sigma_{yy} \end{pmatrix} \begin{pmatrix} \frac{\sqrt{3}}{2} \\ \frac{1}{2} \end{pmatrix},$$

$$\frac{\sqrt{3}}{2}(\gamma\epsilon_3 + \beta\epsilon_2) = \left(-\frac{\sqrt{3}}{2}, \frac{1}{2}\right) \begin{pmatrix} \sigma_{xx} & \sigma_{xy} \\ \sigma_{yx} & \sigma_{yy} \end{pmatrix} \begin{pmatrix} -\frac{\sqrt{3}}{2} \\ \frac{1}{2} \end{pmatrix},$$

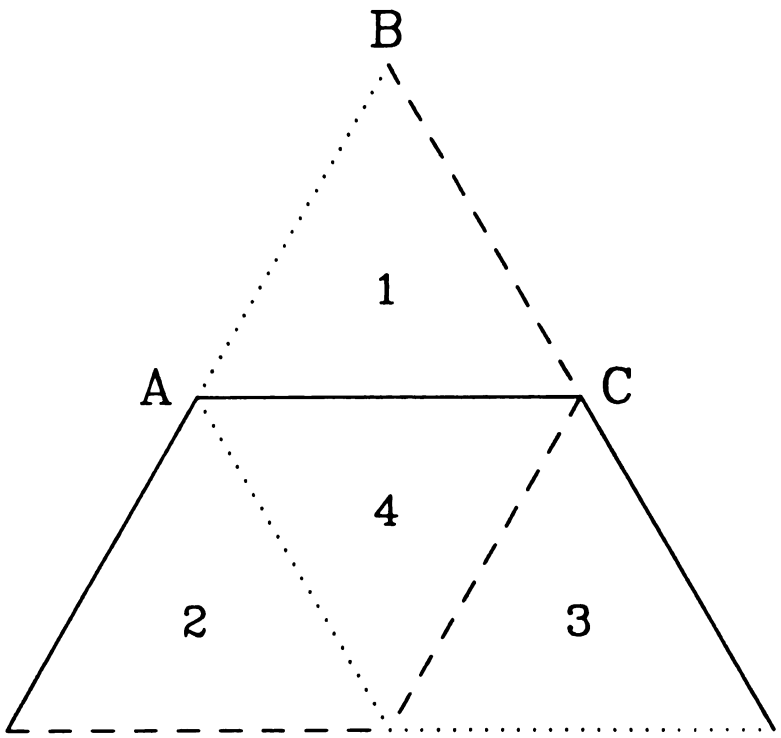

Figure 7.1: Showing the local grid configuration used to calculate the components of the strain and stress tensors. The three outer triangles are labelled 1, 2 and 3 and the inner triangle is 4. The bonds have strengths α, β and γ as indicated by the dots, dashes and solid lines respectively following the notation of Fig. 2.1.

$$\frac{\sqrt{3}}{2}(\beta\epsilon_2 + \alpha\epsilon_1) = (0,-1)\begin{pmatrix} \sigma_{xx} & \sigma_{xy} \\ \sigma_{yx} & \sigma_{yy} \end{pmatrix}\begin{pmatrix} 0 \\ -1 \end{pmatrix}. \tag{7.16}$$

By symmetry $\sigma_{xy} = \sigma_{yx}$ and thus Eq. (7.16) forms a set of three equations in three unknowns which can be solved to give the components of the stress tensor,

$$\sigma_{xx} = \frac{1}{\sqrt{3}}\left(2\gamma\epsilon_3 + \frac{1}{2}\alpha\epsilon_1 + \frac{1}{2}\beta\epsilon_2\right),$$

$$\sigma_{yy} = \frac{\sqrt{3}}{2}(\alpha\epsilon_1 + \beta\epsilon_2),$$

$$\sigma_{xy} = \sigma_{yx} = \frac{1}{2}(\alpha\epsilon_1 - \beta\epsilon_2). \tag{7.17}$$

If α, β and γ are *not* equal it is necessary to average over all three possible orientations of the springs. The scheme we choose is to average the stress tensor σ and the strain tensor ϵ over the three triangles labeled 1, 2 and 3 in Fig. 7.1 and assign the average values to triangle 4. This procedure was used to produce the stress and strain maps shown in Figs. 7.3 - 7.5.

There are many different prescriptions for assigning the local stress and strain fields and some simple consistency checks are necessary. Obviously the method should produce the correct stress and strain fields for a one-component homogeneous material and the stress should be related to the strain by the known elastic tensor. It is easily shown that our method satisfies both these tests. In the composite material we checked that the *average* stress $\langle\sigma\rangle$ and the *average* strain $\langle\epsilon\rangle$ had the correct values and were related by the effective elastic moduli calculated from the energy as described in Section III. We found that $\langle\epsilon_{xx}\rangle$ was equal to the applied strain to within 0.0062%, 0.024% and 0.25% for fiber fractions of 1%, 20% and 55%, and $\langle\sigma_{xx}\rangle/\langle\epsilon_{xx}\rangle$ was equal to the effective Young's modulus evaluated from the energy to within 0.0095%, 0.54% and 2.4% for fiber fractions of 1%, 20% and 55%. Since the lattice is free to relax in the y direction, we should have $|\langle\sigma_{yy}\rangle| = 0$ when the system is fully relaxed. From our simulation, we found that $|\langle\sigma_{yy}\rangle| < 10^{-6}$. The local stress can also be evaluated from the local strain using the local elasticity tensor. We

produced stress maps calculated by both methods and found that they were almost identical except near the fiber matrix interface where our averaging procedure is not exact. When the stress is calculated by this method we found that $\langle\sigma_{xx}\rangle/\langle\epsilon_{xx}\rangle$ gave errors of 0.028%, 0.56% and 3.6% in for fiber fractions of 1%, 20% and 55% in the effective Young's modulus. This error increases with the amount of interface and is always larger than that calculated from Eq. (7.17), so this is not the best way to proceed. Rather, it is best to calculate both the stress and the strain *directly* from the extension of the springs and the forces in the springs, using (7.14) and (7.17).

7.5 RESULTS FOR GLASS - EPOXY FIBER COMPOSITE

We use digital-image-based method (see **Chapter 2** for details) to perform simulations on glass - epoxy fiber aligned composites. In this system, glass fibers are embedded in an epoxy matrix to form a transversely isotropic composites. Several kinds of glass and epoxy are available now [17] and most of them are isotropic. We select one typical glass and one typical epoxy which have the Young's moduli and Poisson's ratios shown in Table 7.2. Under the assumption of plane strain, the two-dimensional Young's modulus and Poisson's ratio are obtained using standard relations [18]

$$E = \frac{E'}{1-\nu'^2},$$

and

$$\nu = \frac{\nu'}{1-\nu'}. \tag{7.18}$$

where E, ν are the Young's modulus and Poisson's ratio in two dimensions, and E', ν' are the corresponding three-dimensional quantities. Using the 3D quantities for glass and fiber, which are listed in Table 7.2, and substituting them into Eqs. (7.18), we obtain the 2D Young's modulus and Poisson's ratio (Table 7.2). Using Eqs. (2.3),

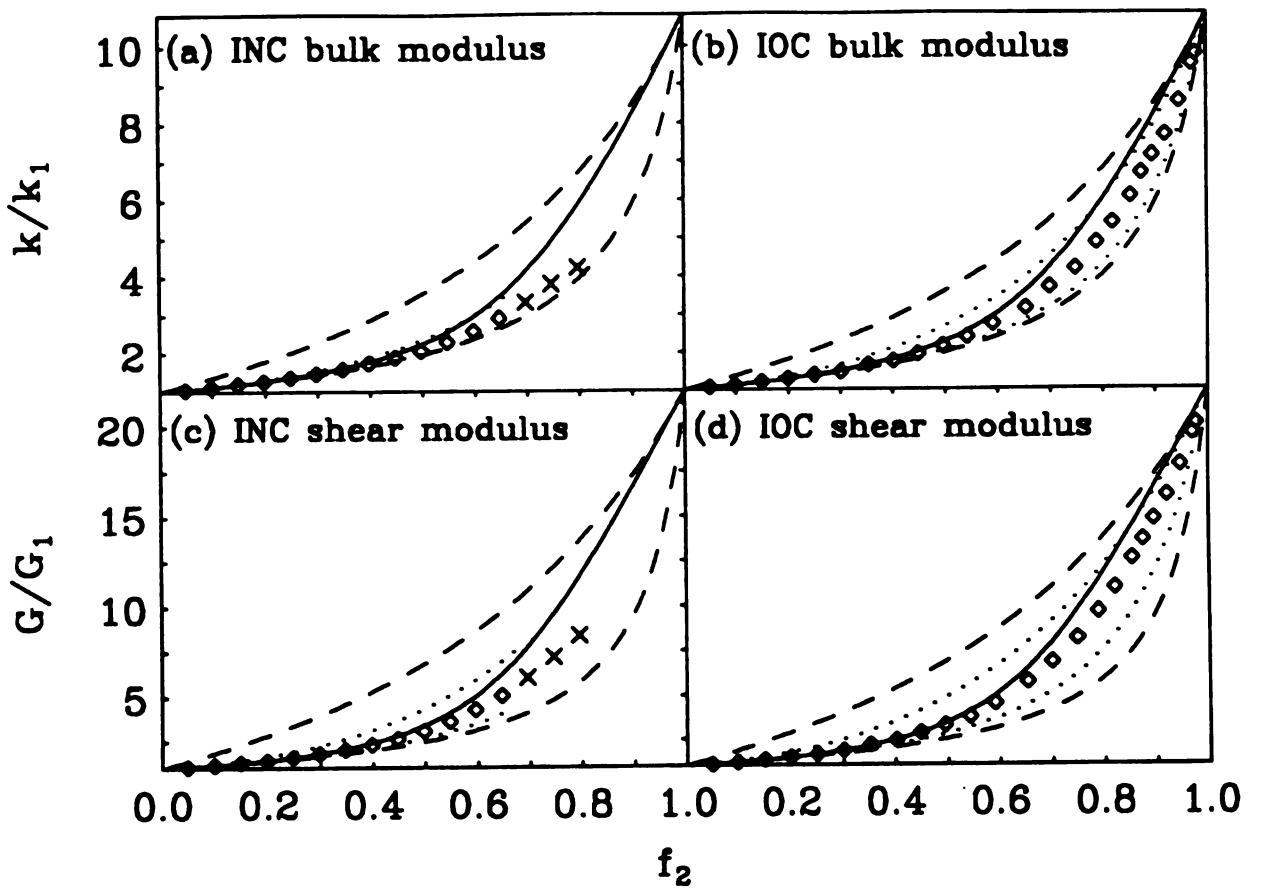

Figure 7.2: Showing the effective area bulk modulus and effective transverse shear modulus. The symbols are simulation data, averaged on 6 configurations. In INC model, the cross symbols at $f_2 > 0.7$ means crystallization of the fibers occurs, and so we stop the third order bounds at $f_2 = 0.7$ [10]; Dash - Hill-Hashin second order bounds; Dots - Milton-Torquato third order bounds; Solid line: effective medium theory. (a) Area bulk modulus in INC model; (b) Area bulk modulus in IOC model; (c) Transverse shear modulus in INC model; (d) Transverse shear modulus in IOC model.

Table 7.2: The Young's modulus and Poisson's ratio for glass and epoxy in 3D and 2D.

	Glass		*Epoxy*	
	$E(GPa)$	ν	$E(GPa)$	ν
$3D$	57.2	0.301	2.80	0.402
$2D$	62.9	0.430	3.34	0.672

Table 7.3: The spring constants α, β, γ for glass and epoxy.

	Glass	*Epoxy*
α	60.0	1.00
β	30.9	4.63
γ	100.2	12.0

we choose a set of springs α, β and γ (Table 7.3) to input our simulation and obtain the area bulk modulus and transverse shear modulus for the Identical Overlapping Cylinders (IOC) model and for the Identical Non-overlapping Cylinders (INC) model shown in Fig. 7.2. It is clear from these figures that all of the simulation data are indeed bounded by the second order [2] and third order bounds [11] as required. When the area fraction of fibers is small ($f_2 < 0.5$), the simulation data are very close to the *lower* bound. Therefore, the lower bounds yield relatively accurate estimates of the effective moduli [11].

Both the area bulk modulus and transverse shear modulus are found to be a little bit larger in the IOC model than that in the INC model. This is as expected because in IOC model the fibers are more tightly combined together which gives slightly higher elastic moduli. For the glass - epoxy composites used this paper, the

ratio of the Young's moduli is about 20 : 1 (Table 7.2). The larger the ratio is, the stronger the effect becomes. This has been verified by the model in which *rigid* fibers are embedded in a matrix [19].

It has been noted by Davis [20] that averaging the upper and lower third order bounds provides a better description of the effective moduli than effective medium theory. The work of Davis was focused on three dimensional metal-matrix composites. We have also found this observation to be true in the two-dimensional composites studied here. This can be ascertained by doing the averaging by eye in Fig. 7.2. Also note that for the IOC model the effective medium theory falls outside the third order bounds when the area fraction of fibers is large ($f_2 > 0.8$).

Strain and stress maps for the INC model are shown in Fig. 7.3-7.5, which are obtained by using Eqs. (7.14) and (7.17). A plane strain of magnitude 10^{-3} is applied along the x direction, and the distribution of the xx components of the strain and stress tensors are represented by different colors. Since the glass fibers have a much larger elastic moduli than the epoxy matrix (Table 7.2), the strain inside the fibers is very small. Therefore, the xx component of strain has a big jump at the fiber-epoxy interfaces. However, the stress map is much smoother than the strain map, because the forces at the fiber-epoxy interfaces are balanced when the system is in equilibrium. Furthermore, the stress is concentrated in the narrow strips (along the x direction) connecting the fibers (see Fig. 7.5). Therefore, when the applied strain is large enough, cracks may be propagated in these narrow strips first. In Figs. 7.3-7.5 the *graininess* is due to the finite size of the pixels used and is a indication of the resolution that we have achieved. White circles are drawn at the fiber-matrix interface for emphasis. This is unnecessary for the strain but is required for the stress maps where the locations of the fibers is difficult to obtain due to the continuity of traction at the interface.

Figure 7.3: A plane strain of 10^{-3} in the x direction is applied to this glass - epoxy composite and the relative scale of strain (upper panel) and stress (lower panel) is represented by different colors as indicated for a fiber fraction $f_2 = 0.01$. In arbitrary units, the mean strain is 45 (corresponding to a mean or applied strain of 10^{-3}) and the mean stress is 45 as indicated in the scales to the right.

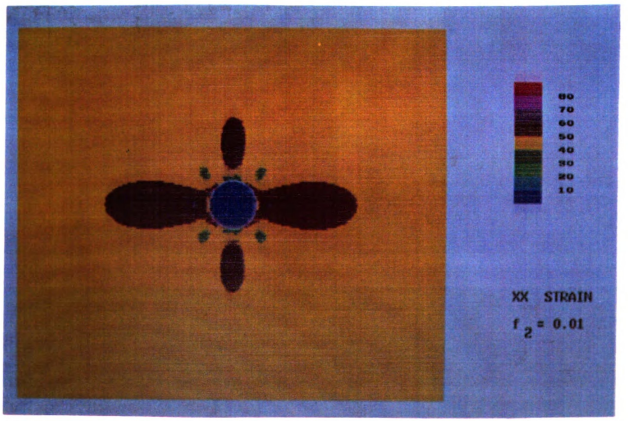
80
70
60
50
40
30
20
10
XX STRAIN
f 2 = 0.01

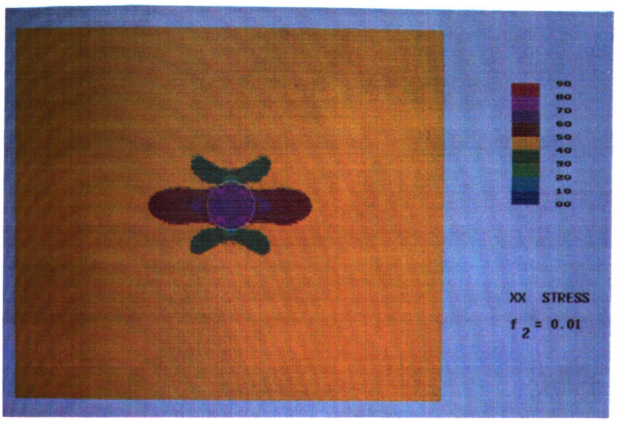
90
80
70
60
50
40
30
20
10
00
XX STRESS
f 2 = 0.01

Figure 7.4: A plane strain of 10^{-3} in the x direction is applied to this glass - epoxy composite and the relative scale of strain (upper panel) and stress (lower panel) is represented by different colors as indicated for a fiber fraction $f_2 = 0.20$. In arbitrary units, the mean strain is 45 (corresponding to a mean or applied strain of 10^{-3}) and the mean stress is 45 as indicated in the scales to the right.

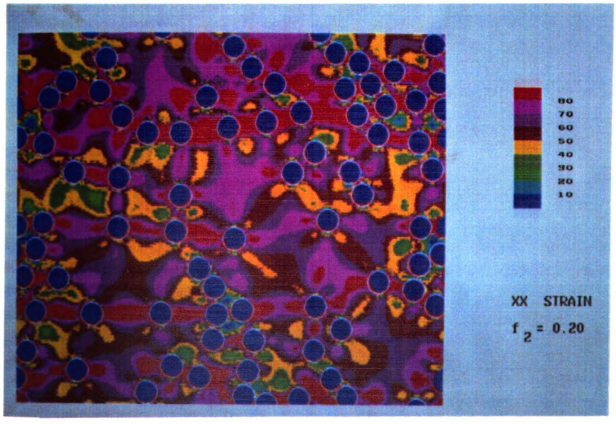
80
70
60
50
40
30
20
10
XX STRAIN
f_2 = 0.20

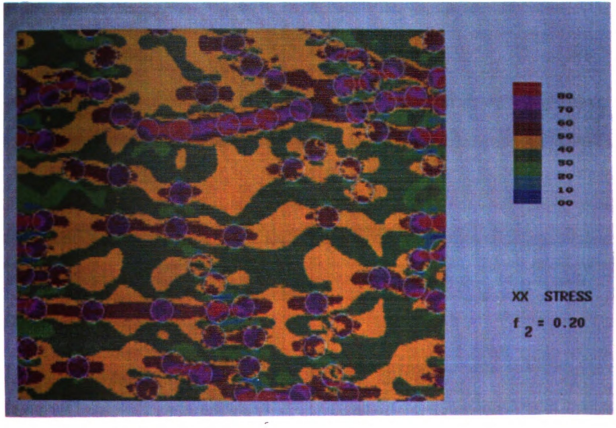
80
70
60
50
40
30
20
10
00
XX STRESS
f_2 = 0.20

Figure 7.5: A plane strain of 10^{-3} in the x direction is applied to this glass - epoxy composite and the relative scale of strain (upper panel) and stress (lower panel) is represented by different colors as indicated for a fiber fraction $f_2 = 0.55$. In arbitrary units, the mean strain is 45 (corresponding to a mean or applied strain of 10^{-3}) and the mean stress is 45 as indicated in the scales to the right.

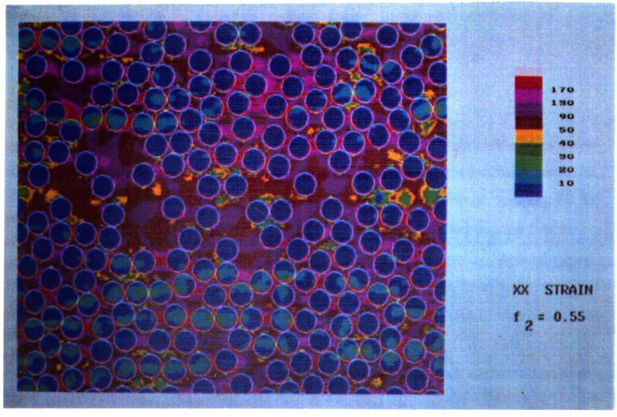
170
130
90
50
40
30
20
10
XX STRAIN
f 2 = 0.55

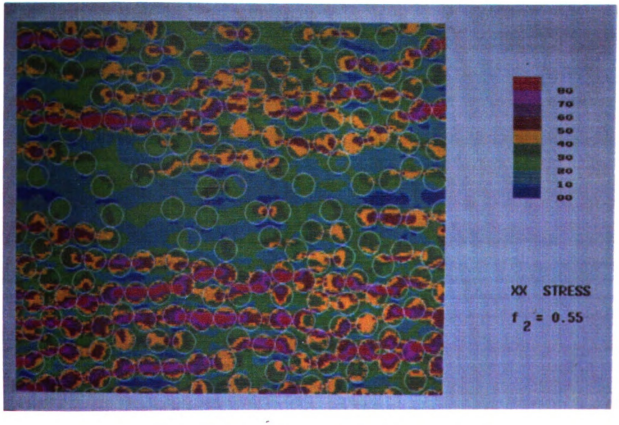
80
70
60
50
40
30
20
10
00
XX STRESS
f 2 = 0.55

7.6 CONCLUSIONS

In this chapter, a digital-image-based model is used to calculate the the effective area bulk modulus and transverse shear modulus for fiber aligned composites. The method is quite general and can be applied to any fiber reinforced composites. In this paper we use glass - epoxy composites as an illustration and discuss two cases: identical *nonoverlapping* fibers and the unphysical case of *overlapping* fibers which are embedded in the epoxy. We compute the effective area bulk modulus and transverse shear modulus of these composites which lie within the Hill-Hashin second order bounds [2] [7] and the Milton-Torquato third order bounds [9] [11]. This simulation method is quite general and can be applied to other cases, such as when the fibers are of different types, shapes or sizes.

Bibliography

[1] Z. Hashin and B. W. Rosen, J. Appl. Mech., Trans. ASME, **31**, 223 (1964).

[2] Z. Hashin, J. Mech. Phys. Solids, **13**, 119 (1965).

[3] Z. Hashin, J. Appl. Mech., **46**, 543 (1979).

[4] Z. Hashin, J. Appl. Mech., **50**, 481 (1983).

[5] J. R. Willis, J. Mech. Phys. Solids, **25**, 185 (1977).

[6] R. Hill, J. Mech. Phys. Solids, **11**, 357 (1963).

[7] R. Hill, J. Mech. Phys. Solids, **12**, 199 (1964).

[8] G. W. Milton, J. Appl. Phys., **52**, 5294 (1981).

[9] G. W. Milton, J. Mech. Phys. Solids, **30**, 177 (1982).

[10] S. Torquato and J. D. Beasley, Int. J. Eng. Sci., **24**, 435 (1986).

[11] C. A. Miller and S. Torquato, J. Appl. Phys., **69**, 1948 (1991).

[12] S. Torquato and F. Lado, J. Appl. Mech., **59**, 1 (1992).

[13] R. Hill, J. Mech. Phys. Solids, **13**, 189 (1965).

[14] C. G. Joslin and G. Stell, J. Appl. Phys., **60**, 1607 (1986).

[15] N. Silnutzer, Ph.D. thesis, University of Pennsylvania, Philadelphia, PA (1972).

[16] S. Timoshenko and J. N. Goodier, Theory of Elasticity, p.20, McGraw-Hill Inc., New York (1951).

[17] P. M. Mallick, Fiber-Reinforced Composite – Materials, Manufacturing and Design, Marcel Dekker, Inc., New York and Basel (1988).

[18] M. F. Thorpe and I. Jasiuk, Proc. Roy. Soc. A, **438**, 531 (1992).

[19] J. Chen, M. F. Thorpe and L. C. Davis, unpublished.

[20] L. C. Davis, Metallurgical Transactions, **22A**, 3065 (1991).

Chapter 8

MATERIALS WITH POLYGONAL HOLES

8.1 INTRODUCTION

We discuss some new exact results in two dimensional (plane) elasticity that have applications in studies of the elastic response of two dimensional composite materials. These results are related to a recently proven theorem [1] which reduces a parameter space of the local stress fields and the effective elastic properties. This theorem is most powerful for materials containing holes. Recently, we have shown that the effective elastic modulus of a sheet containing circular holes is independent of the Poisson's ratio of the matrix [2] [3]. Now we consider a material with polygonal holes and also show that the effective elastic modulus depends on the shape of holes but not on the Poisson's ratio of the matrix. In addition, we discuss the results available in literature for the elastic response of materials containing circular and elliptical holes, and planar cracks which relate directly to the subject of this chapter.

8.2 TWO-DIMENSIONAL ELASTICITY

The stress-strain equations for a linear elastic and isotropic material in three dimensions ($3d$) are given by

$$\epsilon_{ij} = \frac{1}{E'}[(1+\nu')\sigma_{ij} - \nu'\sigma_{kk}\delta_{ij}] \qquad \text{i,j,k} = 1,2,3 \tag{8.1}$$

where E' is the $3d$ Young's modulus and ν' is the $3d$ Poisson's ratio. We use the primes for the elastic constants in three-dimensions ($3d$) so that we may use unprimed quantities in two-dimensions ($2d$).

In $2d$ elasticity the constitutive equations have a form similar to (8.1), but only involve two coordinates

$$\epsilon_{ij} = \frac{1}{E}[(1+\nu)\sigma_{ij} - \nu\sigma_{kk}\delta_{ij}] \qquad \text{i,j,k} = 1,2 \tag{8.2}$$

The unprimed quantities E and ν are the area Young's modulus and the area Poisson's ratio, respectively. Note that the area Poisson's ratio is bounded by $-1 < \nu < 1$, in contrast to the bounds $-1 < \nu' < 1/2$ for the $3d$ Poisson's ratio. The area bulk modulus K and the shear modulus G are expressed in terms of E and ν as [4],

$$K = \frac{E}{2(1-\nu)}$$

$$G = \frac{E}{2(1+\nu)}$$

so that

$$\frac{4}{E} = \frac{1}{K} + \frac{1}{G} \tag{8.3}$$

In this chapter we will use equations (8.2) and the various $2d$ elastic moduli (8.3). The $2d$ constitutive equations (8.2) are usually derived from (8.1) by assuming either *plane strain* or *plane stress*. We summarize the mappings from $3d$ to $2d$ for both plane strain and plane stress in Table 8.1. The $2d$ elastic constants discussed in this chapter may represent the effective in-plane elastic constants of a transversely isotropic material or a sheet containing inclusions, for example.

Table 8.1: The connection between the $2d$ elastic constants (unprimed) and the $3d$ elastic constants (primed) for both plane strain and plane stress.

Plane Strain	*Plane Stress*
$K = K' + \frac{G'}{3}$	$K = \frac{3K'+4G'}{9K'G'}$
$G = G'$	$G = G'$
$E = \frac{E'}{1-\nu'^2}$	$E = E'$
$\nu = \frac{\nu'}{1-\nu'}$	$\nu = \nu'$

8.3 CLM TRANSFORMATION AND THEOREM

A new result in plane elasticity which we refer to as the CLM theorem has recently been proved for $2d$ composite materials [1]. It is based on an earlier work of Lurie and Cherkaev [5]. The CLM theorem applies to linear elastic materials with general anisotropy and holds for an arbitrary geometry. In this chapter we are only concerned with the case where the components are isotropic, when the CLM theorem can be stated as follows.

Suppose that a $2d$ composite material has spatially varying bulk and shear moduli given by $K(\mathbf{r})$ and $G(\mathbf{r})$ respectively, and that the effective moduli of the material are K^* and G^*, then if

$$\frac{1}{K^t(\mathbf{r})} = \frac{1}{K(\mathbf{r})} - C \quad \text{and} \quad \frac{1}{G^t(\mathbf{r})} = \frac{1}{G(\mathbf{r})} + C \tag{8.4}$$

then

$$\frac{1}{K^{t*}} = \frac{1}{K^*} - C \quad \text{and} \quad \frac{1}{G^{t*}} = \frac{1}{G^*} + C \tag{8.5}$$

where the superscript t denotes the transformed system and C is a constant. Note that the constant C is restricted in order to ensure that the elastic moduli are positive everywhere in the transformed system. The vector $\mathbf{r}$ lies in the plane of the $2d$ material. We will refer to (8.4) as the CLM transformation, leading to the CLM

theorem (8.5). Under the CLM transformation the stress field is the same in both the original and the transformed material, for given external tractions, even though the elastic constants differ. Cherkaev, Lurie and Milton [1] refer to such materials as *equivalent.* The CLM theorem contains most other previously known exact results in $2d$ for composite systems, as special cases [1] [3]. In this chapter we are interested in the case where the elastic moduli are piecewise constant and the composite contains two phases only. The constraint on the allowed values of C means that the CLM theorem is most powerful in the limit when the inclusions are holes, and becomes useless in the limit where the sample contains rigid inclusion(s) which require that $C = 0$. In this chapter we focus our attention on the case when the inclusions are holes.

It is useful to rewrite the CLM transformation (8.4) in terms of the Young's modulus using (8.3) to give

$$E^t(\mathbf{r}) = E(\mathbf{r}) \tag{8.6}$$

which indicates that the Young's moduli of the material are invariant under the CLM transformation and to rewrite (8.5) as

$$E^{t*} = E^* \tag{8.7}$$

which states that the area Young's modulus of the composite is invariant under the CLM theorem.

8.4 DUNDURS CONSTANTS

The CLM transformation is related to an earlier result which is due to Dundurs [6] [7]. Dundurs showed that if a composite material consisting of two linearly elastic and isotropic phases is subjected to specified tractions and undergoes plane deformation, then the stress has a reduced dependence on the elastic constants. The stress depends on only *two* dimensionless parameters, as opposed to *three* dimensionless combinations

of elastic constants in $3d$. This can by written as

$$\sigma_{ij} = \sigma_{ij}(\mathbf{r}, \alpha_{12}, \beta_{12}) \tag{8.8}$$

where the vector $\mathbf{r}$ lies in the plane of the $2d$ material. The α_{12} and β_{12}, called Dundurs constants, are defined as

$$\alpha_{12} = \frac{\frac{1}{E_1} - \frac{1}{E_2}}{\frac{1}{E_1} + \frac{1}{E_2}}$$

$$\beta_{12} = \frac{\frac{1}{K_1} - \frac{1}{K_2}}{\frac{1}{E_1} + \frac{1}{E_2}} \tag{8.9}$$

The Dundurs result follows from the CLM transformation (8.4), which reduces the number of parameters by one. The parameters α_{12} and β_{12} are appropriate as they are clearly invariant under the CLM transformation. The Dundurs constants are not unique and other representations can be used.

A particularly important special case occurs when one of the components, say 2, becomes holes (of any size or shape). Then $K_2 = E_2 = 0$, leading to $\alpha_{12} = -1$ and $4\beta_{12} = -E_2/K_2 = -2(1-\nu_2)$. For holes, the dependence on Poisson's ratio remains in the Dundurs constants, but drops out in the expressions for stresses as expected from the result of Michell [8]. Michell showed that the stresses in a $2d$ multiply-connected body, induced by specified tractions, are independent of the elastic constants if the resultant force over each boundary vanishes are there are no body forces. This result led to the development of the photoelasticity method, an experimental technique of using optical birefringence in transparent materials to measure the stress fields. These stress fields depend only on the geometry of the holes and *not* on the elastic constants of the material.

8.5 A MATERIAL CONTAINING HOLES

If a $2d$ composite material is made by removing material to form holes (of any size, shape ,area fraction etc.), then *the relative area Young's modulus E^*/E of a 2d material containing holes is the same for all materials, independent of Poisson's ratio, for*

a prescribed geometry [2]. This result is easily proved by the CLM result [1] [3]. The CLM transformation leaves holes as holes, and therefore *any* matrix material can be reached by using the CLM transformation. Also, the effective area Young's modulus remains unaffected by the change in the Poisson's ratio as seen from (8.7).

To illustrate this special case of the CLM theorem, we recently considered a sheet with circular holes in various regular and random arrangements and used a computer simulation [2]. For simplicity these holes were all of the same size. We showed that the results all lie on a single function, independent of the Poisson's ratio of the matrix material, so that

$$E^{t*}/E^t = E^*/E \tag{8.10}$$

where E is the area Young's modulus of the matrix. The area Poisson's ratio of the composite can be written as

$$\nu^{t*} - \nu^* = (\nu^t - \nu)E^*/E \tag{8.11}$$

where we have used the values of the area Poisson's ratio ν and Young's modulus E of the matrix at the area fraction of holes $f = 0$ to eliminate the (unknown) constant C. This equation provided the *first rigorous proof* of the conjectured flow [9] [10] [11] of the Poisson's ratio to a fixed point at the percolation threshold [2] [3]. The result (8.11) shows explicitly that $\nu^{t*} = \nu^*$ as $E^*/E \to 0$. We have found numerically that for randomly centered circular holes with $\nu = 1/3$, the Poisson's ratio remains as $1/3$ to within numerical accuracy for all values of f [2]. It should be emphasized that the universal value of the area Poisson's ratio is only with respect to the elastic constants of the material; different geometries (arrangement and shape of inclusions) will lead to different universal values of the Poisson's ratio as percolation is approached.

8.6 A MATERIAL WITH POLYGONAL HOLES

Next, we consider a $2d$ material with regular polygonal holes (as shown in Fig. 8.1 for triangles) and investigate the relation between the shape of polygon and the effective

elastic moduli in the dilute limit.

When the area fraction of polygons f is small, to the leading order, the effective Young's modulus E^* can be written as

$$\frac{E^*}{E} = 1 - \alpha f \tag{8.12}$$

where E is the Young's modulus of the matrix and α is some positive constant which is a function of the shape of polygon only. From the CLM theorem, we know that for a given shape of polygon holes in a matrix, E^*/E is a universal curve which is independent of the Poisson's ratio of matrix. The relation (8.11) holds, so that to leading order in the area fraction f, we have

$$\nu^* = \nu + \beta f \tag{8.13}$$

where β is some constant depending upon the shape of the polygon only. By using (8.11), (8.12), and (8.13), we have

$$\nu^{t*} = \nu^t + f[\beta - \alpha(\nu^t - \nu)] \tag{8.14}$$

Therefore, if we choose

$$\nu^t = \nu_0 = \nu + \frac{\beta}{\alpha} \tag{8.15}$$

then $\nu^* = \nu$ to the leading order, and the term linear in f vanishes. We shall refer to this value of the Poisson's ratio ν_0 as the *invariant Poisson's ratio*, and the general result for the Poisson's ratio for small f can be written as

$$\nu^* = \nu - \alpha(\nu - \nu_0)f \tag{8.16}$$

For the rest of this chapter we will use the notation of (8.12) and (8.16). This means that if the matrix has an invariant Poisson's ratio given by (8.15), then the effective Poisson's ratio does not change (to the leading order in f) when a small concentration of polygon holes is cut in the matrix. If $\nu > \nu_0$, then the Poisson's ratio decreases with f, and vice versa, so that the Poisson's ratio tends to "flow towards" ν_0 as f increases.

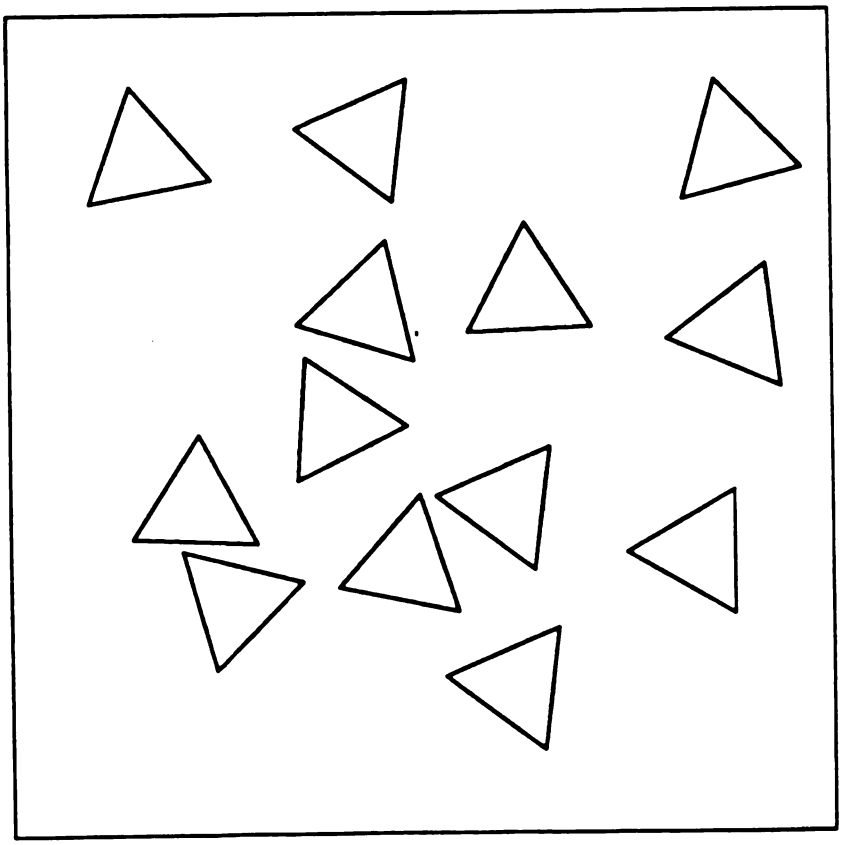

Figure 8.1: A sketch of a composite containing randomly positioned triangular inclusions.

The purpose of this work is to study the dependence of constants α and ν_0 on the shape of polygon. One of the extreme cases is that the polygon is a circular hole. In this case, $\alpha = 3$ and $\nu_0 = 1/3$, which can be calculated exactly using the result for a single circular inclusion. In the other cases, no analytical formulas are available yet. But from the Hashin's [12] second order bounds on E^*, we can show that $3 \leq \alpha < \infty$. We note that these bounds are attained for the circular and very thin elliptical inclusions respectively, and are therefore optimal.

8.7 SIMULATION RESULTS

We do the numerical simulation by using a digital-image-based method (see **Chapter 2** for details), in which we use a triangular net with central forces to represent the matrix. We place a single polygonal hole in a sample which is periodic. In order to calculate α and ν_0 accurately, we have to make the polygonal hole as small as possible. But on the other hand, the smaller the polygonal hole, the larger the finite size error. Therefore, there exists some tradeoff here. Furthermore, the exact area of the polygon is a rather ambiguous quantity due to the finite size effect. If the shape of the polygon is neither triangle nor hexagon, the situation is even worse, because in this case, it is harder to mimic the polygon exactly by cutting bonds in the triangular matrix. Of course, one can always increase the sample size to reduce the finite size error, but the computational time increases dramatically with the sample size. Other numerical methods, such as the finite element method, should give better results than we were able to obtain with the finite difference method used here. Nevertheless our results are accurate enough to be interesting.

In order to get precise results, we do our simulation in two ways. One way is to calculate the area by counting the number of pixels inside the polygonal hole and each pixel corresponds to some fixed area. The other way is that we define the area by calculating the exact area inclosed by the polygon, but the strength of the spring

Table 8.2: The values of α for use in (8.12) and the invariant Poisson's ratio ν_0, with estimated errors from the simulations, for regular polygonal holes.

n	α	ν_0
3 (triangle)	4.23 $\pm$ 0.02	0.227 $\pm$ 0.003
4 (square)	3.40 $\pm$ 0.04	0.302 $\pm$ 0.006
5 (pentagon)	3.25 $\pm$ 0.02	0.325 $\pm$ 0.003
6 (hexagon)	3.14 $\pm$ 0.02	0.328 $\pm$ 0.003
∞(circle)	3	0.333

constants for the bonds crossing the hole-matrix interface are reduced by a factor of 2. This is due to the fact that each bond at this interface is shared by both the matrix and the hole. The two sets of results of α and ν_0 given by these two methods are coincident when f is large, and the deviations become larger and larger when f becomes smaller and smaller. Fortunately, these deviations move away in opposite directions as the hole becomes smaller and f approaches 0, which enables us to take the arithmetic average of the two sets of data to reduce the finite size effect. After that, we use least-square-fit to interpolate the values of α and ν_0. Three different sample size, 102 $\times$ 102, 156 $\times$ 156 and 210 $\times$ 210, are used to estimate the finite size error and ν_0 in (8.16) is chosen to be 1/3. Because of the finite size error, we can only calculate α and ν_0 up to $n = 6$ (hexagon), which is converging rapidly on the large n limit of the circle. Note that all simulations were done with the spring constants of the triangular grid α, β and γ all set equal, so that the Poisson's ratio of the host was 1/3 [2]. Because of the CLM theorem, this single value of ν is sufficient to obtain the quantities of interest α and ν_0, which are given in the Table 8.2.

One special case is when the regular polygon is a *square*. In this case, the effective elastic moduli are *not* isotropic quantities. All other inclusions, with regular

polygons, lead to isotropic elasticity equations (8.2) for the composite, and no angular averaging is required. The square is different as the equivalent directions are at right angles which is not a sufficient symmetry to give isotropy, and three elastic constants, rather that two are required. We compute results for the stress parallel to the side of the square, and find that $\alpha = 3.78 \pm 0.02$ and the invariant Poisson's ratio $\nu_0 = 0.378 \pm 0.003$. Rotating the stress loading by $\pi/4$ so that it is along a diagonal of the square, we find that $\alpha = 3.00 \pm 0.02$ and the invariant Poisson's ration $\nu_0 = 0.205 \pm 0.003$. Averaging α and β and using (8.15), we obtain the results shown in Table 8.2. This is the correct procedure to first order in the area fraction f.

We emphasize that the results in Table 8.2 are for polygonal holes in continuum materials, and the grid was just a numerical device used in the computation. The results in Table 8.2 show a smooth evolution from the triangle to the circle, which is the limit of a regular n-sided polygon. The shape effect is surprisingly large, especially on the invariant Poisson ratio. Note that we could have added an $n = 2$ result for a slit, which can be obtained from the ellipse as the aspect ratio goes to zero. This would give $\alpha = \infty$ and zero for the invariant Poisson's ratio as can be seen by taking the limits on the equations for ellipses in the next section. In Fig. 8.2, we show plots of the results fitted to the following curves,

$$\alpha = 3 + \frac{33.21}{n^3} \quad \text{and} \quad \nu_0 = \frac{1}{3} - \frac{25.84}{n^5} \tag{8.17}$$

These fits were made by plotting the results against various power laws and choosing the one that came closest to giving a straight line. The result (8.17) may be useful in extending our work beyond $n = 6$, to estimate the difference between say an octagon and a circle. Notice that the result for the Young's modulus for the square does not fit onto the curves, which we find surprising as we expected a monotonic progression. The square is a different because of the averaging required and this may account for its different behavior.

As a concluding remark here, it is important to comment that for the geometry of polygonal holes with n finite the stress is singular in the matrix due to the sharp

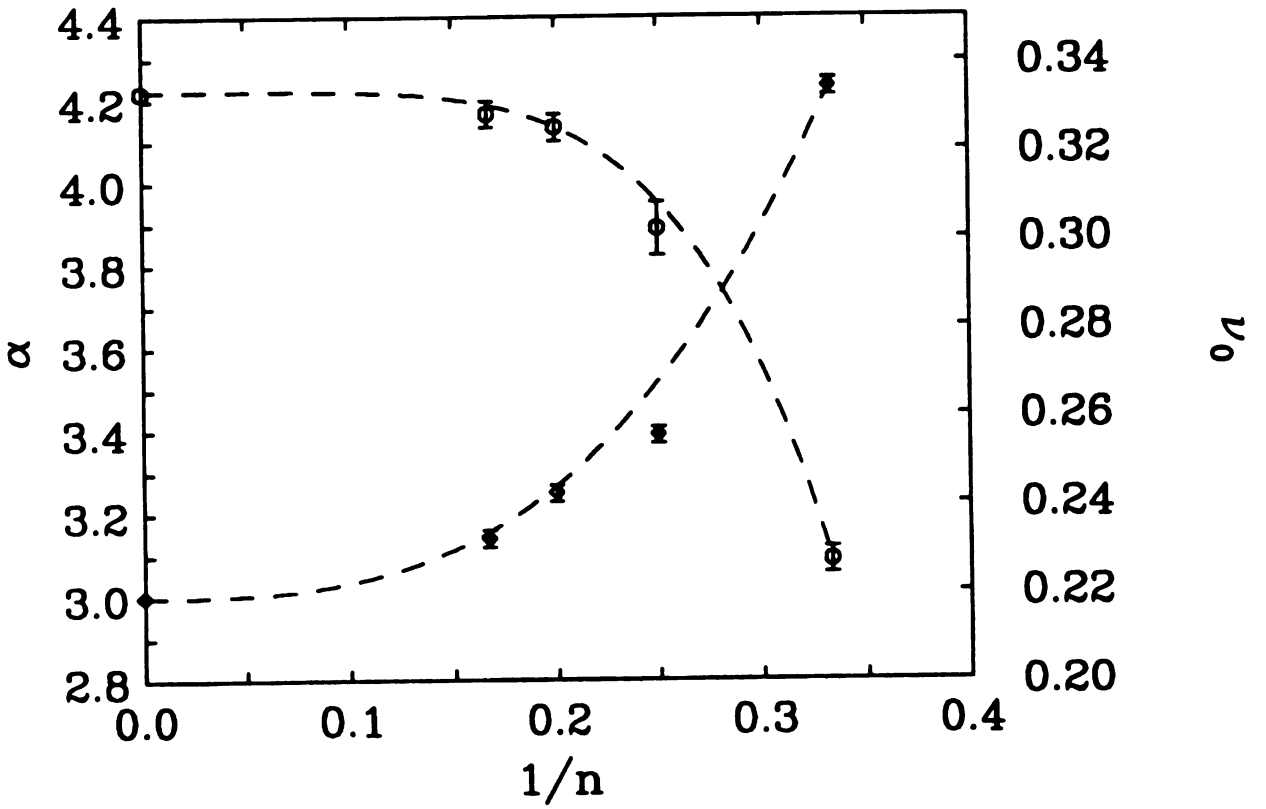

Figure 8.2: Showing the results for α and ν_0 for various n-gons, using the results from Table 8.2, and the power law fit (8.17).

corners. This is a geometric type of singularity [13] [14] and therefore the elastic strain energy is finite (or integrable). The elastic moduli are obtained directly from the elastic strain energy. However, this singularity can be removed by using the complex variable method of elasticity and conformal transformation. Recently, we successfully used these methods to obtain the analytical results for the coefficients of α and ν_0. They appeared to be in agreement with the simulation results with very high accuracy. The comparison between theory and simulation is listed in **Appendix A**.

8.8 EFFECTIVE MEDIUM THEORIES

The CLM theorem and the CLM transformation provide an important check on effective medium theories of composite materials in $2d$. It is clearly desirable that these approximate theories should be invariant under the CLM transformation. Because the dilute result is exact, it is of course invariant under the CLM transformation. The dilute result is used as the starting point in many effective medium theories. We have tested four commonly used methods, the self-consistent method [15] [16] [17], the differential scheme [18], the generalized self-consistent method [19], and the Mori-Tanaka method [20] [21], and we have found that in *any* of the above methods the CLM invariance is maintained.

Here, we will use our dilute results (8.12) and (8.16) along with Table 8.2 to predict the effective elastic moduli at higher volume fractions of holes by using two effective medium theories: the differential scheme and the self-consistent method.

The differential scheme is an iteration on the dilute limit such that incremental amounts of larger holes are embedded in a medium containing the previous level as an effective medium. Independent differential equations are obtained for the Young's modulus and the Poisson's ratio via,

$$\frac{dE}{E} = -\frac{\alpha df}{(1-f)} \tag{8.18}$$

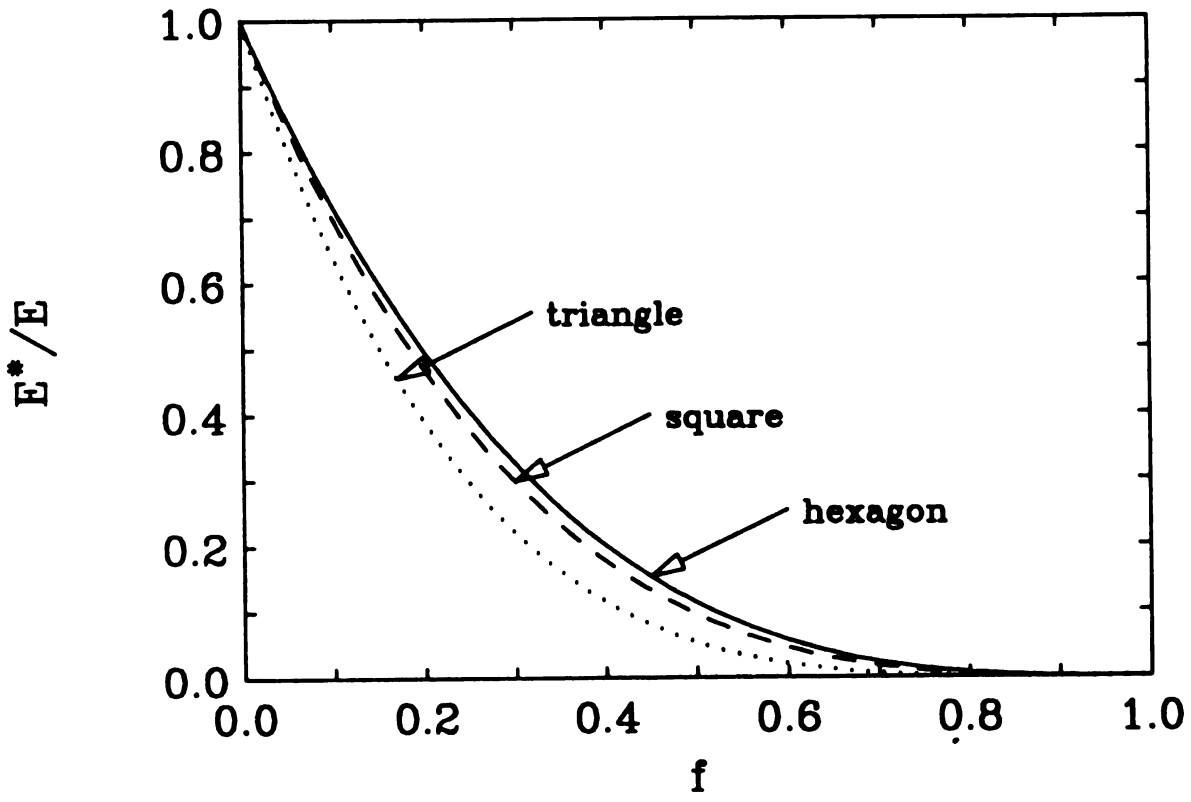

Figure 8.3: The Young's modulus E^* using the differential scheme (8.20) is shown for triangles, squares and hexagons.

and

$$d\nu = (\nu_0 - \nu)\frac{\alpha df}{(1-f)} \tag{8.19}$$

Equations (8.18) and (8.19) can be integrated, with the initial conditions that for small f, the dilute limits given in (8.12) and (8.16) are recovered. This is a standard technique that is explained in more detail in Jasiuk, Chen and Thorpe [22]. The results are

$$\frac{E^*}{E} = \frac{\nu^* - \nu_0}{\nu - \nu_0} = (1-f)^\alpha \tag{8.20}$$

The results (8.20) for the differential scheme, show that the Young's modulus goes to zero, and the Poisson's ratio $\nu^* \to \nu_0$ as $f \to 1$. The Young's modulus result is shown in Fig. 8.3 for triangles, squares and hexagons and gives an idea of the shape dependence of the result for a given area fraction of holes. This is qualitatively the same for all polygonal inclusions but differs in detail with the parameters α and ν_0 given Table 8.2. The differential scheme is set up to describe a composite containing regular polygons with a wide size variation. Equations (8.20) apply to the situation where there is a single type of inclusion (square etc.). However the result can easily be generalized to an arbitrary weighting of different types of polygons (triangles, squares etc.), by taking a weighted average of α and ν_0.

Similarly, we can use the self-consistent method to predict the effective elastic moduli of composites containing polygonal holes. Using the dilute result for E^* and ν^* given in (8.12) and (8.16) we can obtain the expressions for the effective bulk and shear moduli K^* and G^* which are related to E^* and ν^* via (8.3)

$$\frac{K^*}{K} = 1 - \alpha\left(\frac{1-\nu_0}{1-\nu}\right)f \tag{8.21}$$

$$\frac{G^*}{G} = 1 - \alpha\left(\frac{1+\nu_0}{1+\nu}\right)f \tag{8.22}$$

We can achieve self-consistency by replacing ν by ν^* on the right hand sides of equations (8.21) and (8.22).

$$\frac{K^*}{K} = 1 - \alpha\left(\frac{1-\nu_0}{1-\nu^*}\right)f \tag{8.23}$$

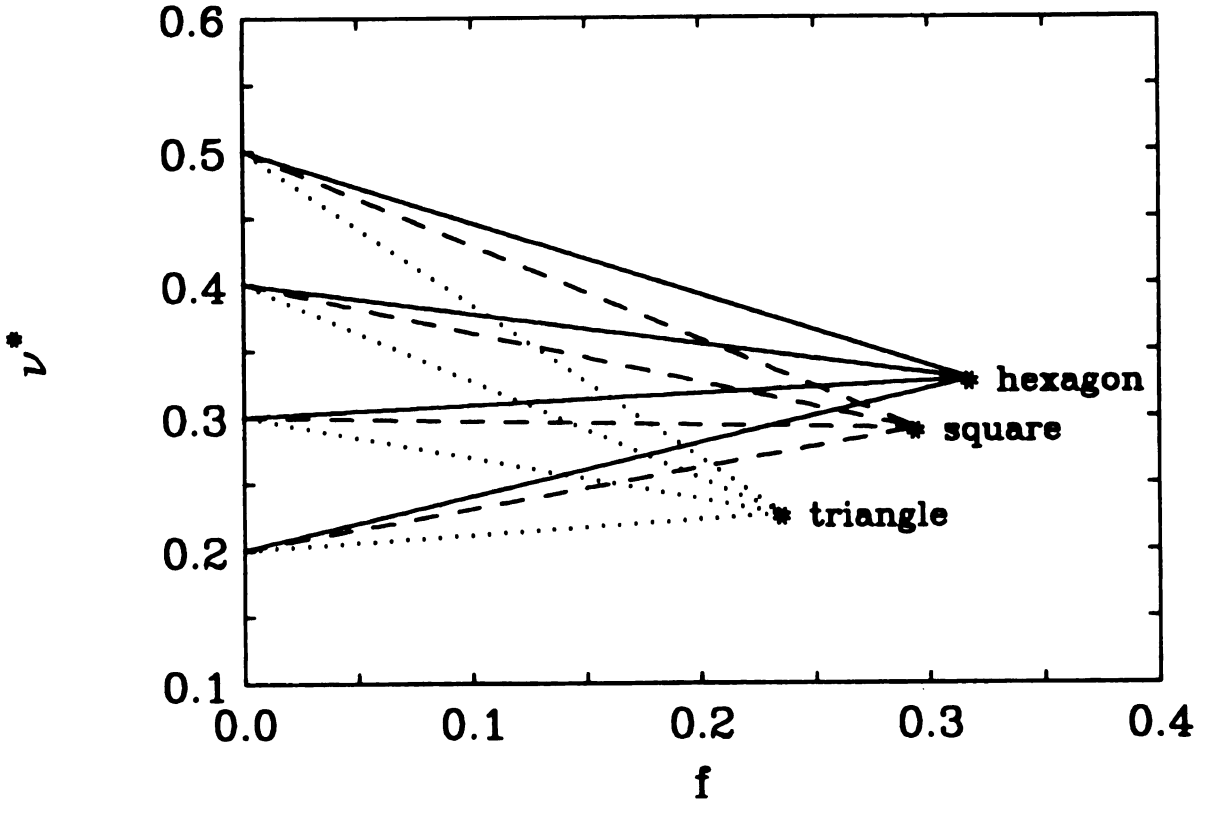

Figure 8.4: The Poisson's ratio ν^* using the self-consistent scheme (8.25) is shown for triangles, squares and hexagons. Here, the star * marks the fixed point of Poisson's ratio which is at ν_0.

$$\frac{G^*}{G} = 1 - \alpha\left(\frac{1+\nu_0}{1+\nu^*}\right) f \tag{8.24}$$

We combine these equations via (8.3) to form equations for E^* and ν^*.

$$\frac{E^*}{E} = \frac{\nu^* - \nu_0}{\nu - \nu_0} = 1 - \alpha f \tag{8.25}$$

which are the same as the dilute results (8.12) and (8.16). The result (8.25) for the Poisson's ratio is plotted in Fig. 8.4 for the cases of triangles, squares and hexagons. It can be seen that *both* the invariant value of the Poisson's ratio *and* the critical value of the are fraction f are sensitive to the type of polygon.

Substituting (8.25) into (8.23) and (8.24) we have the following expressions for K^* and G^*

$$\frac{K^*}{K} = 1 - \alpha\frac{(1-\nu_0)}{[(1-\nu) + f\alpha(\nu - \nu_0)]} f \tag{8.26}$$

$$\frac{G^*}{G} = 1 - \alpha\frac{(1+\nu_0)}{[(1+\nu) - f\alpha(\nu - \nu_0)]} f \tag{8.27}$$

The results (8.23) and (8.24) for the self-consistent method show that the moduli go to zero and the Poisson's ratio $\nu^* \to \nu_0$ at the area fraction $f = 1/\alpha$.

The present result for the self-consistent method complements an earlier study which was done for elliptical inclusion [4]. For this case, the area Young's modulus and the area Poisson's ratio are

$$\frac{E^*}{E} = 1 - f/f_c$$

and

$$\nu^* = \nu - (\nu - \nu_c) f/f_c \tag{8.28}$$

where

$$\nu_c = 1/(\frac{a}{b} + \frac{b}{a} + 1)$$

and

$$f_c = 1/(\frac{a}{b} + \frac{b}{a} + 1) \tag{8.29}$$

Here b/a is the aspect ratio of the randomly oriented and randomly centered ellipses, and the subscripts c denotes the quantity at percolation. Here, the subscript c has the same meaning as the subscript 0 used earlier in this section.

We comment that these effective medium equations at least have a structure compatible with the CLM theorem. Although this compatibility is desirable, it is of course not sufficient to ensure a good effective medium theory. A good figure of merit is given by the percolation concentration. For circular holes, equation (8.29) gives $f_c = 1/3$ which is far from the exact result of $f_c = 0.66$ [23]. Note that in any dimension, the percolation concentration is a geometrically determined quantity that is independent of the Poisson's ratio; any effective medium theory that is invariant under the CLM transformation ensures that this is achieved for holes.

Finally, we comment on the results for a material with planar cracks which exist in literature. The dilute result is

$$\frac{E^*}{E} = 1 - \eta\pi \tag{8.30}$$

$$\nu^* = \nu(1 - \eta\pi) \tag{8.31}$$

where η is a crack density parameter defined by $\eta = Na^2/A$ where N is a number of cracks, the length of the crack is $2a$, and A is the area of the sample. The self-consistent result due to Gottesman [24] is

$$\frac{E^*}{E} = 1 - \eta\pi \tag{8.32}$$

$$\frac{G^*}{G} = 1 - \frac{\eta\pi}{(1 + \nu - \eta\pi\nu)} \tag{8.33}$$

Please note that our results reduce to (8.32) and (8.33) if we set $\nu_0 = 0$ and $\alpha f = \eta\pi$. The differential scheme solution of Salganik [25] gives

$$\frac{E^*}{E} = \frac{\nu^*}{\nu} = e^{-\eta\pi} \tag{8.34}$$

The Mori-Tanaka result obtained by Benveniste [26] yields

$$\frac{E^*}{E} = \frac{1}{1 + \eta\pi} \tag{8.35}$$

$$\nu^* = \nu(1 - \eta\pi) \tag{8.36}$$

As discussed earlier, the CLM result is particularly powerful for holes, where it shows that the Young's modulus should be independent of the Poisson's ratio of the material, and the Poisson's ratio should flow to a universal value at the fixed point [2]. Please note that in all the results discussed in this section the Young's modulus is indeed independent of the Poisson's ratio.

8.9 DISCUSSION

In this chapter, we have drawn together and discussed a number of exact results for $2d$ composite materials. These results begin historically with the result of Michell [8] concerning the stresses in plates containing holes, and are all brought together by a recent theorem proved by Cherkaev, Lurie and Milton [1]. We have discussed the special case of a material containing holes and showed that the effective area Young's modulus is independent of the Poisson's ratio of the matrix. We presented the results for the elastic constants of a material containing polygonal holes and also discussed other geometries such as circular, elliptical and slitlike (crack) holes. We have also pointed out that effective medium theories in $2d$ should reflect the transformation properties in the CLM theorem.

Bibliography

[1] A. Cherkaev, K. Lurie and G. W. Milton, Proc. Roy. Soc. A, **438**, 519 (1992).

[2] A. R. Day, K. A. Snyder, E. J. Garboczi and M. F. Thorpe, J. Mech. Phys. Solids, **40**, 1031 (1992).

[3] M. F. Thorpe and I. Jasiuk, Proc. Roy. Soc. A, **438**, 531 (1992).

[4] P. N. Sen and M. F. Thorpe, J. Accout. Soc. Am., **77**, 1674 (1985).

[5] K. A. Lurie and A. V. Cherkaev, Uspeckhi Mekaniki (Adv. in Mech.), **9**, 3, in Russian (1986).

[6] J. Dundurs, J. Comp. Mats., **1**, 310 (1967).

[7] J. Dundurs, Recent Advances in Engineering Science, Vol. 5, p.203, edited by A.C. Eringen, Gordon and Breach (1970).

[8] J.H. Michell, Proc. London Math. Soc., **31**, 10 (1899).

[9] E. J. Garboczi and M. F. Thorpe, Phys. Rev. B, **31**, 7276 (1985).

[10] L. M. Schwartz, S. Feng, M. F. Thorpe and P. N. Sen, Phys. Rev. B, **32**, 4607 (1985).

[11] E. J. Garboczi and M. F. Thorpe, Phys. Rev. B, **33**, 3289 (1986).

[12] Z. Hashin, J. Mech. Phys. Solids, **13**, 119 (1965).

[13] N. I. Muskhelishvili, Some Basic Problems of the Mathematical Theory of Elasticity, P. Noordhoff Ltd., Gronongen, Holland (1953).

[14] S. Timoshenko and J. N. Goodier, Theory of Elasticity, 2nd. edition, McGraw-Hill, New York (1951).

[15] B. Budiansky, J. Mech. Phys. Solids, **13**, 223 (1965).

[16] R. Hill, J. Mech. Phys. Solids, **13**, 213 (1965).

[17] T.T. Wu, Int. J. Solids Struct., **2**, 1 (1966).

[18] R. McLaughlin, Int. J. Eng. Science, **15**, 237 (1977).

[19] R. M. Christensen and K. H. Lo, J. Mech. Phys. Solids, **27**, 223 (1979).

[20] T. Mori and K. Tanaka, Acta Metallurgica, **21**, 571 (1973).

[21] Y. Benveniste, Mech. of Materials, **6**, 305 (1989).

[22] I. Jasiuk, J. Chen and M. F. Thorpe, Applied Mechanics Reviews, **47**, No. 1, Part 2, January (1994).

[23] W. Xia and M. F. Thorpe, Phys. Rev. A, **38**, 2650 (1988).

[24] T. Gottesman, Ph.D. thesis, Tel-Aviv University (1980).

[25] R. L. Salganik, Mechanics of Solids, **8**, 149 (1973).

[26] Y. Benveniste, Mech. Res. Comm., **13**, 193 (1986).

Chapter 9

CONCLUSION

The thesis covered most of my research at Michigan State University during my study toward the Ph.D. degree. I chose composite materials as my main research area because I believed that composite was the direction of a new generation of materials. Although composite was known for more than two-thousand years, its development had been very slow until thirty years ago.

Since the 1960s' commercial and military prospects have stimulated the study of composite materials. Until the beginning of 1980, most of the study was concentrated on the experimental work and theoretical analysis. But the fast development of computer science created a new era of composite materials. Since 1980 more and more composites have been studied, tested or designed on computers. As we know, the equations describing composites are often non-linear fourth-order differential equations. There is no way to solve such equations analytically except for some very simple geometries or by introducing some assumptions (such as small concentration of inclusions, no interaction between inclusions, etc.). If the concentration of inclusions is relatively large (but not so close to the rigidity percolation limit), then **no** current theory can describe such composites precisely. Therefore, I made a lot of effort in developing software to study the elastic and structural properties of composites numerically. All of the simulations in the thesis were developed and performed

by myself.

After giving a brief introduction to composite materials in **Chapter 1**, I introduced (in **Chapter 2**) two simulation techniques which were widely used in the thesis. Then (in **Chapter 3**) we set up a model for fiber-reinforced composites and particulate-reinforced composites. In that model, we introduced an interface slipping coefficient to take into account the friction on the inclusion-matrix interface. This factor was important in describing the adhesion on the inclusion-matrix interface, since the boundary condition was neither perfectly bonded nor purely sliding on the interfaces in real composite materials. Our model could also recover the results for perfect-bonding and pure-sliding as special cases, which was a check on the correctness of the model. In **Chapter 4** and **5** we studied the elastic and structural behaviors of composites with rigid inclusions. In **Chapter 4** we assumed perfectly-bonded interface conditions and used the digital-image-based method; while in **Chapter 5** we assumed purely-sliding interface conditions and used the finite element method. In **Chapter 6** we studied the relation between local geometry and local strain. It appeared to be important in practice because we could determine the stress distribution from the geometric parameters. In **Chapter 7** we verified the bounds for composites numerically. In **Chapter 8** we studied the $2d$ porous materials in which the holes could be arbitrary polygons. After finishing the computer simulation, we solved this problem analytically by using a conformal mapping method, and found that the results between simulation and theory agreed nicely. The theoretical work using the conformal mapping method was briefly discussed in **Appendix A**.

We have also made some progress in the study of the elastic properties of a two-dimensional matrix containing elliptical holes or cracks. The computer simulation setup and some results were presented in **Appendix B**.

Recently we did a lot of work in studying the anisotropy in composite materials and porous materials. Several months ago we found a very interesting phenomenon. The basic claim is as follows. For a composite with arbitrary isotropic components,

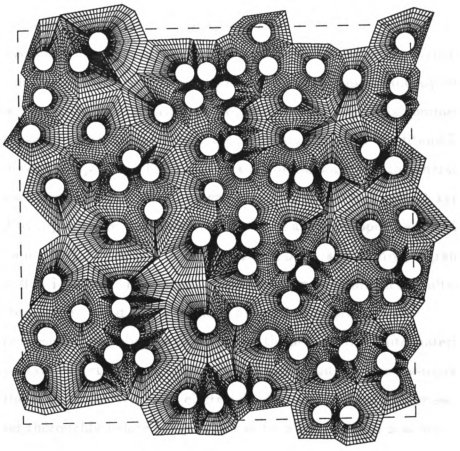

Figure 9.1: Showing a typical mesh generated by my ABAQUS preprocessor for random fiber-reinforced composites.

its effective elastic properties are anisotropic in general. But if these components have the same shear modulus, then the composite becomes isotropic again. This claim is true for **any** geometry in **any** dimensions. A paper on this work is being written now, and most of the work was not included in the thesis. (A particular $2d$ example of this work was briefly addressed in **Appendix C**).

This thesis has concentrated on the study of the elastic and structural properties of composite materials. It does not cover another important aspect – plastic properties. Recently I developed a preprocessor for ABAQUS (a commercial finite element package) which could generate the mesh and boundary conditions for random fiber-reinforced composites. The basic idea of the software was to generate Voronoi cells for each configuration, and then generate a mesh for each cell. A typical mesh generated by my software was shown in Fig. 9.1. I also developed an ABAQUS input program, and Dr. L.C. Davis at Ford Motor Company is using my program to study the plastic flow in $2d$ fiber-reinforced composites. Some preliminary results have been obtained but not included in the thesis. This work is in progress now.

My thesis covers only a small portion of the field of composite materials. Many other important aspects of composites are also important, such as elastoplastic deformation, thermal conductivity and electric conductivity. Those properties should be understood thoroughly before composites can be widely used in practice. Personally I believe that composite materials have a very brilliant future, and they will become one of the major materials used in the next century. Finally, let me conclude my thesis with one example. I visited the engineering division in Ford Motor Company recently. Ford is developing a new generation of cars. A major character of the design is to replace the metal body of cars by composite materials. This change will reduce the weight of cars significantly and increase the mileage per gallon. The body made of composite materials can also resist against corrosion, which is a big problem for vehicles driven in winters in high latitude regions, such as in Michigan. Of course, we should always choose strong composites to guarantee the safety, and make composite

cars cheap enough to compete on the market.

Appendix A

CONFORMAL MAPPING

The complex variable method of elasticity and conformal transformation have been successfully used to solve many problems of practical importance [1] [2] [3]. Here I first summarize this approach and then use this method to study the problem in which a single polygonal hole embedded in an isotropic, homogeneous, and linear elastic sheet which is subjected to a uniform remote stress.

Recall from complex variable theory that if we have two complex domains S and Σ in the z and ξ planes respectively, the conformal transformation is given by

$$z = w(\xi) \tag{A.1}$$

where w is a holomorphic function and $\xi = \rho e^{iv}$, where ρ and v are polar coordinates. If both the domains S and Σ are infinite, this transformation is of the form

$$w(\xi) = B\left(\xi + \sum_{n=1}^{\infty} a_n \xi^{-n}\right) \tag{A.2}$$

If we want to transform the exterior of a unit circle in the ξ plane into the exterior of the regular polygon in the z plane (such that the center of the circle corresponds to the center of the polygon), we use the following transformation

$$\begin{aligned} w(\xi) = B\,[\,\xi \;+\; & \frac{2}{n(n-1)\xi^{n-1}} + \frac{n-2}{n^2(2n-1)\xi^{2n-1}} + \frac{(n-2)(2n-2)}{3n^3(3n-1)\xi^{3n-1}} \\ & + \frac{(n-2)(2n-2)(3n-2)}{12n^4(4n-1)\xi^{4n-1}} + \ldots\,] \end{aligned} \tag{A.3}$$

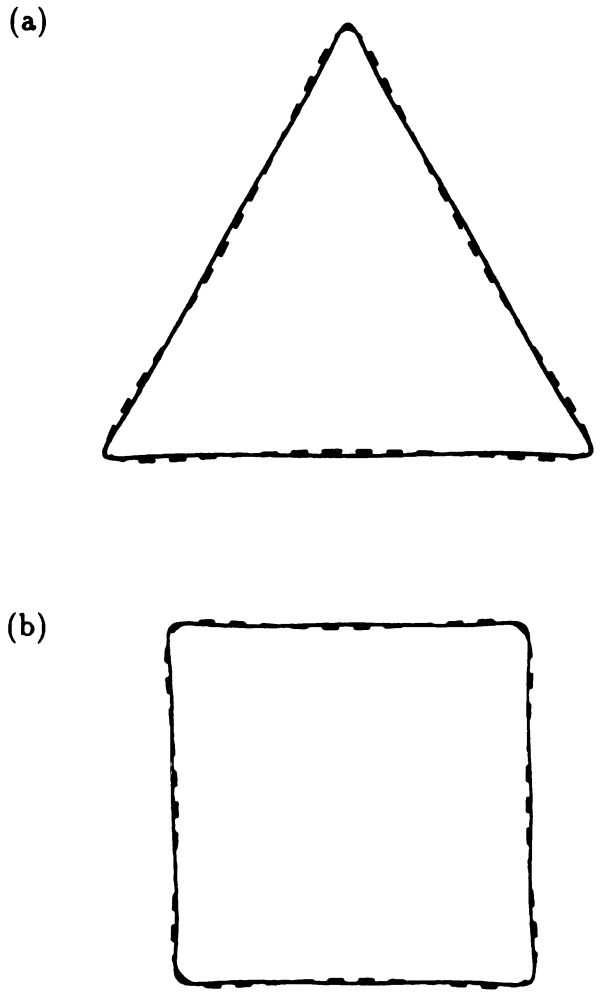

Figure A.1: The shape corresponding to the conformal mapping given in Eqn. (A.3) with $n = 3$ (a) and $n = 4$ (b). The dashed line corresponds to truncating the series after 2 terms and the solid line is the first three terms. In the limit of an infinite number of terms a perfect triangle is obtained. For the triangle the area of the dashed figure is 1.0037 that of the corresponding perfect triangle; the area of the solid figure is 1.00055 that of the perfect triangle.

where $n = 3, 4, 5$ ... (n is the number of sides in a polygon), and $B = Re^{i\delta}$, where R is a real constant and δ is the angle rotated from the original position of the polygon. The full transformation for a polygon is of the Schwarz-Christoffel type and Eqn. (A.2) is the expanded form of this transformation. If only first few terms of the series in Eqn. (A.2) are used the polygon has rounded off corners as seen in Fig. A.1. The parametric equations for the hole can be obtained by setting $\rho = 1$ in ξ and separating real and imaginary parts.

After finding the stress and displacement in the ξ plane (with circular holes embedded in a matrix), we can transform it back to the z plane in order to finding the solution for cutting polygonal holes in a matrix. The detailed calculations can be find in the paper co-authored by Jasiuk, Chen and Thorpe (1994) [4]. Here, only the comparison between theory and simulation is shown in Table A.1 - A.4.

Table A.1: Analytical and numerical values for parameters α and ν_0 for triangular holes. The analytical results correspond to including the first leading term, the first two leading terms, etc., in the transformation function.

Triangle	α	ν_0	
Simulation	4.23 ± 0.02	0.227 ± 0.003	
Analytical	4.212933335	0.2294649836	8 terms
	4.212224861	0.2295642570	7 terms
	4.211197346	0.2297117902	6 terms
	4.209613384	0.2299460752	5 terms
	4.206953267	0.2303542646	4 terms
	4.201867155	0.2311712346	3 terms
	4.189725712	0.2332287784	2 terms
	4.142857143	0.2413793103	1 term

Table A.2: Analytical and numerical values for parameters α and ν_0 for square holes. All of the results are obtained after proper average. The analytical results correspond to including the first leading term, the first two leading terms, etc., in the transformation function.

Square	α	ν_0	
Simulation	3.40 ± 0.04	0.302 ± 0.006	
Analytical	3.475848056	0.3060811063	8 terms
	3.475276566	0.3061198202	7 terms
	3.474452775	0.3061765414	6 terms
	3.473192339	0.3062651450	5 terms
	3.471096666	0.3064165109	4 terms
	3.467151661	0.3067120130	3 terms
	3.458021706	0.3074301794	2 terms
	3.425974026	0.3100833965	1 term

Table A.3: Analytical and numerical values for parameters α and ν_0 for pentagonal holes. The analytical results correspond to including the first leading term, the first two leading terms, etc., in the transformation function.

Pentagon	α	ν_0	
Simulation	3.25 ± 0.02	0.325 ± 0.003	
Analytical	3.239613248	0.3232906379	8 terms
	3.239255869	0.3233062956	7 terms
	3.238740430	0.3233291756	6 terms
	3.237951454	0.3233648103	5 terms
	3.236639718	0.3234254651	4 terms
	3.234174238	0.3235432913	3 terms
	3.228506463	0.3238272630	2 terms
	3.209183673	0.3248542660	1 term

Table A.4: Analytical and numerical values for parameters α and ν_0 for hexagonal holes. The analytical results correspond to including the first leading term, the first two leading terms, etc., in the transformation function.

Hexagon	α	ν_0	
Simulation	3.14 ± 0.02	0.328 ± 0.003	
Analytical	3.137612182	0.3288189915	8 terms
	3.137389658	0.3288260221	7 terms
	3.137067766	0.3288363187	6 terms
	3.136573466	0.3288523724	5 terms
	3.135748900	0.3288797632	4 terms
	3.134194426	0.3289330861	3 terms
	3.130618072	0.3290617689	2 terms
	3.118550369	0.3295253102	1 term

Bibliography

[1] N. I. Muskhelishvili, Some Basic Problems of the Mathematical Theory of Elasticity, P. Noordhoff Ltd., Groningen, Holland (1956).

[2] G. N. Savin, Stress Concentration Around Holes, Pergamon Press, New York (1961).

[3] M. F. Thorpe, Proc. Roy. Soc. A, **437**, 215 (1992).

[4] I. Jasiuk, J. Chen and M. F. Thorpe, Applied Mechanics Reviews, **47**, No. 1, Part 2, January (1994).

Appendix B

THE SHEET CONTAINING ELLIPTICAL HOLES OR CRACKS

I studied the effective elastic properties for a $2d$ sheet containing elliptical holes or cracks by digital-image-based method which was described in **Chapter 2**. The elliptical holes or cracks were randomly distributed in the matrix. They could be either overlapping or nonoverlapping. The orientation of the elliptical holes or cracks could be along one particular direction or could be random. Two typical configurations were shown in Fig. B.1 and B.2. After applying external loadings in different directions, the effective elastic properties along those directions were obtained.

Several results are presented in Fig. B.3 through Fig. B.6. Fig. B.3 corresponds to the configuration shown in Fig. B.1 in which all of the elliptical holes are along the horizontal direction (11 direction). It shows the effective elastic compliance S^c_{11}, S^c_{22} and $2S^c_{12} + S^c_{33}$ with respect to the area fraction of the holes. Here I use superscript c to denote *composites*, and all of the symbols without superscripts correspond to the parameters of the uniform *matrix*. The dashed lines in Fig. B.3 in the low concentration region are obtained from the analytical calculations. The results

are as follows.

$$\frac{S_{11}}{S_{11}^c} = 1 - f\left(1 + \frac{2b}{a}\right) ,$$

$$\frac{S_{22}}{S_{22}^c} = 1 - f\left(1 + \frac{2a}{b}\right) ,$$

$$\frac{(2S_{12} + S_{33})}{(2S_{12}^c + S_{33}^c)} = 1 - f\left(1 + \frac{a}{b} + \frac{b}{a}\right) . \tag{B.1}$$

where a and b are the two semi-axes of the elliptical holes (semi-axis a is along the 11 direction), and f is the area fraction of the elliptical holes.

Furthermore, S_{11}^c, S_{22}^c and $2S_{12}^c + S_{33}^c$ are invariant under CLM transformation. This means that the quantities S_{11}/S_{11}^c, S_{22}/S_{22}^c, and $(2S_{12} + S_{33})/(2S_{11}^c + S_{33}^c)$ are invariant quantities for different values of the Poisson's ratios of the matrix. This result is true for any concentration of the holes, and is obviously true in the dilute region as shown in the Eqs. (B.1). Therefore, for simplicity I always use the matrix with Poisson's ratio $\nu_0 = 1/3$ in computer modeling.

Fig. B.4 shows the effective Young's modulus and Poisson's ratio for a sheet containing overlapping, randomly oriented elliptical holes. In the Young's modulus plot, the result is also compared with that of cutting circular holes in an identical sheet.

The simulation for a matrix with single crack is performed. Since the analytical solution of this problem exists [1], it is a good check for the correctness of my program. Fig. B.5 shown the comparison between simulation data and the analytical solution (solid curve), and they agree well with each other.

Fig. B.6 corresponds to cutting cracks randomly (both position and orientation) on a $2d$ sheet. In this figure $2a$ is the length of the cracks and n is the number of cracks per unit area. We use n because cracks have no area. The solid line in the dilute region is also obtained analytically, which is given by

$$\frac{\langle E^c \rangle}{E} = \frac{\langle \nu^c \rangle}{\nu} = 1 - n\pi a^2 \tag{B.2}$$

where $\langle E^c \rangle$ and $\langle \nu^c \rangle$ are the effective Young's modulus and Poisson's ratio respectively, and E and ν are the corresponding quantities for the matrix.

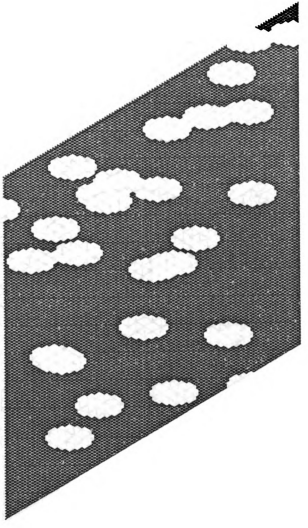

Figure B.1: Showing the simulation setup for a matrix containing randomly distributed elliptical holes. All of the holes are oriented in the horizontal direction, and are allowed to overlap.

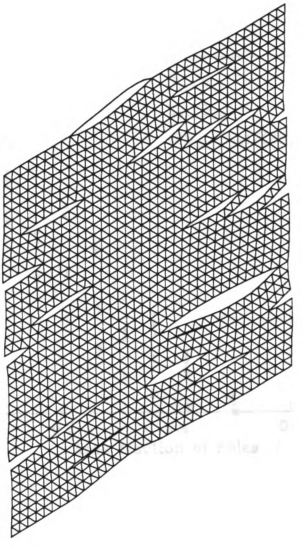

Figure B.2: Showing the simulation setup for a matrix containing randomly distributed cracks. All of the cracks are oriented in a certain direction, and are allowed to overlap. This is the equilibrium shape of the sheet when a uniform strain is applied in the vertical direction.

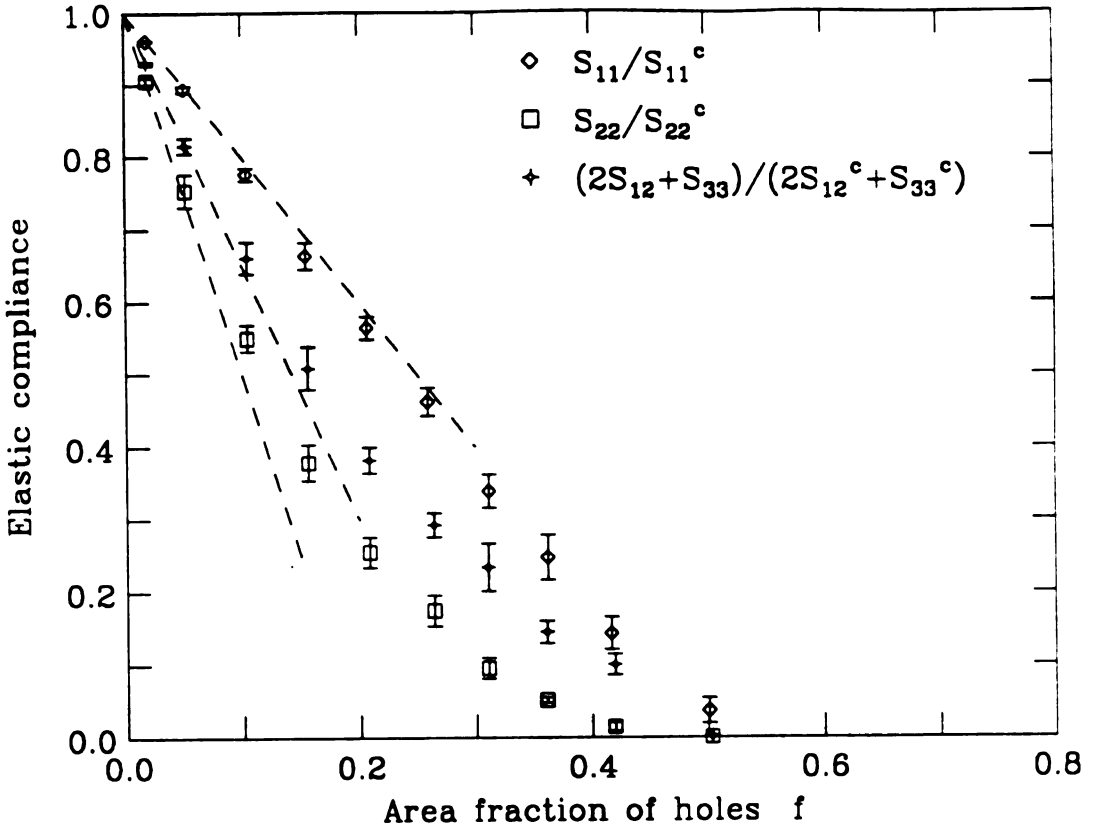

Figure B.3: Showing the elastic compliance for a matrix containing randomly distributed overlapping elliptical holes, as shown in Fig. B.1. All of these elliptical holes are oriented in the horizontal direction. The ratio between two semi-axes of an elliptical hole is $a/b = 2$. The symbols are simulation data, and the dashed lines are the analytical results in dilute region. The data are averaged over 5 different configurations, and the error bar is given for each data point.

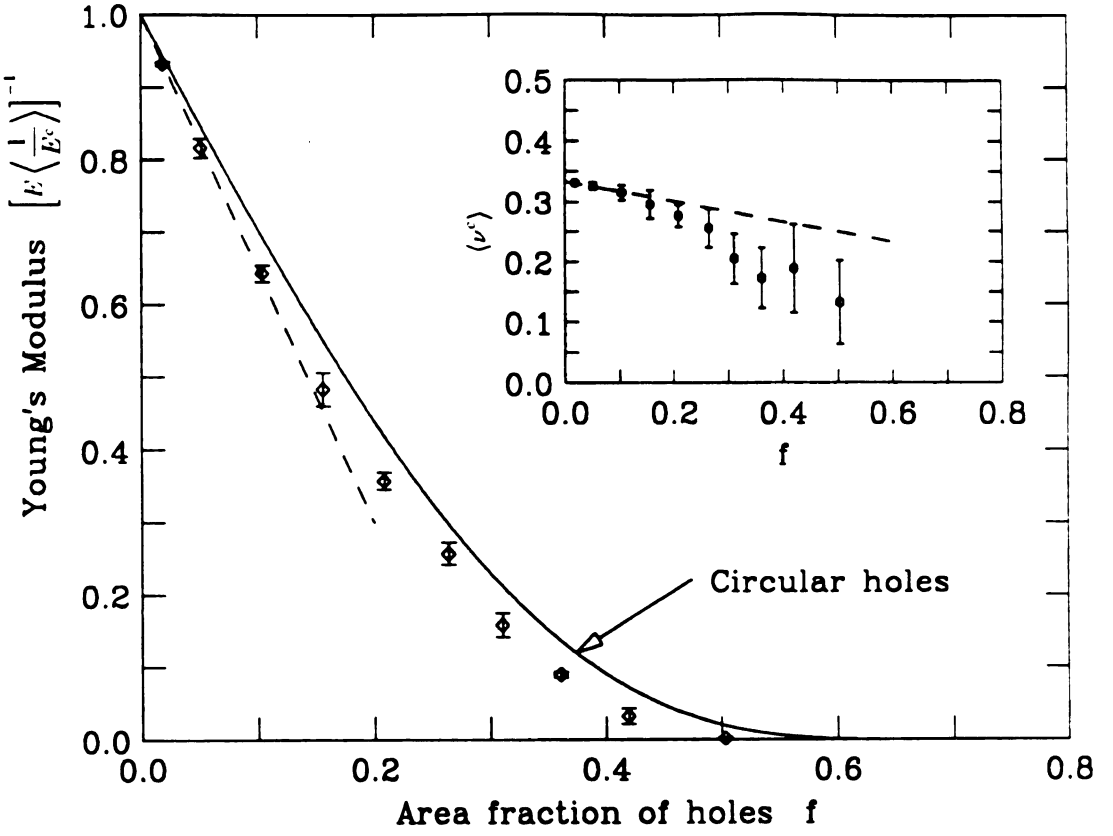

Figure B.4: Showing the effective Young's modulus and Poisson's ratio for a matrix containing randomly distributed, oriented, overlapping elliptical holes. The solid line is the similar result but for the circular shaped holes. The symbols are simulation data, and the dashed lines are the analytical results in dilute region. The data are averaged over 5 different configurations, and the error bar is given for each data point.

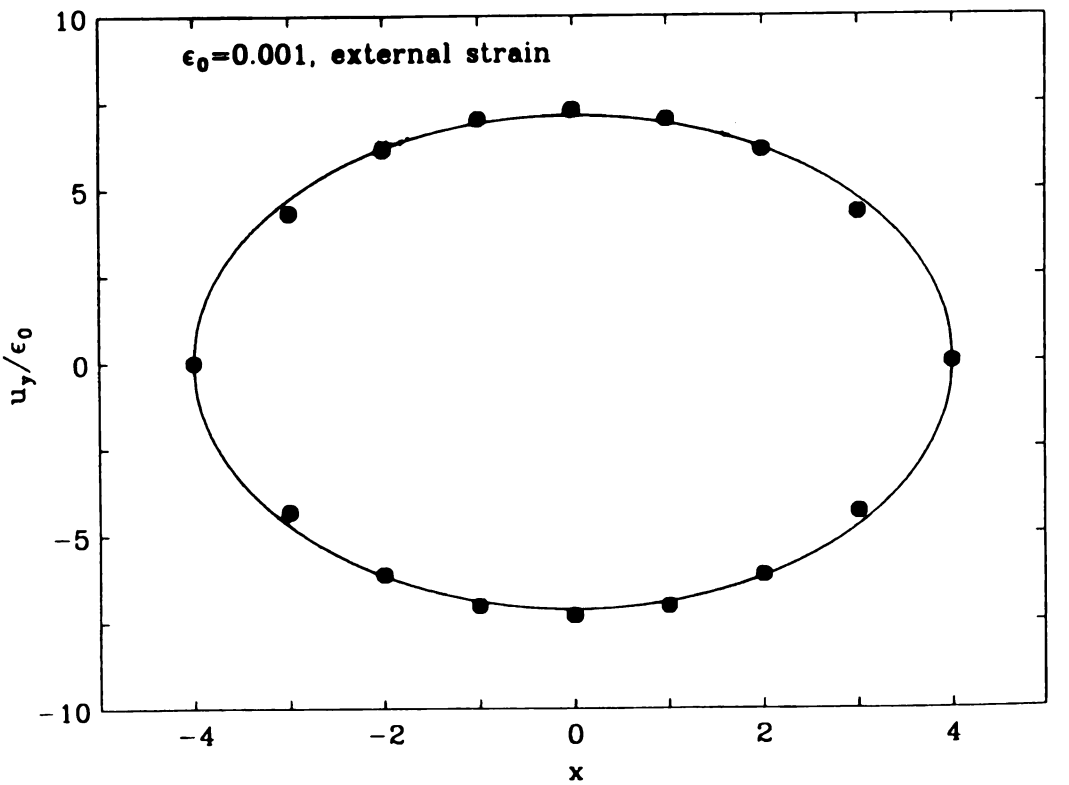

Figure B.5: Showing the displacement u_y on the two sides of a single crack cut in a uniform matrix. A uniform external strain $\epsilon_0 = 0.001$ is applied in the direction perpendicular to the crack.

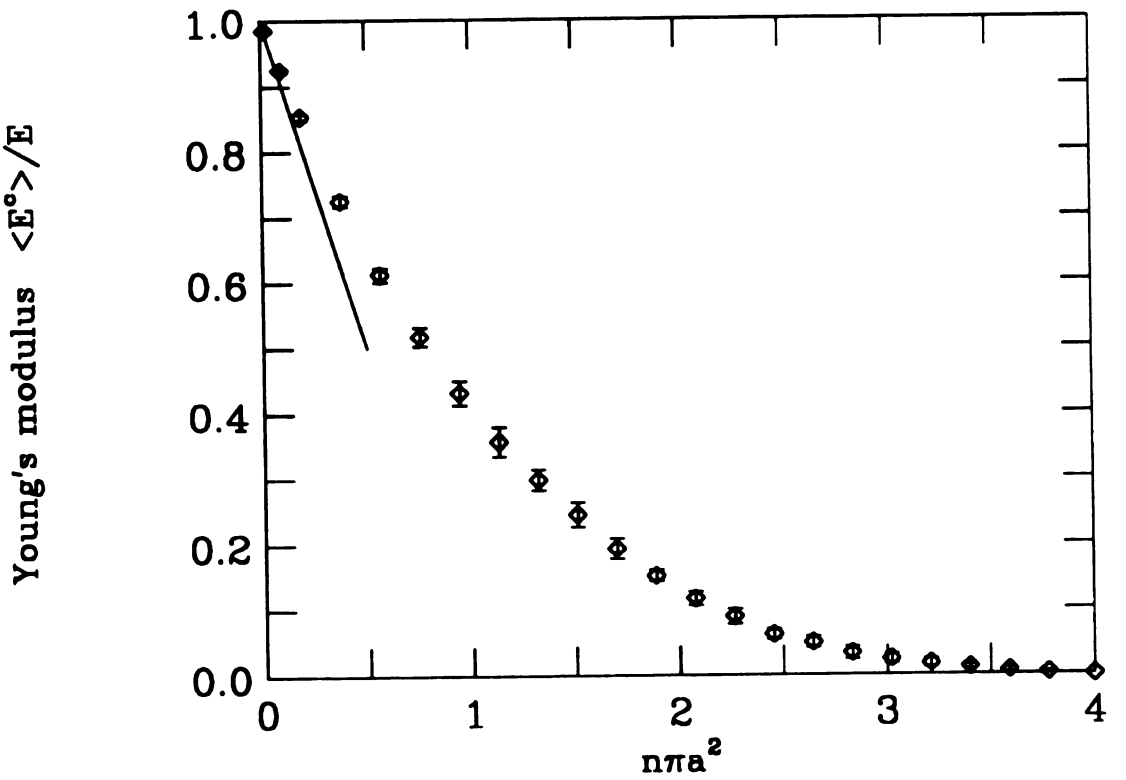

Figure B.6: Showing the effective Young's modulus for a matrix containing randomly distributed, oriented, overlapping cracks. The symbols are simulation data, and the solid line is the analytical result in dilute region. The data are averaged over 5 different configurations, and the error bar is given for each data point.

Bibliography

[1] I. N. Sneddon and M. Lowengrub, Crack Problems in the Classical Theory of Elasticity, New York (1969).

Appendix C

HILL'S THEOREM FOR AN N-SLAB IN D-DIMENSIONS

Recently we found a very interesting phenomenon while studying the anisotropy of composite materials. For a composite with arbitrary isotropic components, its effective properties are anisotropic in general. But if these components have the same shear modulus, we have proved analytically that the composite becomes isotropic again. This result is implicit in Hill's paper, but it is not entirely clear if he understood that his theorem is valid even when the geometry is arbitrary and not isotropic. In fact the result is true for **any** geometry. This claim is valid in any dimension d ($d \geq 2$), and will become more clear through the following example. This slab geometry is the most anisotropic geometry that one can imagine, and was suggested to us by R. W. Zimmerman during his visit to MSU at the end of 1993.

Let's consider a d-dimensional slab with N elements, as shown in Fig. C.1. The volume fraction of element i is f_i ($\sum_{i=1}^{N} f_i = 1$), and its Poisson's ratio, Young's modulus, and shear modulus are ν_i, E_i and μ_i respectively. Assume that all of the elements have the same shear modulus, *i.e.*, $\mu_i = \mu$ for any i-th element. I proved analytically that this slab was isotropic, and its effective Poisson's ratio ν^* could be

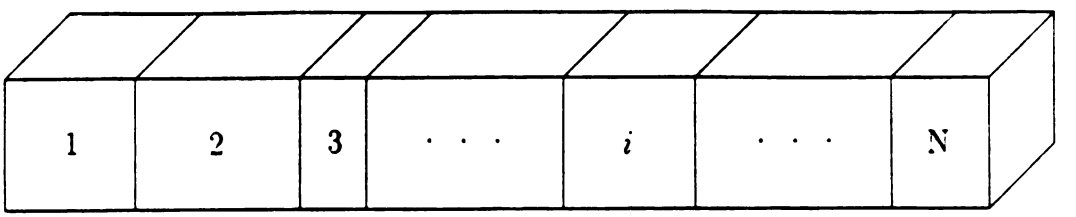

Figure C.1: Showing a N-slab in d-dimensions.

written as

$$\nu^* = \frac{\beta}{\alpha}\,, \tag{C.1}$$

where α and β are given by

$$\alpha = \sum_{i=1}^{N} \frac{f_i}{1-(d-2)\nu_i}\,,$$
$$\beta = \sum_{i=1}^{N} \frac{f_i\nu_i}{1-(d-2)\nu_i}\,. \tag{C.2}$$

Note that $\alpha - (d-2)\beta = 1$. The effective Young's modulus E^* recovers the isotropic condition

$$\frac{E^*}{2\mu} = 1 + \nu^*\,. \tag{C.3}$$

Therefore, the law of mixture is valid only in $2d$, *i.e.*, $\nu^* = \sum_{i=1}^{N} f_i\nu_i$ and $E^* = \sum_{i=1}^{N} f_iE_i$ are valid only when $d = 2$.

Set up the Cartesian coordinate x_1, x_2, ..., x_N, where x_1 is along the longitudinal direction and x_2, x_3, ..., x_N are along the transverse directions. Assume that all of the transverse directions are symmetric. Then we just need to prove that the effective elastic properties of the N-slab are the same along x_1 and x_2 directions in order to show that the N-slab is isotropic.

C.1 CASE 1: External Loading in x_1 Direction

Assume that the external loading is a longitudinal strain u_{11} along the x_1 direction. Under this loading, the strain vector of element i is $\{u^i_{11}, u^i_{22}, ..., u^i_{NN}\}$, where $i = 1, 2, ..., N$. Because of symmetry all of the transverse strains are the same, *i.e.*, $u^i_{22} = u^i_{33} = ... = u^i_{NN} = u_{22}$, where u_{22} denotes the transverse strain which is independent of the elements.

The total elastic energy per unit volume of the N-slab in d dimensions can be written as,

$$U = \mu\sum_{i=1}^{N} f_i\left\{\left[{u^i_{11}}^2 + (d-1)u^2_{22}\right] + \frac{\nu_i}{1-(d-1)\nu_i}\left[u^i_{11} + (d-1)u_{22}\right]^2\right\}\,. \tag{C.4}$$

Since the averaged strain is equal to the external strain, we have

$$\sum_{i=1}^{N} f_i u_{11}^i = u_{11} \ . \tag{C.5}$$

In order to find the minimum energy of the system, we introduce a function F,

$$F = U + \lambda \left(u_{11} - \sum_{i=1}^{N} f_i u_{11}^i \right) \ , \tag{C.6}$$

where λ is the Lagrange undetermined multiplier. Minimizing F with respect to u_{22}, we get

$$u_{22} + \sum_{i=1}^{N} \frac{f_i \nu_i}{1-(d-1)\nu_i} \left[u_{11}^i + (d-1)u_{22} \right] = 0 \ . \tag{C.7}$$

Minimizing F with respect to u_{11}^i, we get

$$u_{11}^i + \frac{\nu_i}{1-(d-1)\nu_i} \left[u_{11}^i + (d-1)u_{22} \right] = \frac{\lambda}{2\mu} \ . \tag{C.8}$$

Multiplying Eqn. (C.8) by f_i and summing over i, we get

$$u_{11} + \sum_{i=1}^{N} \frac{f_i \nu_i}{1-(d-1)\nu_i} \left[u_{11}^i + (d-1)u_{22} \right] = \frac{\lambda}{2\mu} \ . \tag{C.9}$$

Subtracting Eqn. (C.9) from Eqn. (C.7), we get

$$u_{22} - u_{11} = -\frac{\lambda}{2\mu} \ . \tag{C.10}$$

Substituting Eqn. (C.10) into Eqn. (C.8), we get

$$u_{11}^i = \left[\frac{1-(d-1)\nu_i}{1-(d-2)\nu_i} \right] u_{11} - \left[\frac{1}{1-(d-2)\nu_i} \right] u_{22} \ . \tag{C.11}$$

Multiplying Eqn. (C.11) by f_i and summing over i, we get

$$u_{22} = -\left(\frac{\beta}{\alpha} \right) u_{11} \ . \tag{C.12}$$

By definition, the Poisson's ratio $\nu_{11}^* = -u_{22}/u_{11}$. Therefore, we get

$$\nu_{11}^* = \frac{\beta}{\alpha} \ . \tag{C.13}$$

Substituting Eqs. (C.11) and (C.12) into Eqn. (C.4), and using the definition of the effective Young's modulus $U = \frac{1}{2} E_{11}^* u_{11}^2$, we get

$$\frac{E_{11}^*}{2\mu} = 1 + \nu_{11}^* \ , \tag{C.14}$$

where ν_{11}^* is given by Eqn. (C.13).

C.2 CASE 2: External Loading in x_2 Direction

Now let's consider the case in which the external loading is a strain u_{22} along the x_2 direction. Under this loading, $u^i_{33} = u^i_{44} = ... = u^i_{NN} = u^i_{tt}$ because of symmetry, where u^i_{tt} denotes the transverse strain of the element i, and it should be independent of the element index, *i.e.*, $u^i_{tt} = u_{tt}$.

The total elastic energy per unit volume of the N-slab can be written as

$$U = \mu \sum_{i=1}^{N} f_i \left\{ u^{i\,2}_{11} + u^2_{22} + (d-2)u^2_{tt} + \frac{\nu_i}{1-(d-1)\nu_i} \left[u^i_{11} + u_{22} + (d-2)u_{tt} \right]^2 \right\} . \tag{C.15}$$

Minimizing U with respect to u^i_{11}, we get

$$u^i_{11} + \frac{\nu_i}{1-(d-1)\nu_i} \left[u^i_{11} + u_{22} + (d-2)u_{tt} \right] = 0 . \tag{C.16}$$

Minimizing U with respect to u_{tt}, we get

$$\sum_{i=1}^{N} f_i \left\{ u_{tt} + \frac{\nu_i}{1-(d-1)\nu_i} \left[u^i_{11} + u_{22} + (d-2)u_{tt} \right] \right\} = 0 . \tag{C.17}$$

Multiplying Eqn. (C.16) by f_i and summing over i, we get

$$\sum_{i=1}^{N} f_i \left\{ u^i_{11} + \frac{\nu_i}{1-(d-1)\nu_i} \left[u^i_{11} + u_{22} + (d-2)u_{tt} \right] \right\} = 0 . \tag{C.18}$$

Subtracting Eqn. (C.18) from Eqn. (C.17), we get

$$u_{tt} = u_{11} . \tag{C.19}$$

From Eqn. (C.16), we get

$$u^i_{11} = -\frac{\nu_i}{1-(d-2)\nu_i} \left[u_{22} + (d-2)u_{tt} \right] = 0 . \tag{C.20}$$

Multiplying Eqn. (C.20) by f_i and summing over i, and using Eqn. (C.19), we get

$$u_{tt} = u_{11} = -\left(\frac{\beta}{\alpha} \right) u_{22} . \tag{C.21}$$

Substituting Eqs. (C.21) into Eqn. (C.20), we get

$$u_{11}^{i} = -\frac{1}{\alpha}\left[\frac{\nu_i}{1-(d-2)\nu_i}\right] u_{22} \ . \tag{C.22}$$

By definition, the Poisson's ratio $\nu_{22}^{*} = -u_{11}/u_{22}$. Therefore, we get ν_{22}^{*} from Eqn. (C.21)

$$\nu_{22}^{*} = \frac{\beta}{\alpha} \ . \tag{C.23}$$

Substituting Eqs. (C.21) and (C.22) into Eqn. (C.15), and using the definition of the effective Young's modulus $U = \frac{1}{2}E_{22}^{*}u_{22}^{2}$, we get

$$\frac{E_{22}^{*}}{2\mu} = 1 + \nu_{22}^{*} \ , \tag{C.24}$$

where ν_{22}^{*} is given by Eqn. (C.23).

C.3 CONCLUSIONS

From case 1 and case 2 we know that $\nu_{11}^{*} = \nu_{22}^{*}$ and $E_{11}^{*} = E_{22}^{*}$. Because of symmetry, it is obvious that $\nu_{22}^{*} = \nu_{tt}^{*}$ and $E_{22}^{*} = E_{tt}^{*}$, where $3 \leq t \leq N$. Thus we get

$$\begin{aligned} \nu_{11}^{*} = \nu_{22}^{*} = ... = \nu_{NN}^{*} = \nu^{*} \ , \\ E_{11}^{*} = E_{22}^{*} = ... = E_{NN}^{*} = E^{*} \ . \end{aligned} \tag{C.25}$$

Therefore, this N-slab in d-dimensional is isotropic and its effective Poisson's ratio ν^{*} and E^{*} are given by Eqs. (C.1) and (C.3).